Thermoviscoplasticity of Glassy Polymers: Experimental Characterization, Parameter Identification and Model Validation

Joel Méndez Diez

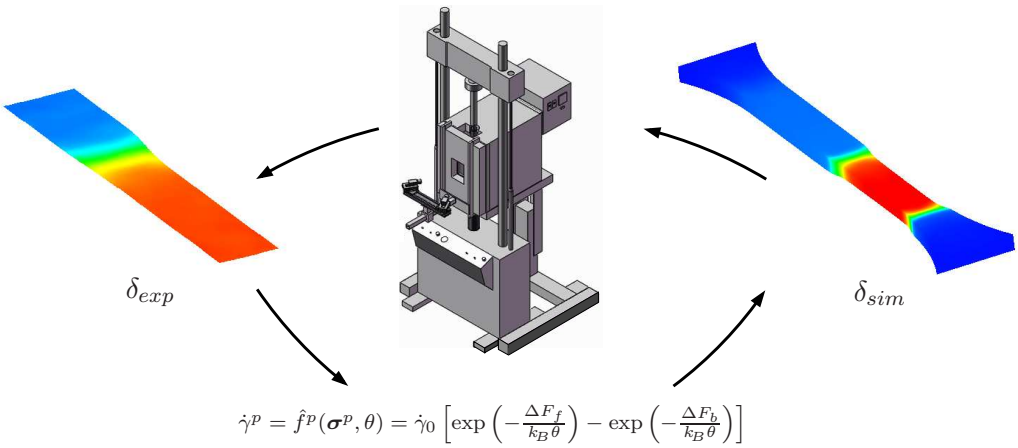

Bericht Nr.: I-22 (2010)
Institut für Mechanik (Bauwesen), Lehrstuhl I
Professor Dr.-Ing. C. Miehe
Stuttgart 2010

Thermoviscoplasticity of Glassy Polymers: Experimental Characterization, Parameter Identification and Model Validation

Von der Fakultät Bau- und Umweltingenieurwissenschaften
der Universität Stuttgart zur Erlangung der Würde
eines Doktor-Ingenieurs (Dr.-Ing.)
genehmigte Abhandlung

vorgelegt von

Joel Méndez Diez

aus Tehuacán (Mexiko)

Hauptberichter : Prof. Dr.-Ing. C. Miehe
Mitberichter : Prof. Dr.-Ing. S. Diebels

Tag der mündlichen Prüfung: 30. November 2009

Institut für Mechanik (Bauwesen) der Universität Stuttgart

2010

Herausgeber:

Prof. Dr.-Ing. habil. C. Miehe

Organisation und Verwaltung:

Institut für Mechanik (Bauwesen)
Lehrstuhl I
Universität Stuttgart
Pfaffenwaldring 7
70550 Stuttgart
Tel.: ++49(0)711/685-66378
Fax: ++49(0)711/685-66347

© Joel Méndez Diez
Institut für Mechanik (Bauwesen)
Lehrstuhl I
Universität Stuttgart
Pfaffenwaldring 7
70550 Stuttgart
Tel.: ++49(0)711/685-66325
Fax: ++49(0)711/685-66347

Alle Rechte, insbesondere das der Übersetzung in fremde Sprachen, vorbehalten. Ohne Genehmigung des Autors ist es nicht gestattet, dieses Heft ganz oder teilweise auf fotomechanischem Wege (Fotokopie, Mikrokopie) zu vervielfältigen.

ISBN 3-937859-10-1 (D 93 Stuttgart)

Zusammenfassung

Die vorliegende Arbeit befasst sich mit der experimentellen Charakterisierung des mechanischen Verhaltens glasartiger Polymere unter verschiedenen Verformungsarten, Dehnungsgeschwindigkeiten und Temperaturen, sowie mit der Anwendung einer Theorie von Thermo-elasto-visco-plastizität im logarithmischen Verzerrungsfeld, welche kürzlich in unserer Gruppe entwickelt worden ist. Eine Klassifizierung der dargestellten Experimente hinsichtlich der Verformungsart in homogen und inhomogen und hinsichtlich der Dehnungsgeschwindigkeit in isotherm und thermomechanisch wird vorgenommen. Druckbeanspruchungen auf uniaxiale Art sowie im ebenen Verzerrungszustand bei denen es zu keinem Anstieg der Temperatur kommt werden als homogene Experimente angesehen. Inhomogene Experimente werden hingegen unter Zug mittels unkonventioneller Ausrüstung durchgeführt, welche einen tiefen Einblick in dafür charakteristische Necking–Phänomen liefern. Die Vorarbeitung, Erfassung und Nachbearbeitung der experimentellen Daten werden diskutiert. In dem Berechnungsteil dieser Arbeit wird das plastisches Fließen mit zwei unterschiedliche mikromechanisch motivierten konstitutiven Theorien für glasartige Polymeren approximiert. Die Identifizierung der benötigten Materialparameter und die davon erhaltenen Simulationen bilden die Grunlage für eine kritische Bewertung der angewandten konstitutiven Gesetze. Zusätzlich werden mittels einen der vorgestellten konstitutiven Modelle Experimente simuliert und so dessen Anwendbarkeit bei hohen Verzerrungsgeschwindigkeiten untersucht.

Abstract

This work is concerned with the experimental characterization of the mechanical response of glassy polymers under various deformation modes, strain rates and temperatures together with the application of a framework of thermo-elasto-visco-plasticity in the logarithmic strain space recently developed in our group. The presented experiments are mainly classified based on the type of deformation in homogeneous and inhomogeneous and based on the applied strain rate in isothermal and thermomechanical. Homogeneous tests are understood to be uniaxial compression and plane strain compression experiments where the temperature does not rise due to deformation. Inhomogeneous experiments performed under tension are carried out together with unconventional equipment that allows a deeper insight into the necking phenomenon in glassy polymers. Discussions on the preprocessing, acquisition and post-processing of the experimental data are included. In the computational part of this work the plastic flow is approximated by means of two different micromechanically motivated constitutive theories for glassy polymers. The identification of the necessary material parameters and the simulations obtained therefrom give the foundation for a critical review of the capabilities of the employed constitutive laws. Additionally, thermomechanical experiments are simulated by one of the presented constitutive models to evaluate the capacity of the model at higher strain rates.

Acknowledgements

As a foreigner seeking to thrive outside his homeland, the positive influence of others has played an important role in writing my story in Germany. It is the intention of this lines to thank those individuals whose support and encouragement have been with me in this long journey. My deepest apologies in advance if I happened to leave anybody aside.

The work presented in this thesis was carried out between the years 2004 and 2009 while I was a co-worker at the Institute of Applied Mechanics (Civil Engineering), Chair I, at the University of Stuttgart. The generous financial support provided by the Deutsche Forschungsgemeinschaft via diverse grants is gratefully acknowledged.

Firstly I would like to express my gratitude to Professor Christian Miehe for allowing me to be part of his team. His trust in me to make use of the Institute's material testing laboratory without restrictions encouraged me to give my best in obtaining the experimental results presented in this work. His advice on continuum thermomechanics was a major contribution to the theoretical part of this thesis. As done by other colleagues in the past, I would also like to acknowledge Professor Miehe's full commitment to culture diversity within his research group, making me feel truly integrated in it. I thank Professor Stefan Diebels for accepting to be the co-referee of this thesis and for the interest that he demonstrated in it via his careful corrections.

I want to express my very heartfelt gratitude to my colleague, mentor and friend Doctor Serdar Göktepe. His deep knowledge of the mechanics of polymers were crucial to give this endeavor a successful completion. Serdar's help on many aspects of my life in Germany, not only during our time together at the Institute but also after he left, shall never be forgotten.

I am deeply indebted to Herr Ralf Plonus for all the fruitful work that we did together at the laboratory. Without his precise constructions the experiments presented in this thesis would had never reached their actual quality. Fortunately my interaction with Ralf was not only bounded to the professional field: if I ever achieved to learn the German language up to a communicative level he is certainly the one to blame.

I also want to thank Doctor Ercan Gürses for the enjoyable time that we spent together at the Institute. I will always remember his open and cooperative character to face challenges and interact with people. I would like to thank to Doctor Daniele Rosato for the years of joyful cooperation at the Institute and for being always a solid reference for me in both personal and scientific matters. To my colleagues Fabian Welschinger, Ilona Frankenreiter, Dominic Zäh and Dominik Zimmermann I would like to thank not only their continuous support on all the computer issues that I had during my long stay at the Institute but most important their friendship.

To Professor Christian Linder and Doctor Björn Kiefer I thank the very cordial collaboration in the teaching duties in which I had the pleasure to take part.

To Martina Hofacker I want to thank for her heartfelt friendship, her constant support and concern. To Felix Hildebrand I thank his enterprising spirit and his friendship.

I would also like to thank my colleague Uwe Rempler for his non-stop support in computer issues that went far beyond those found in everyday research. I will always remember him not only as the person with the deepest knowledge on computers that I know, but also as a true friend. Doctor Gerald Scheday I thank for his useful work on parameter identification, which I extensively used during my research at the Institute, and for his valuable advice in that regard. To Doctor Nikolas Apel I thank for the interesting discussions that we had every time that we had the opportunity to meet. I thank Doctor Klaus Bayreuther for the interesting discussions and his advise during our time together at the Institute. I am very fortunate to call all of them my friends.

I am deeply indebted to the students Hüsnü Dal, Aruna Prakash, Harish Iyer, Shaofei Qu and Melanie Weigert whose hard work largely contributed to the results shown in this thesis. I would also like to thank to all the COMMAS students, who I had the pleasure to meet in the diverse exercises that I taught between 2006 and 2009, for their interest in the computational mechanics of materials and their endless questions. I would like to specially thank Dinesh Kularatne for proof-reading the manuscript of this thesis and for his friendship.

I want to thank my family, Joel, María Luisa, María, Hector, Sofía and Nicolás for their constant and intense love. Their unconditional support on every enterprise that I have undertaken in my life has given me the confidence to get to where I am today. A lifetime would not be enough to express my gratitude to them.

To my uncle Luis I thank for encouraging me to continue my education beyond a Bachelor degree; without his advise it is dubious that I would had come this far. To my family in Vienna, Angelica, Carlos, Carlos Manuel, Ana Claudia and Markus, I owe the motivation to pursue graduate studies in Europe. Their personal stories of success have been always an inspiration for me. To Alfredo Salinas and Patrick Mandic I thank for their friendship since the very beginning of this journey, making it a really enjoyable one.

I want to thank my beloved wife Suad for bringing love, wisdom and tenderness into my life. Without her unconditional support in both good and bad times as well as her blind confidence in me I would had never achieved what I have done so far. My gratitude and my heart are eternally hers. Through Suad I experienced the joyful addition to a beautiful family, Roberto, Rosy and Badir, to whom I thank for their constant support and comprehension during all the years that we have been away from them.

Finally I wish to thank to whoever is responsible of placing all the above mentioned people on my way.

Stuttgart, February 2010 Joel Méndez Diez

Agradecimientos

Siendo yo un extranjero buscando triunfar fuera de su pais de origen, la influencia positiva de otras personas ha jugado un rol muy importante en mi historia en Alemania. La intención de estas líneas es agradecer a esas personas cuyo apoyo y estímulo me han acompañado en esta larga jornada. Mis más sinceras disculpas si sin darme cuenta he dejado fuera de ellas a alguien.

El trabajo presentado en esta tesis fue hecho entre los años 2004 y 2009 mientras fuí empleado en el Instituo de Mecánica Aplicada (en la facultad de Ingenieria Civil), Silla I, en la Universidad de Stuttgart. Agradezco infinitamente el generoso apoyo financiero proveido durante mis estudios por la Sociedad Alemana de Investigación a través de diversos proyectos.

Primeramente me gustaría expresar mi gratitud al Profesor Christian Miehe por permitirme ser parte de su equipo. Su confianza en mi permitiendome hacer uso de el laboratorio de prueblas de materiales del Instituto sin restricción alguna me motivó a dar lo mejor de mi al momento de obtener los resultados experimentales mostrados en este trabajo. Su asesoría en termo-mecanica del medio contínuo fue una gran contribución a la parte teórica de esta tesis. Al igual que otros colegas lo han hecho en el pasado, me gustaría reconocer el absoluto compromiso del Profesor Miehe con la diversidad cultural dentro de su grupo de investigación, haciendome sentir verdaderamente integrado en él. Agradezco al Profesor Stefan Diebels por aceptar ser co-asesor de esta tesis y por el interés mostrado a través de sus cuidadosas correcciones.

Me gustaría expresar mi gratitud de todo corazón a mi colega, mentor y amigo el Doctor Serdar Göktepe. Sus profundos conocimientos en la mecánica de polímeros fueron cruciales para dar a este trabajo un exitoso final. La ayuda de Serdar en diversos aspectos de mi vida en Alemania, no solo durante el tiempo que trabajamos juntos en el Instituto sino también después de que partió, jamás será olvidada.

Estoy profundamente en deuda con el Señor Ralf Plonus por todo el fructífero trabajo que llevamos a cabo juntos en el laboratorio. Sin sus precisas construcciones los experimentos presentados en esta tesis nunca hubieran alcanzado su calidad actual. Afortunadamente mi relación con Ralf no estuvo limitada solo al campo profesional: si alguna vez logré aprender Alemán hasta un nivel que me permitiera comunicarme libremente, es él seguramente el culpable de ello.

También quiero agradecer al Doctor Ercan Gürses por el agradable tiempo que pasamos juntos en el Instituto. Siempre recordaré su caracter abierto y cooperativo a la hora de enfrentar retos e initeractuar con las personas. Me gustará agradecer al Doctor Daniele Rosato por los años de alegre cooperación en el Instituto y por haber sido siempre para mi una sólida referencia en cuestiones tanto personales como científicas. A mis colegas Fabian Welschinger, Ilona Frankenreiter, Dominic Zäh y Dominik Zimmermann me gustaría agradecer no solo su contínuo apoyo en todos los problemas que pude tener con las computadoras durante mi larga estancia en el Instituto sino también su amistad.

Al Profesor Christian Linder y al Doctor Björn Kiefer agradezco la muy cordial colaboración en las tareas de impartición de clases en las que tuve el placer de ayudarles. A Martina Hofacker quiero agradecer su sincera amistad, su constante apoyo y preocupación. A Felix Hildebrand agradezco su espíritu emprendedor y su amistad.

También quisiera agradecer a mi colega Uwe Rempler por su ininterrumpido apoyo en asuntos computacionales que van mas allá de los encontrados en la investigación cotidiana. Siempre lo recordaré no solo como la persona con los conocimientos de computadoras mas profundos que conozco, sino también como un verdadero amigo. Al Doctor Gerald Scheday le agradezco por su útil trabajo en identificación de parámetros, el cual ampliamente utilicé durante mi investigación en el Instituto, y por su valiosa asesoría al respecto. Al Doctor Nikolas Apel le agradezco las interesantes discusiones que tuvimos siempre que teniamos la oportunidad de encontrarnos. Le agradezco al Doctor Klaus Bayreuther por las interesantes discusiones y su consejo durante el tiempo que pasamos juntos en el Instituto. Me considero muy afortunado de llamar mis amigos a todos ellos.

Estoy prefundamente en deuda con los alumnos Hüsnü Dal, Aruna Prakash, Harish Iyer, Shaofei Qu y Melanie Weigert cuyo arduo trabajo contribuyo en gran medida a los resultados mostrados en esta tesis. Tambien me gustaria agradecer a todos los alumnos del programa COMMAS, a los cuales tuve el placer de conocer en las diversas clases que enseñé entre 2006 y 2009, por su interés en la mecanica computacional de materiales y por sus interminables preguntas. Quisiera agradecer a Dinesh Kularatne por su ayuda con la corrección de esta tesis y por su amistad.

Quiero agradecer a mi familia, Joel, María Luisa, María, Hector, Sofía y Nicolás por su constante e intenso amor. Su apoyo incondicional en cada proyecto que he emprendido en mi vida me ha dado la confianza para llegar a donde me encuentro hoy. No me alcanzará la vida para expresarles mi gratitud.

A mi tio Luis le agradezco por animarme a continuar mi educación mas allá de la licenciatura; sin su consejo es dudoso que yo hubiese llegado tan lejos. A mi familia en Viena, Angelica, Carlos, Carlos Manuel, Ana Claudia y Markus, les debo la motivación para proseguir mis estudios de posgrado en Europa. Sus historias de exito personal siempre han sido una inspiración para mi. A Alfredo Salinas y Patrick Mandic les agradezco su amistad desde el principio mismo de esta travesía, haciendola verdaderamente agradable.

Quiero agradecer a mi amada esposa Suad por traer amor, sabiduría y ternura a mi vida. Sin su amor incondicional tanto en los tiempos buenos como en los malos así como sin la confianza ciega que tiene en mi, nunca habria alcanzado lo que hasta hoy he logrado. Mi gratitud y mi corazón son eternamente suyos. A través de Suad experimenté la feliz inclusión en una hermosa familia, Roberto, Rosy y Badir, a los cuales agradezco por su constante apoyo y comprensión durante los años que hemos estado lejos de ellos.

Finalmente quisiera agradecer a quien quiera que sea el responsable de poner a todas las personas arriba mencionadas en mi camino.

Stuttgart, Febrero 2010 Joel Méndez Diez

Contents

1. Introduction **1**
1.1. Motivation and State of the Art 1
1.1.1. Thermo-Mechanical Response of Glassy Polymers 4
1.1.2. Conventional Experimental Studies 7
1.1.3. General Concepts 10
1.1.4. Studied Glassy Polymer 12
1.2. Employed Experimental Equipment 12
1.2.1. Testing Machine 13
1.2.2. Optical Measurement Solution 14
1.3. Scope and Outline 16

2. Homogeneous and Inhomogeneous Compression Experiments **19**
2.1. General Testing Conditions for Compression Experiments 19
2.1.1. Isothermal Testing Conditions 19
2.1.2. Pre- and Post-Processing of the Data 19
2.1.3. Temperature Evolution in the Specimen and Metal Plates 22
2.2. Uniaxial Homogeneous Compression Tests 23
2.2.1. Experimental Setup 23
2.2.2. Results and Observations 24
2.3. Plane Strain Compression 26
2.3.1. Specimen Preparation 26
2.3.2. Standardized Experimental Procedure 26
2.3.3. Results and Observations 28
2.3.4. Repeatability 29
2.4. Thermo-Mechanical Uniaxial Compression Experiments 31
2.4.1. Results and Observations 31

3. Cold Drawing of a Dumbbell-Shaped Specimen **33**
3.1. Experimental Setup 33
3.1.1. Illumination of the Experiments 33
3.1.2. Arrangement of the Cameras 33
3.1.3. System Calibration 35
3.1.4. Employed Tensile Specimens 36
3.2. Standardized Experimental Procedure 36
3.2.1. Experimental Data Acquisition 37
3.2.2. Data Post–Processing 37
3.3. Isothermal Results and Observations 38
3.3.1. Load-Displacement Diagram 38
3.3.2. 3–D Experimental Results 39
3.3.3. Neck Velocity 44

3.3.4. Natural Draw Ratio 45
3.4. Repeatability 46

4. Thermo–Elasto–Visco Plasticity of Glassy Polymers 49
4.1. Basic Tensorial Objects of Plastic Metric Thermoplasticity 49
4.2. General Constitutive Framework of Thermoviscoplasticity 51
4.3. The Global Equations of Coupled Thermoviscoplasticity 52
4.4. Specific Constitutive Functions for Glassy Polymers 54
4.4.1. Additive Split of the Free Energy Function 54
4.4.2. Thermoelastic Contribution to Free Energy 54
4.4.3. Plastic Contribution to Free Energy 55
4.5. Micromechanically–Based Thermoviscoplastic Flow 57
4.5.1. Double-Kink Model 58
4.5.2. Micromechanical Model Based on the Distribution of Free Volume . 60
4.6. Algorithmic Implementation of Finite Thermoviscoplasticity 67
4.6.1. Thermomechanical Coupling Algorithm 68
4.6.2. Constitutive Update Algorithm at Frozen Temperature 69
4.6.3. Algorithmic Linearization for Global Newton Solver 70
4.6.4. Remarks on the Finite Element Discretization 71

5. Numerical Examples 73
5.1. Parameter Identification Methodology 73
5.2. Results Using the Double Kink Model 73
5.2.1. Isothermal Uniaxial Compression and Plane Strain Simulations . . . 73
5.2.2. Simulation of Thermo–Mechanical Compression Experiments 76
5.2.3. Simulation of Inhomogeneous Tension Tests 81
5.3. Results Using the Theory of Distributed Free Volume 86
5.3.1. Isothermal Uniaxial Compression and Plane Strain Simulations . . . 87
5.3.2. Simulation of Inhomogeneous Tension Tests 87

6. Concluding Remarks 97

A. Derivation of the Backstress Tensor 99

B. Statistics of the Freely Jointed Chain 101

1. Introduction

La razón de ser of this thesis is twofold. On one side it aims to characterize the mechanical behavior of glassy polymers via the design and execution of mechanical experiments. On the other, to use the obtained experimental data as a reference to identify the material parameters entering constitutive models of elastoviscoplasticity, permitting the evaluation of their predictive capabilities.

1.1. Motivation and State of the Art

The history of humanity has been commonly divided by anthropologists based on the most used material to produce tools during each period. From there we know the Stone Age ($2.5 \cdot 10^6 - 3300$ BC) -including the three sub-eras Palæolithic (from Greek: $\pi\alpha\lambda\alpha\iota\acute{o}\varsigma$, "old"; and $\lambda\iota\theta o\varsigma$, "stone"), the Mesolithic and the Neolithic- the Bronze Age (3300 – 1200 BC) and the Iron Age (1200 – 500 BC). After the end of the Iron Age (and most probably already before) mankind diversified the materials used in its daily life; mainly eight classes of materials were in use, namely: diverse metals, stones, ceramics, glasses, woods, skins, horns and fibers. These eight material groups remained the basis of human technology until, one and a half centuries ago, two new closely related kinds of materials named rubbers and plastics came into scene. From that moment on these new materials began not only to replace the traditional materials but to encourage the development of new products which have helped to extend the range of activities performed by mankind. It was these two materials, part of the material classification known as *polymers*, that made possible modern wonders such as the motor car, the telephone and the television set. The industrial use of rubber was well established by the start of the twentieth century, but we shall not forget that the Spanish *Conquistadores* as early as in 1530 already acquainted for the use that the Mesoamerican Indians made of it, see for example Sahagún [80] and The Research Association of British Rubber Manufacturers [85]. In what is concerned with *plastics*, there is an important clear-cut differentiation to be made regarding what the words plastics and polymers really mean. A *polymer* will contain accidental impurities originated from its production process as well as intentionally added additives that either facilitate the fabrication process or improve the properties of the final product. That resulting material is called a *plastic*.

Although different kinds of polymers possess different properties, all of them are made out of long molecules with a covalent backbone formed by carbon atoms. These long molecules are kept together by weak (also called Van der Waals) bonds and hydrogen, or secondary bonds. The low melting point of the weak bond (not far from room temperature) makes these materials to creep, which is a feature observed in any material when close to its melting point. It is this property that makes polymers differ from metals and ceramics as far as design and application concerns. After Ashby & Jones [13] polymers can be subdivided in four classes of interest: (*a*) *thermoplastics* that soften when heated (example: polyethylene), (*b*) *thermosets* that harden when a resin and a hardener are heated together (example: epoxy), (*c*) *elastomers* or *rubbers* (example: polyisoprene), and (*d*) *natural polymers* such as the last four of the list of eight materials given above (wood, skin, horns or natural fibers).

In this work special attention is given to thermoplastics, commonly known as *linear* polymers, which are the largest class of engineering polymers. Molecularly the term *linear* means that opposite to thermosets, which are heavily cross-linked, thermoplastics are not,

enabling softening via heating due to the melting of the secondary bonds that keep the molecules together, allowing the material to be formed. If the chains of a linear polymer were straighten out they would look like a piece of string. This establishes the basis of their deformation mechanism, i.e. these polymers can be drawn in such a way that the flow orients the strings, converting what initially was an *amorphous* agglomerate into a fiber in which the molecules are aligned up to a certain level, see Figure 1.1. Although generally in the literature a polymer chain is normally drawn straight for explanatory purposes, a free polymer molecule is always in a coiled state where each C–C joint along the backbone can rotate, twist, wriggle and snarl to adopt different configurations. Once melted, these chains move and accommodate randomly; when cooled down this chain cluster, depending on the architecture of the molecules, can freeze without rearranging, creating what is known as an *amorphous polymer*, or can move and partially align to form a *crystalline polymer*. For a more deep insight into the molecular rearrangements in polymers and illustrative graphical interpretations see for example Ashby & Jones [13], Brydson [25] and Carraher [27].

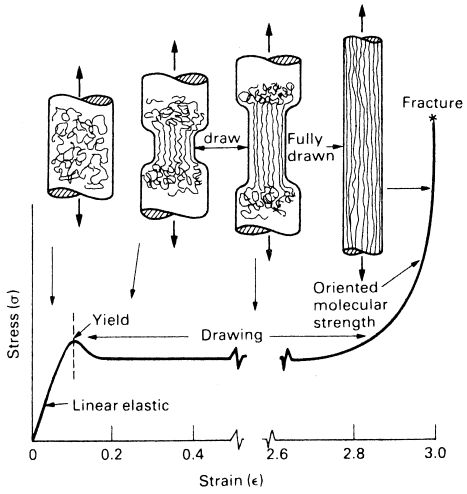

Figure 1.1: Schematic true stress-true strain diagram of an amorphous glassy polymer under tension taken from Ashby & Jones [13]. The picture clearly shows the molecular re-arrangements taking place when the material is drawn, yielding a frozen reversible plastic deformation.

The Glass Transition Temperature T_g. In general, liquids that do not fastly crystallize exhibit a so-called *glass transition*. Bueche [26] suggested a very simple but illustrative experiment to find it. If a liquid polymer is slowly cooled down from the molten state and a needle is pushed against the surface of the polymer, there will be a point during the cooling process where the force needed to push the needle into the polymer will abruptly increase. This small temperature range in which the material changes from a liquid to a glass is called *glass transition*, see Figure 1.2a. This method shows qualitatively the glass transition, but is not accurate enough to assess the temperature of the glass transition precisely.

In order to obtain a quantitatively accurate glass transition temperature, the properties associated with the volume expansion of the material must be observed, for these exhibit a unique behavior when approaching the glass transition region. For example, the volume expansion, that can be directly related to the thermal expansion coefficient α_t, is higher

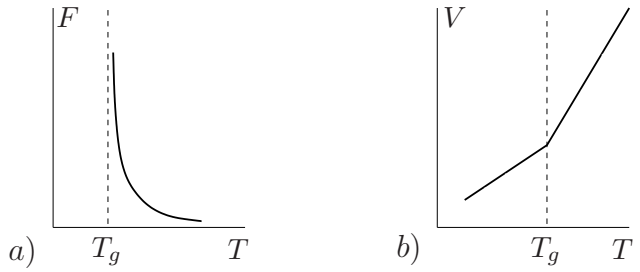

Figure 1.2: *a*) Schematic representation of the experiment proposed in Bueche [26] to locate the *glass transition*. The force F required to push a needle into a polymer piece will increase abruptly as the material approaches the glass transition. *b*) A more precise method to asses T_g is to measure the evolution of a volume-related property of the material with respect to temperature T. In the diagram the change of slope in the volume evolution at T_g can be clearly seen.

above the glass transition temperature than below it. It has been observed that even though this parameter changes from polymer to polymer, the relation of the thermal expansion coefficient below (for the glass, α_g) and above (for the liquid, α_l) the glass transition temperature keeps the relation $\alpha_g = \alpha_l/2$. This type of measurement permits to determine the so-called *glass temperature* (also called *glass transition temperature*) more precisely. Figure 1.2b shows a typical curve of the change of the volume with temperature for a glass. Bueche [26] defines the glass transition as the temperature region within which a noncrystallizing liquid, polymeric or otherwise, changes from a soft material to a hard, brittle material. At the molecular level Brydson [25] defines T_g as the temperature at which molecular rotation about single bonds becomes restricted, i.e. below this temperature the molecular movement is so slow that the liquid appears hard or glass-like. The ease of rotation of the bonds is influenced either by factors affecting an individual (single) chain or by the influence of the surrounding polymer chains. For details on the numerous factors affecting T_g the reader is referred to Bueche [26], Rehage & Borchard [79], Ashby & Jones [13] and Brydson [25].

Applications of *glassy polymers*. The use of *glassy polymers* began in the 1950's with the development of polystyrene (PS). Due to their various applications and adaptability their use increased and diversified tremendously ever since. PS became a replacement for cellulosic esters which were, up to that time, the basic thermoplastics employed to produce plastics from organic bases like wood or cotton. One typical example of cellulosic esters is cellulose nitrate or *celluloid*, at one-time used to produce photographic film, bicycle parts and toys. Today, celluloid is used in knife handles, table-tennis balls and glass frames, see Brydson [25]. Although it was considerably more brittle than the cellulosic materials, PS was widely used due to its relative low production costs and good processability. During the last 45 years new glassy polymers such as poly(methyl methacrylate) (PMMA), better known as plexiglass, having excellent optical properties, or polycarbonate, being an attractive combination of clarity and toughness, have been developed and marketed.

Despite the considerable high production costs of *Bis-phenol A polycarbonate* due to special care needed in processing, limitations in chemical and ultraviolet light resistance, moderate electrical tracking resistance and notch sensitivity, these materials are well placed in the so-called specialty plastics. Such a relevance arises from the well documented toughness, rigidity, transparency, self-extinguishing characteristics, good electrical

insulation characteristics and heat resistance among others. Some polymers are rigid but have not good optical properties, others are transparent but soft; bis-phenol A polycarbonate is one of the few materials in which a good compromise between these desirable properties and a relative low cost is to be found. Moulded polycarbonates are used in many different fields. For electronics and electrical engineering applications it takes the form of covers for time switches, batteries and relays. There, four of its properties are simultaneously exploited, namely its good electrical insulation, transparency, flame resistance, and durability. A polycarbonate of a very high purity is used to produce optical media in general, particularly compact discs (CD), where its outstanding optical properties become invaluable. Since the invention of the CD in 1982, 42 billion discs have been produced from Bayer's Makrolon alone. Many home appliances are made out of polycarbonate: baby bottles, cups, saucers, food processor bowls, coffee makers, cold water reservoirs, and vacuum cleaner housings just to mention a few. These applications speak for the easiness of the injection moulded pieces made out of this material to be removed from the mould, its resistance to be stained by beverages as well as their ability to be sterilized. For more extensive and detailed applications of polycarbonate see Brydson [25] pp 575-578, for details about Bayer's Makrolon visit Bayer [1]

1.1.1. Thermo-Mechanical Response of Glassy Polymers. Crist [30] concluded that almost all solid polymers – amorphous polymers below the glass transition temperature T_g or crystalline polymers below the melting temperature T_m – undergo a permanent shape change when subjected to a stress of sufficient magnitude. In this work, similar to what Lu & Ravi-Chandar [58] distinguished in tension experiments of polycarbonate before its final fracture, five stages in the description of the deformation of glassy polymers well below T_g are differentiated. A typical stress-strain curve of an amorphous polymer under compression, displaying these featured stages of the mechanical response upon loading, is depicted in Figure 1.3.

① Reversible elastic and linear viscoelastic region at low stress.

② Nonlinear elastic to viscoelastic transition at moderate stress.

③ Yield region at high stress.

④ Strain softening at moderate strains.

⑤ Strain hardening at large strains.

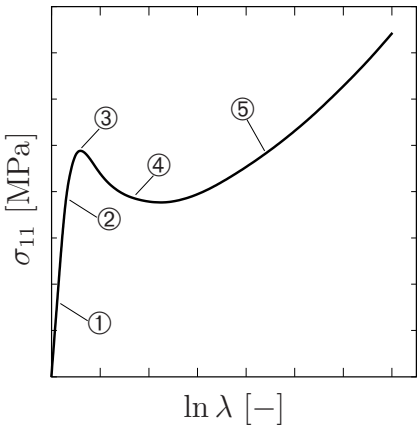

Figure 1.3: Schematic true stress-true strain diagram of an amorphous glassy polymer.

It should be noted that most of the responses during large deformations are highly nonlinear, since the true linear range for polymers is very small. Brown & Ward [24] claimed that the strain softening appears to be a general feature of the behavior of amorphous glassy polymers. Other processes such as crazing, voiding, and fracture may also take place when a polymer is deformed to some extent, however, these phenomena are out of the scope of this work and thus are not taken into account. The process of

yielding in glassy polymers is of tremendous technological importance since it defines the upper limits of the service stress in load-bearing applications or the conditions required for shaping parts during manufacturing.

Temperature- and Rate-Dependent Yield and Post-Yield Behavior. For crystalline materials like metals and ceramics, the scientific basis of yielding is well understood, ascribed as planes of atoms sliding over each other to new equilibrium positions. However, glassy polymers (especially amorphous polymers), by definition, are disordered solids lacking of a well specified equilibrium state in the micro level, hence their fundamental nature of yielding and subsequent plastic deformation still to be examined, see for example Boyce, Weber & Parks [22] and Miehe, Göktepe & Méndez [73]. In the conventional engineering concept, the *yield point* is the point beyond which the deformation ceases to be entirely elastic and starts to deform plastically. In the stress-strain curve, the yield point usually lies before the maximum stress in the moderate strain region. The above description for yield point is based on the experience with metals due to the distinct mechanisms causing the two types of deformation: lattice distortion and dislocation motion. Nevertheless, this idea cannot be applied directly to glassy polymers since the distinction between elastic and plastic deformation is not clear-cut in experimental investigations. Thereby here, the stress maximum $\mathrm{d}\sigma/\mathrm{d}\epsilon = 0$ is taken as the *yield stress*, and the corresponding point in the stress-strain curve is denoted as the *yield point*. The yield stress is highly sensitive to diverse environmental conditions, which will be analyzed in the subsequent chapters specially regarding the effects of temperature, strain rate and deformation state, assuming a constant hydrostatic pressure and an initially equal status of structures in test samples (e.g. chemical microstructures, physical aging and mechanical history). For the detailed observations on those unmentioned factors having impact on the yield stress of amorphous polymers the reader is referred to Spitzig & Richmond [84] for hydrostatic pressure influences, and to Brady & Yeh [23] and Golden, Hammant & Hazell [39] for thermal ones.

Christiansen, Baer & Radcliffe [28] performed a series of tension experiments on polycarbonate under different pressures ranging from 1 atm ($\sim$ 1b) up to 8kb, being the first of most interest for the problem at hand. The cross-head velocity used in their isobaric experiments was 0.005 in/min (approximately 0.127 mm/min) with temperatures ranging from 116K (-157°C) to 300K (27°C). Their results manifested that the yield stress as well as yield strain increases with decreasing temperature. G'sell et al. [43] conducted similar tensile experiments on the same materials at a true strain rate of 1×10^{-4} s^{-1} but under higher temperatures ranging from 25°C to 150°C. The tendency of the experimental data are analogous except for the yield stress which is prone to zero in the vicinity of T_g, indicating that at the glass transition temperature ($T_g = 145$°C for polycarbonate), or above it, glassy polymers behave like viscoelastic fluids deforming at a small, nearly constant stress.

Bauwens-Crowet, Bauwens & Homes [15] measured the yield stress over a wide range of true strain rates and temperatures on polycarbonate and PVC in tension tests. Their study revealed that the yield stress in amorphous glassy polymers appears to be true strain-rate dependent, i.e. a larger imposed true strain rate $\dot{\epsilon} = \overline{\ln \lambda}$ invariably results in a greater yield stress σ_y. Haward [50] further found that the viscoelastic heating may cause a temperature rise and thus reduces the yield stress at very large rates. It is noteworthy to mention that special attention is to be given to the applied true strain rates specially

when performing numerical simulations of the observed mechanical behavior of glassy polymers since thermomechanical effects easily arise, which must be taken into account in the applied constitutive models. A much larger rate dependency of the yield stress of polycarbonate is seen when the temperature approaches T_g, as shown in G'Sell et al. [43]. A characteristic feature of large deformations in solid linear polymers including glassy polymers is that, when the stress is removed at the end of the experiment, the major part of the plastic deformation remains. However, if the temperature is raised above the glass transition temperature T_g, the stored deformation upon unloading is reversed and the material returns to its original shape. Boyce & Haward [19] deduced that the polymers which have been permanently deformed are capable of *remembering* their previous shape and behave as though they comprise a frozen elastic extension rather than true flow. The post yield behavior of glassy polymers is governed by two phenomena, namely the strain softening and strain hardening.

Yield, often associated with a subsequent stress drop (*strain softening*) on the stress-strain curve, was in the past totally attributed to the adiabatic heating appearing during deformation. This erroneous appreciation coined the term localized *melting* which Vincent [89] refuted via isothermal tension experiments through which it was found that despite the fact that thermal effects do occur, these cannot explain the phenomena of cold-drawing due to basically three reasons: *i*) a neck can nucleate and propagate even at very low deformation rates, where isothermal deformation conditions are assured, i.e. the adiabatic effect can not explain the necking, *ii*) the drop of the tangent modulus ($\mathrm{d}\sigma/\mathrm{d}\epsilon$) in the region of uniform extension falls by a much larger factor than that obtained by the very small temperature raise caused by low deformation rates, *iii*) if stretching is stopped after the specimen necked and is later resumed, complex relaxation and re-yielding effects are encountered, being not able to be explained by adiabatic heating. Necking became then ascribed to effects that are geometrical in nature since the fall in cross-sectional area during stretching is not compensated by an adequate degree of strain hardening. Ward [91] concluded that adiabatic heating effects become important as the strain rate is raised above 0.1 min^{-1}, which is an important reference when performing compression experiments. Here, we define the strain softening as a fall in the true stress under isothermal conditions after the onset of yielding below the glass transition temperature T_g. The term *yield drop* was first adopted by Brown & Ward [24] to describe this phenomenon. G'Sell & Jonas [44] and [45] found that the true yield drop is observed for all glassy polymers (thermoplastics and thermosets) below their glass transition temperature, but that the magnitude differs substantially from one material to another. See for example a comparison between PC and PMMA in Figure 1.4, where the amount of softening after yielding drastically changes from one material to another.

The unique tension experiments performed on polycarbonate at room temperature in G'sell et al. [43] allowed to exclude the effect of cross-section reduction thanks to their superb experimental setup and showed that the yield drop corresponds to a true-strain softening of the material. At higher temperatures the strain softening is strongly affected by the strain rate: a higher strain rate results in a more pronounced strain softening while at an extremely low strain rate (2×10^{-5} s^{-1}) under 125°C, the strain softening is even surpassed. The temperature, in turn, is also found to have influences; the stress decreases more abruptly when the temperature is approaching T_g. Analogously, no strain softening is observed above the glass transition temperature, at which the material becomes rubber-like. Crist [30] identified quench cooling, mechanical cycling and hydrostatic pressure

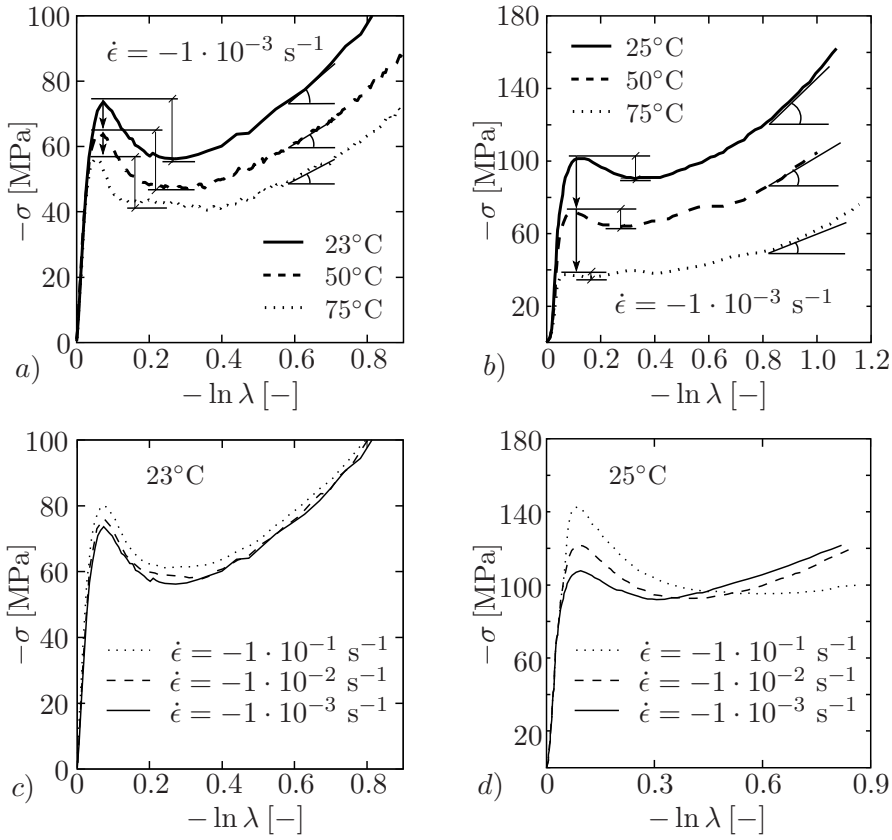

Figure 1.4: Uniaxial compression experiments showing temperature and strain rate dependency of two different glassy polymers. *a*) Isothermal compression experiments for PC done in our group. *b*) Isothermal compression experiments for PMMA. *c*) Experiments to show the effect of the applied true strain rate on PC done in our group. *d*) Effect of the applied true strain rate on PMMA. *b*) and *d*) are from Arruda, Boyce & Jayachandran [11].

as those variables reducing the amount of strain softening in a glassy polymer sufficiently below T_g.

The most famed phenomenon associated with the plastic instability in glassy polymers is the onset of the constriction known as *neck* or *necking* appearing during tensile deformation of most of amorphous polymers such as PVC, PC and PMMA (Haward [49]). When a dumbbell-shaped specimen is extended at a constant speed, it does not deform to the same extent through the whole gauged section. Instead, the material starts to extend at one point to form a neck which then grows until it covers the whole length of the test piece. During the drawing process, the force applied to the specimen to propagate the neck remains approximately constant, being often termed as *creep-like* deformation. The amount of strain (draw ratio) along this stable neck is called *natural draw ratio* since it is determined by the material hardening characteristics and not by the amount of drawing imposed on it. See Allison & Ward [6] and Séguéla [82] for more details. Finally when the neck reaches the shoulder of the dumbbell-shaped specimen, the stress will start to rise, and the strain hardening is recorded until the final fracture occurs, see for instance Boyce & Haward [19].

1.1.2. Conventional Experimental Studies. Glassy polymers are considered in this work to have an initially isotropic and axisymmetric structure, indicating that their properties are independent of directions. Before exploring their mechanical behavior in detail, it is necessary to review the types of experiments that have been used in the

literature to study the intrinsic stress-strain response of the material since the observed behavior depends to a large extent on the deformation state. In the following subchapters, the principal features of some common mechanical experiments on glassy polymers are summarized.

Homogeneous Compression Experiments. The uniaxial compression experiment is a widely used conventional test method for the investigation of the mechanical response of glassy polymers since, as already stated before, these do not neck under compression. Despite that this kind of testing represents a convenient method to observe the intrinsic characteristics of glassy polymers, these experiments must be prepared and carried out carefully since the test pieces are prone to buckle if the diameter-to-height ratio tends to be too small. Moreover, friction between the sample and the loading platen is not completely eliminated even if lubrication is applied with the best of effort, developing an additional constraint. Albeit a compromise value for the diameter-to-height ratio is suggested by Bowden [16] as 0.5, many researchers have taken a ratio equal or larger than 1 in their uniaxial compression experiments using both cylindrical and cubic specimens, e.g. Boyce & Arruda [17] tested on cylindrical specimens of polycarbonate with 6.35 mm in diameter and 6.35 mm in height. Boyce, Arruda & Jayachandran [18] used cubic specimens with equal edge dimension 11.1 mm of the same material. Melick, Govaert & Meijer [62] and [63] also performed a series of compression tests on cylindrical specimens of polycarbonate and polystyrene using dimensions of ϕ 6 mm $\times$ 6 mm and ϕ 8 mm $\times$ 8 mm separately. Arruda, Boyce & Jayachandran [11] worked on PMMA with cubic specimens having a dimension of 12.7 mm on edges. Dupaix & Boyce [32] employed the ratio of 0.258 taking the dimension of the cylindrical specimens of PET to be ϕ12.39 mm $\times$ 3.2 mm.

During the uniaxial compression experiments, the local transverse area A effectively increases with time, lowering the true stress $\sigma_t = F/A$ after yield. With careful attention to frictional end effects, alignment and sample geometry, Boyce, Arruda & Jayachandran [18] reported to have achieved a macroscopically uniform deformation far beyond the yield on cylindrical specimens of polycarbonate at room temperature. Although similar treatment was explicitly described recently by others, e.g. Melick, Govaert & Meijer [62], [63] and Dupaix & Boyce [32], here we stick to a better arrangement proposed by Boyce & Arruda [17] and Arruda, Boyce & Jayachandran [11]. A schematic drawing of the special treatment used in this work will be further detailed in Chapter 2.2.1, Figure 2.4.

In the case of plane strain compression experiments, a compressive force is applied onto a cubic specimen laying in a channel die (see Boyce, Arruda & Jayachandran [18] and Dupaix & Boyce [32]). The sample is compressed via a punch and expanded in the other lateral direction. The problem of frictional constraint at large strains is not negligible because the area of the specimen surfaces having contact with the channel die and the punch in the loading direction increases as deformation proceeds. This friction often brings in a second stress drop in the true stress-strain curve which will be discussed and solved in Chapter 2.3.1. Moreover, the increase of surface area also sets a roadblock when we calculate the true stress. The assumption of incompressibility during deformation will serve to solve the above mentioned calculation barrier as it will be shown in the subsequent chapters. Boyce, Arruda & Jayachandran showed that the plane strain yielding occurs at a greater stress than for uniaxial compression due to pressure effects

resulting from the mentioned dimensional constraint.

Inhomogeneous Tensile Experiments. As mentioned before, the deformation of glassy polymers under tension is termed inhomogeneous due to the onset of a macroscopic neck in the gauged section of the tension specimen. This entails a non-homogeneous strain distribution along the test piece, disabling the later identification of material parameters by conventional methods. Specimens with a circular cross section are more frequently employed in tensile experiments than flat ones with a rectangular transverse area. In both cases, stress is easier to obtain as nominal stress, albeit the overall true stress is difficult to determine due to the variation of the cross-sectional area after the onset of necking. In Figure 1.5 real images of the stages of deformation of an inhomogeneous tension test, similar to those shown in Figure 1.1, are included.

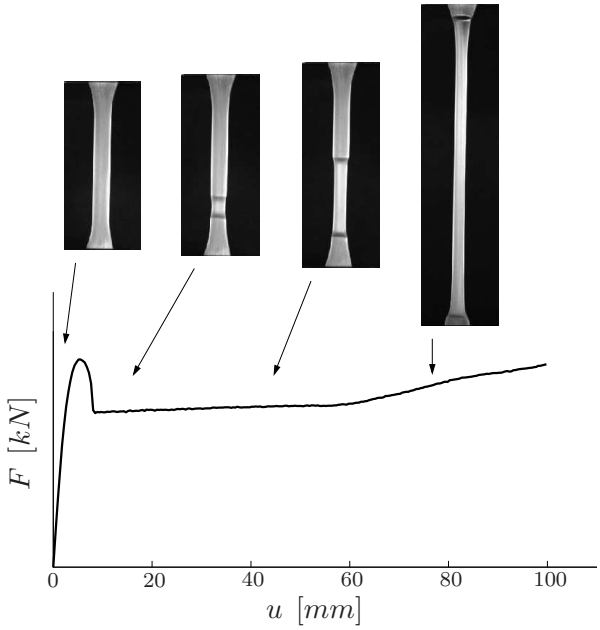

Figure 1.5: Real experiment carried out under tension using a flat specimen. Due to the technical difficulties of carrying out a true strain-controlled tension test, the load-displacement diagram obtained at a deformation rate $\dot{u} = 50$mm/min is presented.

Ward [91] summarized two ways in which a neck may be initialized. First, if for a given applied load, one element is subjected to a higher true stress, because its effective cross-sectional area is smaller, that element will reach the yield point at a lower tension than any other point in the sample. Secondly, a fluctuation in material properties may cause a localized reduction of the yield stress in a given element so that this element reaches the yield point at a lower applied tension. According to what is explained there, necking may actually take place everywhere on a relative long profile of the specimen. Different methods were raised in the preparation of the specimen from cylindrical bars to provoke the nucleation of the neck at a particular site. Boyce & Arruda [17] and Boyce, Arruda & Jayachandran [18] tapered a cylindrical bar of polycarbonate at the middle plane by gradually reducing the diameter using a 1 in (about 25.4 mm) radius tool from ϕ12.7 mm to minimum ϕ6.35 mm forming an hour glass shape contour in that region. G'Sell et al. [43] machined rod specimens in the mid-plane on a lathe to a similar contour as in Boyce & Arruda [17]. G'Sell, Aly-Helal & Jonas [41]

and G'Sell, Hiver & Dahoun [42] introduced a geometric defect section extended to a certain length at the center of the specimen to pre-define the location of the neck initiation in other tensile experiments. Bowden [16] pointed out two drawbacks of the tensile tests for studying the yield behavior of glassy polymers: firstly, in many plastics, the tensile stress can lead to fracture before yield occurs, and secondly, it is only the extrinsic yield point (maximum nominal stress) that can be readily investigated. Once the specimen has formed a neck, as it will generally do at the extrinsic yield point, it is very difficult to work back to obtain the intrinsic true stress-strain function for the material, since the stress and strain in the neck are difficult to measure with any precision and the strain rate has increased locally. However, new measuring techniques have been developed over the years and are able to characterize the locally inhomogeneous deformation beyond yielding with adequate precision.

There are basically two kinds of loading control in performing the tensile experiments. Due to its simplicity to implement, the traditional way by using a fixed displacement rate (also referred to as *cross-head speed* and equivalent to *nominal strain rate*) is more preferable than loading at a true strain rate. Three typical techniques of recording the local deformation under the displacement rate control are to be found in Boyce & Arruda [17], G'Sell, Aly-Helal & Jonas [41] and Parsons et al. [76], which can be further divided into two categories: contact and non-contact techniques. Boyce & Arruda [17] mounted a lateral extensometer to a tensile specimen of polycarbonate to measure the local diameter change at the region of the smallest cross-section. The weak points of this method are conspicuous, it can only provide the data of transversal strain in the mid-plane, furthermore the installation/un-installation of the extensometer is lengthy and has to be repeated for each individual test. G'Sell, Aly-Helal & Jonas [41] put forward a photographic measurement with the aid of a camera mounted facing the sample of HDPE and connected to a chart recorder. The test sample was specially treated by marking a set of 39 points spaced 1 mm apart along the 40 mm gauge length. This non-contact technique provides a more convenient way to measure the local strains in a relatively long profile, but the preparation of the specimen as well as the post-processing of the images can be tedious and only the uniaxial strain can be directly obtained based on the displacements of the marked dots with a questionable accuracy. Parsons et al. [76] also conducted tensile experiments on HDPE using a CCD camera equipped with a 200 mm lens providing high resolution (1280×1024 pixels) 12bit images. A random speckle pattern was applied to each specimen with an airbrush filled with India ink. It is a new non-contact measuring technique (also referred to as *video extensometer*) and able to give an accuracy greater than 30 pixels/mm with the minimum speckle size of about 0.1mm. This up-to-date method is easy to implement and able to provide sufficiently high accuracy. In this work as well as in Miehe, Göktepe & Méndez [73], we used a similar optical measurement solution provided by GOM mbH to characterize the distribution of the displacements and local strains.

1.1.3. General Concepts. At this stage it is important to establish the difference between standard engineering measurements, generally carried out by the producer of a specific material to fill out the corresponding *material data sheet*, and the experimental work intended to serve as validation for material constitutive theories. For the first case, physical quantities are normally obtained by the application of ISO, IEC or DIN experimental standards. Online data-bases such as Campus [2] and Bayer [1] are excellent sources of general material properties. An illustrative example of this case is the acqui-

sition of the engineering yield stress characteristic of a glassy polymer in particular. A single value is obtained at specific temperature, relative humidity, pressure and strain rate. This unique value for a specific material serves as a reference for engineers who want to produce pieces of that material for diverse uses. If the producer wishes to know if the employed material complies with international standards he or she can reproduce the test conditions and confirm the quality of the delivered raw material. On the other side, when material parameters are to be identified from homogeneous experiments or Finite Element (FE) validations are needed, different variables must be employed and a *common* quantity must be found that is both, measurable in the laboratory and reproducible via simulations. It can be that the deformation rate specified in an ISO standard generates adiabatic heating in the specimen, yielding the unavoidable softening of the material; for the first case described above this effect is un-relevant since the phenomenon is considered as a whole and the designer requires that the stresses in the structure made out of that material do not surpass that yield stress. If the experimental results are intended to be used to identify the material parameters contained in a specific material model, then the decoupling of thermal and mechanical effects is required. For this case different kinds of experiments must be carried out to be able to isolate these various effects. Also for the second case, different structures made out of the studied material have to be loaded and deformed to obtain not only load-displacement data but also measurements of the inhomogeneous strain distribution along its surface. For example, in MÉNDEZ [64] the predictive capabilities of a large strain constitutive theory of rubber viscoelasticity to solve inhomogeneous Boundary Value Problems (BVP) were examined. 3-D optical measurements were performed on inhomogeneous specimens subjected to shear. It was noticed that from the 3-D results the shear angle distribution could be obtained from the surface of the specimen via post-processing. This significative variable was then obtained from simulations, making them comparable with experiments.

Next, a review of the most significant quantities employed throughout this work is given, based on which experiments and constitutive modeling will be performed. The **nominal strain** ε is the uniaxial variation of length Δl normalized by the original (undeformed) length l_0

$$\varepsilon = \frac{l - l_0}{l_0} = \frac{\Delta l}{l_0} \tag{1.1}$$

where l is the deformed length. The **true strain** ϵ is defined as the integral of the above defined quantity, also known as *logarithmic strain* or *natural strain*

$$\epsilon = \int_{l_0}^{l} \frac{\mathrm{d}l}{l} = \ln \frac{l}{l_0} \ . \tag{1.2}$$

The two quantities do not diverge considerably at small strains, however they become unequal close to a value of 0.1. Frequently in tensile experiments the term *stretch* or *stretch ratio* is used to denote the ratio between the deformed length l and the undeformed length l_0

$$\lambda = \frac{l}{l_0} \ . \tag{1.3}$$

The stretch λ will be a key quantity on which the subsequent experimental work under compression will be based. In a special case when the tensile experiment is conducted using a specimen with a constant cross-sectional area along the gauged section, λ can be then used to calculate the *natural draw ratio* based on the incompressibility condition.

Further details can be found in Chapter 3.3.4. The insertion of (1.3) into (1.2) yields the *true strain* ϵ in the form

$$\epsilon = \ln \lambda \ . \tag{1.4}$$

The **nominal stress** or *Engineering* stress σ_n is the applied load F divided by the initial (undeformed) cross-sectional area A_0 perpendicular to the loading direction

$$\sigma_n = \frac{F}{A_0} \ . \tag{1.5}$$

The **true stress** σ is the load F divided by the instantaneous cross-sectional area A of the specimen, namely

$$\sigma_t = \frac{F}{A} = \frac{F}{A_0} \cdot \frac{l}{l_0} = \frac{F}{A_0} \cdot \lambda = \frac{F}{A_0} \cdot \exp(\epsilon) \ . \tag{1.6}$$

It is preferable to use *true stress* when investigating the intrinsic properties of a material. On the other hand, when considering the properties of the material as a whole, the *nominal stress* is believed to be more effective and convenient since when the *nominal stress* is at its maximum, the material is supposed to carry the maximum load.

Other quantities. The so-called *Young's modulus* E may be evaluated by either the nominal or true stress as both of them coincide at low strains

$$E = \lim_{\varepsilon \to 0} \frac{\mathrm{d}\sigma}{\mathrm{d}\varepsilon} \ . \tag{1.7}$$

The *Poisson's ratio* ν, a measurement of the transverse strain ε_x, which is perpendicular to the loading direction y, provides a second elastic constant

$$\nu = \frac{-\varepsilon_x}{\varepsilon_y} \ . \tag{1.8}$$

The *bulk modulus* K and the *shear modulus* G can be determined from E and ν as

$$K = \frac{E}{3(1-2\nu)} \quad \text{and} \quad G = \frac{E}{2(1+\nu)} \ . \tag{1.9}$$

Gilmour, Trainor & Haward [36] reported typical values for glassy polymers near room temperature: $E \sim 3$ GPa and $\nu \sim 0.035$, hence $K \sim 3$ GPa and $G \sim 1.1$ GPa.

1.1.4. Studied Glassy Polymer. The glassy polymer used in all the experiments presented in this work is a commercial grade of bisphenol A polycarbonate (PC) called Makrolon 2607 produced by *Bayer Material Science*. The most relevant mechanical properties reported by the producer [1] are listed in Table 1.1. All the test specimens employed here were manufactured by injection moulding at the *Deutsches Kunststoff Institut* (DKI) in Darmstadt (see [3]).

1.2. Employed Experimental Equipment

All uniaxial compression, plane strain compression and tensile experiments presented in this work were performed using an MTS 810 Material Test System coupled to an MTS 651 Environmental Chamber to maintain constant environment temperature during the experiments. In order to counterbalance temperature fluctuations, a cooling apparatus filled with liquid nitrogen was connected to the environmental chamber via an insulated plastic pipe. Several new fixtures and fittings were produced to comply with our experimental setup (Figure 1.6). Detailed specifications of the computers and peripherals can be found in the following subchapters.

Table 1.1: Typical Values of the Polycarbonate Makrolon 2607

Material Properties (23°C, 50% r.h.)	Value	Test Condition
Tensile Modulus (MPa)	2400	1 mm/min
Yield Stress (MPa)	67	50 mm/min
Yield Strain (%)	6.1	50 mm/min
Stress at Break (MPa)	65	50 mm/min
Strain at Break (%)	115	50 mm/min
Density (kg/m^3)	1200	-
Glass Transition Temperature (°C)	145	10°C/min

1.2.1. Testing Machine. The MTS 810 Material Test System is a servo-hydraulic testing machine used to conduct tension and compression experiments on materials and components. It can be split into the following major parts (see Fig. 1.6 for reference): An *actuating cylinder*, having the function of deforming the material to be tested, can provide a maximum stroke of 100 mm under tension or compression. Two *vertical columns*, made of solid steel coated with chrome plating, support and guide the crosshead. The *crosshead* (or *traverse*) is the horizontal beam located in the upper part of the two parallel columns. The crosshead is moved using two *hydraulic lifts* placed parallel to the vertical columns. Once at the desired position and prior to the initiation of an experiment, the traverse must be locked using a hydraulic mechanism. The loading frame, formed by the actuating cylinder, the vertical columns, the traverse, and the steel skeleton keeping these components together, has a maximum load capacity of 250 kN. The *alignment fixture*, which is a high precision-machined component used to line up the upper and lower axis rods with each other, i.e. to align the fixtures holding the specimens, is crucial to avoid undesired shearing in the experiments. This mechanism serves as a coupling to attach the force transducer to the traverse. Also known as *load cell*, the *force transducer* has a maximum loading limit of 100 kN and can measure an applied force with an accuracy of 2.5 N. The removable *hydraulic grips* (not shown in Fig. 1.6) can be used to carry out tension experiments by holding the flat specimens at both ends or as an aid to attach to the machine different types of dies to perform compression experiments. The above mentioned hydraulic grips can be used at a maximum temperature of 40°C, which means that in order to perform tension and compression experiments at higher temperatures the grips must be removed and new mechanical fixtures have to be used. For this purpose two precision machined *axis rods* were employed. The upper and lower axis rods are screwed to the load cell and the actuating cylinder, respectively. These rods transmit the load applied by the machine allowing the traverse and the actuating cylinder to be separated by a distance that is large enough to permit the execution of temperature-controlled experiments inside an environmental chamber (see Figures. 1.6 and 1.8). Depending if an experiment will be carried out under tension or compression, further fixtures will be attached to the axis rods. The MTS testing machine works with the software TestStar IIs which coordinates via feedback control the entire testing system in real time, enabling to run uniaxial tension and compression experimental routines. The computer on which

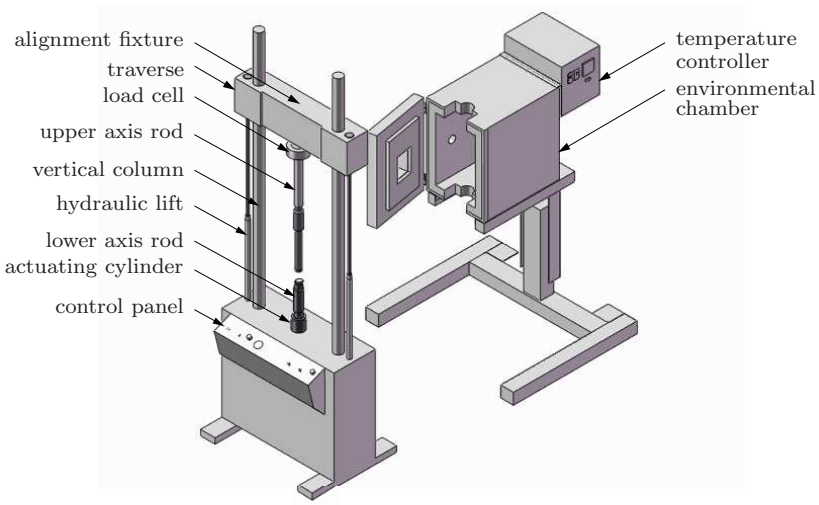

Figure 1.6: Main components of the MTS 810 Material Test System and MTS 651 Environmental Chamber. The sketch shows the setup for uniaxial compression experiments.

this software is installed gives the desired experimental program into a controller box, which in turn sequentially executes the instructions contained in it by converting them into specific commands to the MTS testing machine. Throughout the execution of the program, the software collects the load and displacement data at a user-defined interval of time.

Environmental Chamber and Cooling Apparatus. The MTS 651 Environmental Chamber, as depicted in Figure 1.7, is capable of testing versatile materials and components within various ranges of high and low temperatures. Two electrical heating elements are used for high temperature testing up to +315°C. An electric motor-driven fan provides diffused convection heat for uniform temperatures. The specimen is shielded from direct radiant heat by the fan baffle and the fan blades. Besides, the integrated Eurotherm 2404 controller together with a thermometer placed near the specimen in the chamber governs the temperature regulation by close-loop control. The environmental chamber is able to maintain a constant temperature within a bias of ±2°C and recover from 2 min door-open to the set point temperature in no more than 6 min. The chamber is of all-welded construction with fiberglass insulation between the outer liner and the stainless steel inner liner. The window is multiplane, tempered glass and sealed. This keeps the moisture out and prevents fogging and frosting, which also gives us the possibility to record the images of the deforming specimen from outside of the chamber during the course of an experiment.

The coolant medium fed into the environmental chamber is liquid nitrogen (LN), of which incoming amount is automatically regulated by the temperature controller through an electromagnetic inlet valve integrated on the back of the chamber. The use of liquid nitrogen facilitates the temperature regulation and is able to decrease the temperature to −129°C. If necessary, pressurized air can be additionally connected to the inlet valve of the LN container, forcing the coolant into the chamber at a faster speed.

1.2.2. Optical Measurement Solution. The optical measurement solution ARAMIS produced by GOM mbH is based on the grating method and photogrammetry. It is well suited for measuring three-dimensional deformations and strain distributions of objects

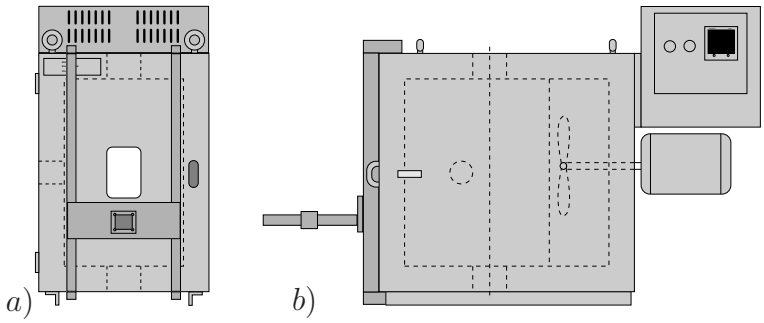

Figure 1.7: *a*) the front view of the environmental chamber with the door closed. *b*) lateral view showing the temperature controller and the support for the CCD cameras mounted on the door.

subjected to static or dynamic load. The hardware for image acquisition is comprised of two identical modules, each containing a lens, a CCD camera and an image processing card. The lens is mounted onto an analog camera module, and further connected to an individual serial port of the corresponding image processing card in the computer which handles the image acquisition and data post-processing via the ARAMIS software (version 4.7.4-2) under Linux. The analog CCD camera can provide 8-bit images up to a resolution of $768(horizontal) \times 572(vertical)$ pixel in TIFF format and record at a maximum frame rate of 12 fps. The integrated setup of the tensile experiments with the optical measurement system is depicted in Figure 1.8. In the following the mechanism of the ARAMIS software for 3D strain computation will be described.

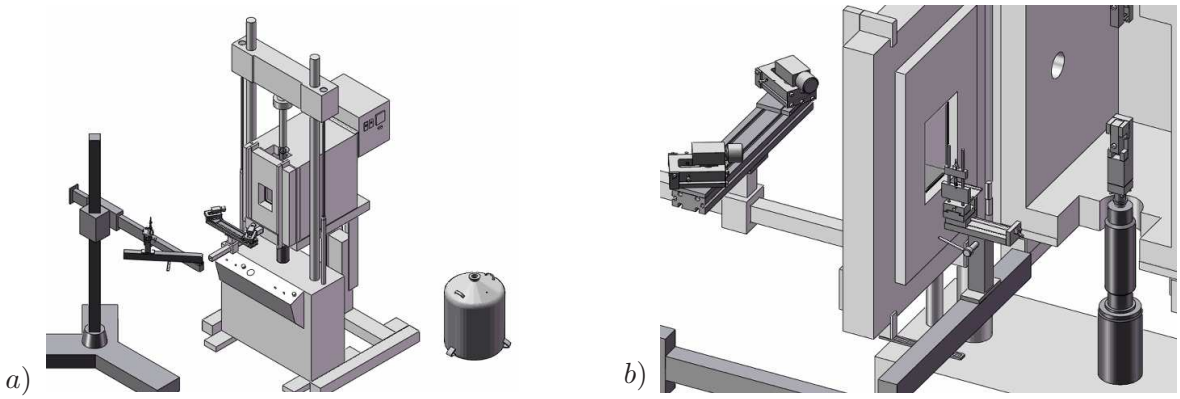

Figure 1.8: MTS servo-hydraulic testing machine *a*) with the door of the environmental chamber closed and ready to perform a 3–D experiment by capturing the deformation sequence via the two cameras mounted on the door. *b*) The door of the environmental chamber is kept open and the tripod is employed to facilitate the calibration of the cameras.

In general, the object subjected to loading is viewed by two CCD cameras. A random pattern marking is sprayed onto the object surface which deforms simultaneously with the object. The deformation of the marking under different loading conditions is recorded by both CCD cameras as an image sequence. The initial post processing defines the macro facets in the reference image from the left camera and compared with the right one, the coordinates of every facet with respect to the selected start point are allocated automatically. These facets are tracked in each successive image with sub-pixel accuracy. By comparing the images, ARAMIS can register any displacement on the surface of the object using photogrammetric principles, yielding the precise 3D coordinates on the surface

of the specimen related to the facets at each stage of deformation, from which the strains are derived. At last, ARAMIS is able to process and visualize the results in diagrams or 3–D meshes so as to obtain the distribution of strain on the surface of the measured object at various stages. For more details on the features of the ARAMIS system and its usage, refer to GOM [40] and [4] and to Qu [77].

1.3. Scope and Outline

Chapter 2 contains homogeneous and inhomogeneous compressive experiments carried out using polycarbonate at three different true strain rates and three different temperatures. First, an introduction to the conditions necessary for the correct execution of the experiments is given, which include temperature and strain rate regulation among others. The principals of the calculation of true stress and true strain from the gathered experimental data are explained in detail. The experimental set-up and the employed hardware are introduced for the cases of uniaxial- and pure shear compression experiments. The ins and outs of the experimental methodology followed in the execution of the experiments are presented and the results obtained are discussed and interpreted. Furthermore, thermomechanical experiments under uniaxial compression are included to round off the spectrum of phenomena observable with these type of tests.

In **Chapter 3**, inhomogeneous tensile experiments performed using dumbbell shaped flat specimens are presented. The main steps followed during the execution of these type of tests by means of the optical measurement equipment known as ARAMIS are intensely discussed and a standardized experimental procedure is put in place in order to be consistent across all the tensile experiments. Key factors such as illumination, camera alignment, system calibration or specimen coating are explained. First, the results obtained directly from the testing machine in the form of load-displacement diagrams are presented for one deformation rate and three different temperatures. Afterwards, the three-dimensional inhomogeneous strain distributions captured from the surface of the specimen during deformation are shown and synchronized with the load-displacement diagrams, facilitating a better understanding of the necking process. By use of the obtained three-dimensional strain distributions the temperature dependency of the neck velocity is studied for the employed deformation rate.

Chapter 4 contains the basic guidelines for a constitutive model aiming to capture the mechanical behavior of glassy polymers via computer simulations based on the previously presented experimental results. For this purpose a model of thermo-elasto-visco-plasticity of glassy polymers is presented. The framework of additive kinematics in the logarithmic strain space is introduced in a modular form. A thermomechanical constitutive model of glassy polymers is presented together with two different temperature dependent micromechanical models for the plastic flow, namely, the double-kink theory and a model based on the distribution of free volume. The algorithmic setup required to solve, in a staggered manner, the coupled differential equations governing the deformation is presented. This chapter is further supplemented by the Appendices A and B where the derivation of the back stresses of the formulation is shown in detail.

In **Chapter 5**, the properties of the presented constitutive models, to resemble the material response measured via experiments, will be dealt with. This so-called *model validation* intends to evaluate the material laws by revising their performance under different temperatures and deformation rates. Initially, the material parameters entering the constitutive

equations are identified by trial and error for which specific guidelines are introduced in order to perform the identification as efficiently as possible. The main mechanical parameters are obtained from homogeneous compression experiments by fitting the experimental data of uniaxial and plane strain compression. Once this is completed, BVP's resembling the inhomogeneous tension experiments are solved and the results obtained are compared with the load-displacement curves and the three-dimensional strain distributions previously obtained.

2. Homogeneous and Inhomogeneous Compression Experiments

This Chapter contains the compression experiments later used to identify the material parameters appearing in constitutive laws intended to model the material behavior of glassy polymers. First, isothermal homogeneous compression experiments in two deformation modes, namely uniaxial compression and pure shear, are presented. Later, thermomechanical compression experiments minded to study the softening effect due to the accumulation of heat during deformation will be introduced. As has been found by Boyce & Arruda [17], Arruda, Boyce & Jayachandran [11] and other researchers, polycarbonate, like other glassy polymers such as PMMA, shows strong dependencies on both the temperature and the mechanical conditions under which it is deformed. In the subsequent chapters the main parameters to be observed for successfully controlling these dependencies during the course of an experiment are detailed as much as possible.

2.1. General Testing Conditions for Compression Experiments

Experimental procedures have to be regulated and strictly followed to achieve the same initial conditions before testing. Among other factors it must be observed: thermal equilibrium in both specimen and metal platens, a uniform lubrication, and a loading function deforming the material at a constant true strain rate. Even if the latter was enforced, possible modes of inhomogeneous deformation such as barreling, shearing, and buckling of the specimen still may occur when deforming the material under compression, which will yield inhomogeneous stress distributions along the test pieces. Nevertheless, by means of an appropriate lubrication and keeping the height-to-diameter ratio small, the above mentioned phenomena can be largely avoided.

2.1.1. Isothermal Testing Conditions. In the above cited literature a significant temperature rise has been observed at the true strain rates of $\dot{\epsilon} = -0.01$ s^{-1} and $\dot{\epsilon} = -0.1$ s^{-1} at room temperature in compression experiments as a clear sign of the adiabatic heat generated during deformation that can not be dissipated to the surroundings. On the other side, at a rate as low as $\dot{\epsilon} = -1 \times 10^{-3}$ s^{-1} isothermal deformation conditions were obtained in the material as verified by the nearly flat temperature response measured by the infrared detector used in Arruda, Boyce & Jayachandran [11]. Therefore, the series of compression experiments presented in this subchapter intend to isolate the effect of adiabatic heating by using true strain rates $\dot{\epsilon}$ of the order of -1×10^{-3} s^{-1}, -5×10^{-4} s^{-1} and -1×10^{-4} s^{-1} to allow maximum dissipation of the heat generated during the deformation of the specimen. These experiments were conducted at three different temperatures, namely 23 °C, 50°C and 75°C to study the well-known temperature dependency of the mechanical response.

2.1.2. Pre- and Post-Processing of the Data. The fact that the experiments under compression will be carried out at a constant true strain rate $\dot{\epsilon}$ requires the incorporation of additional parameters into the employed experimental setup with the aim that the applied displacement function induces a true strain deformation regime on to the material. Once the experiment has been carried out and the data has been captured it must be post-processed to transform the measured displacements into true strain and the applied load into true stress.

Determination of the Displacement Function. In order to apply a constant true strain rate to the test piece using the MTS machine in displacement control mode, a

displacement function must be derived. We start with the time derivative of (1.4)

$$\dot{\epsilon} = \dot{\overline{\ln \lambda}} = \frac{\dot{\lambda}}{\lambda} = \text{const} \tag{2.1}$$

where λ, the stretch ratio introduced in (1.3), can be expressed in terms of the time-dependent displacement function $u(t)$ in the form

$$\lambda = \frac{l}{l_0} = \frac{l_0 + u(t)}{l_0} \ . \tag{2.2}$$

From (2.1) the evolution of the stretch in time can be obtained

$$\dot{\lambda} = \lambda \dot{\epsilon} \ . \tag{2.3}$$

Integrating (2.3) via convolution integral representation yields $\lambda(t) = \exp(\epsilon(t)) - 1$. Insertion of (2.2) and taking the initial condition $\lambda(t = 0) = 1$ gives finally the displacement function

$$u(t) = l_0\big(\exp(\dot{\epsilon}t) - 1\big) \tag{2.4}$$

with $\epsilon(t) = \dot{\epsilon}t$. The latter expression is preferred since the inclusion of an explicit true strain rate $\dot{\epsilon}$ in the formulation is desired. However, the motion controller of the MTS machine is based on a linear displacement algorithm and can not execute exponential functions, therefore an approximation of the displacement function by several linear segments as depicted in Figure 2.1a was carried out.

Computation of the True Strain-True Stress Diagram. As mentioned in previous chapters, the displacement function is inputed to the testing machine in order to perform experiments at constant true strain rate and collect the load F and displacement $u(t)$ at a specified interval of time. The post-processing of the data involves the computation of the true stress and true strain values. The true strain can be computed from (1.4) by insertion of $(2.2)_3$

$$\epsilon = \ln \lambda = \ln \left(1 + \frac{u(t)}{l_0}\right) \ . \tag{2.5}$$

The true stress is per definition $\boldsymbol{\tau} = J\boldsymbol{\sigma} = \boldsymbol{P}\boldsymbol{F}^T$, with its 1–D counterpart $J\sigma = P\lambda$. Taking into consideration the incompressibility condition $J := \det \boldsymbol{F} = 1$, we get

$$\sigma = P\lambda \tag{2.6}$$

where the first Piola-Kirchoff stress is defined as

$$P = \frac{F}{A_0} \ . \tag{2.7}$$

Substituting (2.7) in (2.6), we get

$$\sigma = \frac{F\lambda}{A_0} \tag{2.8}$$

in which A_0 stands for the initial cross-section area of the specimen.

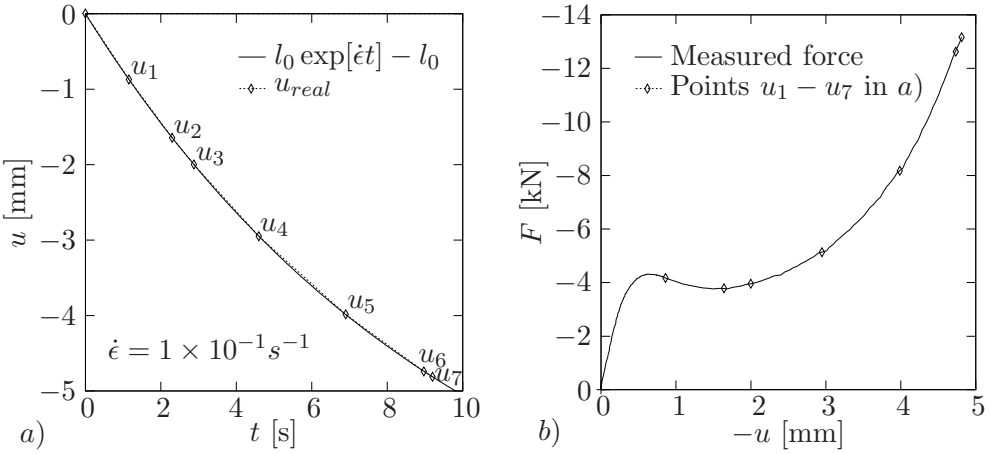

Figure 2.1: *a*) Exponential loading curve employed in compression experiments (here shown for the fastest true strain rate). The maximum true strain attained for uniaxial compression experiments is $\epsilon_{max} = -1.15$ ($u_{max} = -4.81$mm for $l_0 = 8$mm). *b*) Load–displacement curve obtained directly from the testing machine.

Calculation of the Compliance Factor of the Testing Machine. In order to analyze the response of the material on which the experiments are being performed, the impact of the stiffness of the axis rods on the output data should be considered. As the applied load increases, a small part of the measured displacement is absorbed by the axis rods themselves and becomes significant towards the end of the compression experiments where the applied load can reach 10kN or more. Even though the rods posses a complex geometry that difficults the theoretical computation of the displacements caused by load, their linear elastic response can be idealized as follows. Considering the stiffness of the upper axis as C_2 and that of the lower axis rod as C_1, the applied load F can be written as

$$F = C_1(u_1 - u_2) = C_2\ u_3 \tag{2.9}$$

as shown in Figure 2.2. The term u_1 refers to the displacement of the lower end of the bottom axis, u_2 is the value of the displacement of the upper end of the bottom axis and u_3 refers to the displacement of the lower end of the top axis. The net deformation in the specimen is given as

$$u_2 - u_3 = u_1 - \left(\frac{F}{C}\right) \tag{2.10}$$

where $C := \frac{C_1 C_2}{C_1 + C_2}$. Now the true strain can be computed from (1.3) and (1.4) yielding

$$\epsilon = \ln\left(\frac{l}{l_0}\right) = \ln\left(\frac{u_2 - u_3}{l_0}\right)\ . \tag{2.11}$$

Substituting $(2.10)_2$ in $(2.11)_2$ finally gives

$$\epsilon = \ln\left(\frac{u_1 - \left(\frac{F}{C}\right)}{l_0}\right) \tag{2.12}$$

with the load-dependent displacement correction factor F/C. A value of $C = 2.3 \cdot 10^5$ will be employed to display all the compression experiments presented in this work. Due to the fact that the effect of the contraction of the rods is much larger than the bending of

the traverse or the movement that could be absorbed by the actuating cylinder at higher loads, the *machine elasticity* is here neglected differently with what Bowden [16] (pp. 290) suggested.

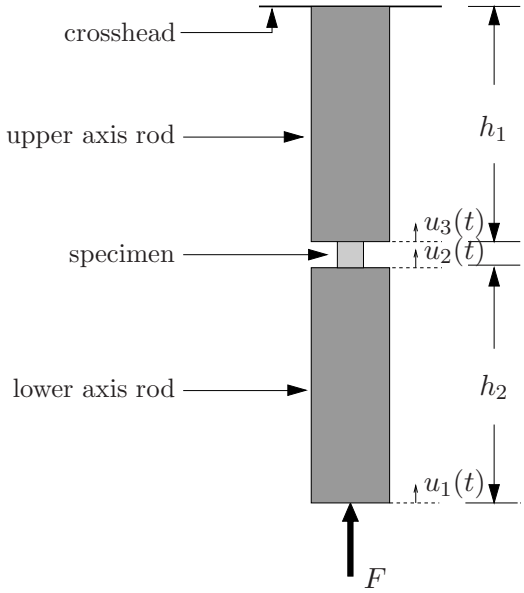

Figure 2.2: Arrangement of a specimen in an Uni-axial compression test.

2.1.3. Temperature Evolution in the Specimen and Metal Plates. One of the crucial steps in the experimental setup presented here is to bring both the specimen and the metal dies to the exact environmental temperature before the experiment begins. This is not a trivial task since an inhomogeneous temperature distribution throughout a piece made out of a glassy polymer would immediately yield inaccurate results due to the several local stiffnesses that the material would present depending on the temperature at different points along its geometry. Hence, the time that the components inside the environmental chamber are left to reach the desired temperature prior to an experiment becomes relevant. In this regard, a study was conducted to observe the evolution of temperature in the specimen and plates soon after they were placed inside the environmental chamber. In order to measure the temperature inside the cylindrical specimen, a special tool was devised having the same geometry as those used for real tests. It was cut into two parts, having a screw and thread mechanism to be assembled together enabling the inclusion of a ring-thermocouple in between to measure the temperature of the material to be tested. This thermocouple was plugged into a Raytek infra-red thermometer used to transfer and record the temperature data in a computer. At the same time the evolution of the temperature in the plates was manually read and recorded using a second thermocouple. This study was conducted for each testing temperature, namely 50°C and 75°C.

The outcome of this study can be seen in Figure 2.3a for the case of 50°C. The results indicate that the specimen reached the desired temperature in approx. 50 min, whereas the plates required 100 min. As shown in Figure 2.3b, for the case of 75°C, the specimen and metal plates require 60 min and 100 min respectively. While conducting the experiments at both temperatures, the time elapsed between placing the specimen inside the heated environmental chamber and the testing machine carrying out the experiment was taken to be 120 min, which largely surpasses the suggested values of Dupaix & Boyce [32]

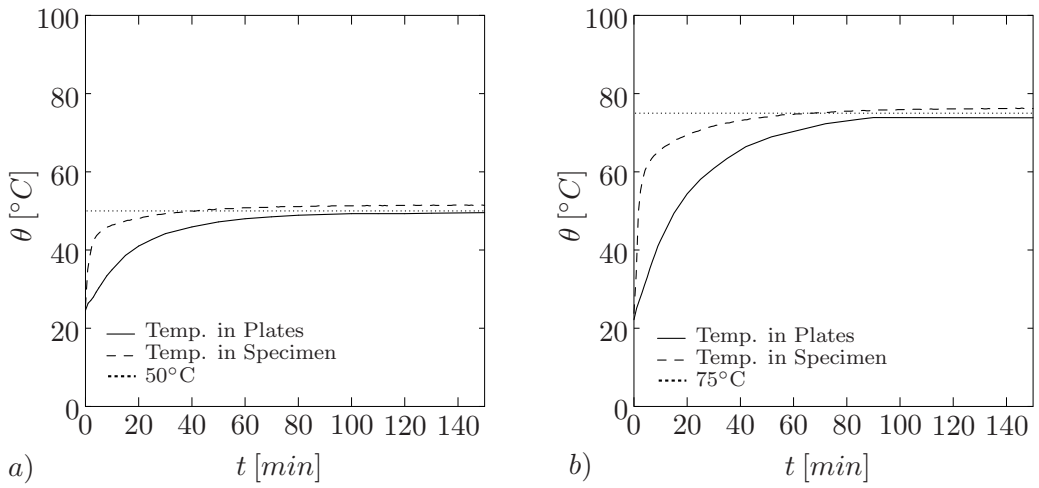

Figure 2.3: Temperature evolution in the specimen and metal plates for the case of uniaxial compression experiments. *a*) Test temperature $\theta = 50°C$. *b*) Test temperature $\theta = 75°C$.

(20min) and Melick, Govaert & Meijer [62] [63] (15min). For more details on this procedure see Iyer [52] and Qu [77].

2.2. Uniaxial Homogeneous Compression Tests

2.2.1. Experimental Setup. Cylindrical specimens having a dimension of $\phi 8$ mm $\times$ 8 mm were used for this purpose, see Figures 2.4a and 2.14a. As it can be seen in Figure 2.14d, the consequences of wrong lubrication or incorrect positioning of the specimen are manifested in the form of barreling and shearing of the tested specimens, leading to a softer response of the material. However, these undesired effects can be sufficiently eliminated by the use of adequate lubrication. For the case of barreling, two circular Teflon films having a slightly greater diameter than the specimen itself were placed on top and bottom of it. Teflon film has the convenient property of deforming together with the faces of the specimen in contact with the metallic dies, considerably reducing the friction at those sensitive points.

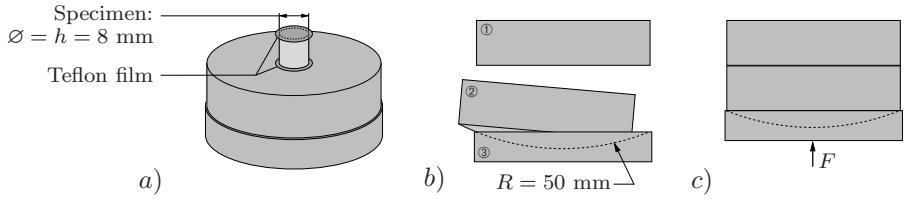

Figure 2.4: *a*) Sketch of the lower die with the loading setup for uniaxial compression tests. *b*) Device before alignment. ①Upper, fixed die. ②Upper part of the spherical die. ③Lower part of the spherical die. *c*) Aligned upper and lower dies after applying a force $F \sim 20$kN.

To further avoid barreling, a small amount of the commercial lubricant WD–40 was applied between each Teflon film and the metal plates. Additionally, a convex spherical self-adjusting seat, as suggested by Boyce & Arruda [17] and Arruda, Boyce & Jayachandran [11], was placed on the lower concave plate with silicon-based lubricant uniformly smeared in between. This construction chiefly helps to maintain the upper and lower metal plates parallel, avoiding shearing in the deformed specimen. A picture of this arrangement is illustrated in Figure 2.4b and 2.4c.

2.2.2. Results and Observations. After the implementation of the above mentioned testing conditions and techniques, isothermal uniaxial compression experiments were carried out. The load F[kN] and displacement u[mm] data were measured by the sensors and stored at intervals of 2 sec for the fastest true strain rate ($\dot{\epsilon} = -1 \cdot 10^{-3}$ s^{-1}) and 5 sec for the intermediate and slowest true strain rates ($\dot{\epsilon} = -5 \cdot 10^{-4}$ s^{-1} and $\dot{\epsilon} = -1 \cdot 10^{-4}$ s^{-1} respectively). Figure 2.1b shows a typical load-displacement curve obtained from the testing machine. It is important to mention that the first linear segment u_1, in which the displacement function was discretized, ends after the yield point. This is desirable since the small holding time between linear segments of the displacement function could yield in an inaccurately acquired yield point if this change in slope took place at a value close to it. The resulting true stress-true strain response of the tested polycarbonate was post-processed from the load-displacement data based on (2.5) and (2.8) and plotted in Figure 2.5.

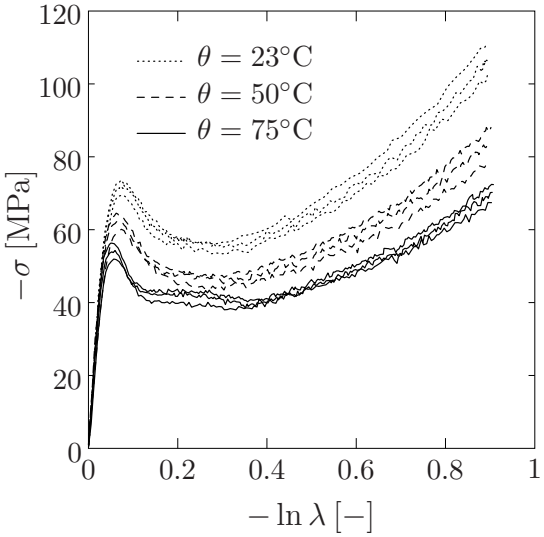

Figure 2.5: True stress vs. true strain curves of the uniaxial compression experiments revealing the true strain rate- and the temperature dependency of polycarbonate. The rates $\dot{\epsilon} = -1 \cdot 10^{-3}$ s^{-1}, $\dot{\epsilon} = -5 \cdot 10^{-4}$ s^{-1} and $\dot{\epsilon} = -1 \cdot 10^{-4}$ s^{-1} at each temperature are not explicitely marked but it should be noted that the stiffer the observed response, the higer the corresponding true strain rate.

The observed behavior of polycarbonate under uniaxial compression shows a sharp elastic response within a small range of true strain followed by a nonlinear elastic-inelastic transition up to the occurrence of yielding. Strain softening, which takes place in the post yield region, is followed by temperature dependent strain hardening. From Figures 2.6a to 2.6c it can be clearly observed that at fixed temperature the yield stress is higher for higher true strain rates. Furthermore, the employed true strain rates do not greatly affect the amount of strain softening at different temperatures. However, it must be noted that this low true strain rates were intentionally employed to avoid the accumulation of heat in the cylindrical specimen, thus at this point it is not possible to conclude that the true strain rate has no major effect on the softening as a whole. Similarly, there is no major dependency of the true strain rates on the amount of strain hardening at each temperature.

In Figures 2.6d to 2.6f the effect of temperature on the yield point can be observed for each true strain rate. At higher temperature, the yield value is significantly lower. How-

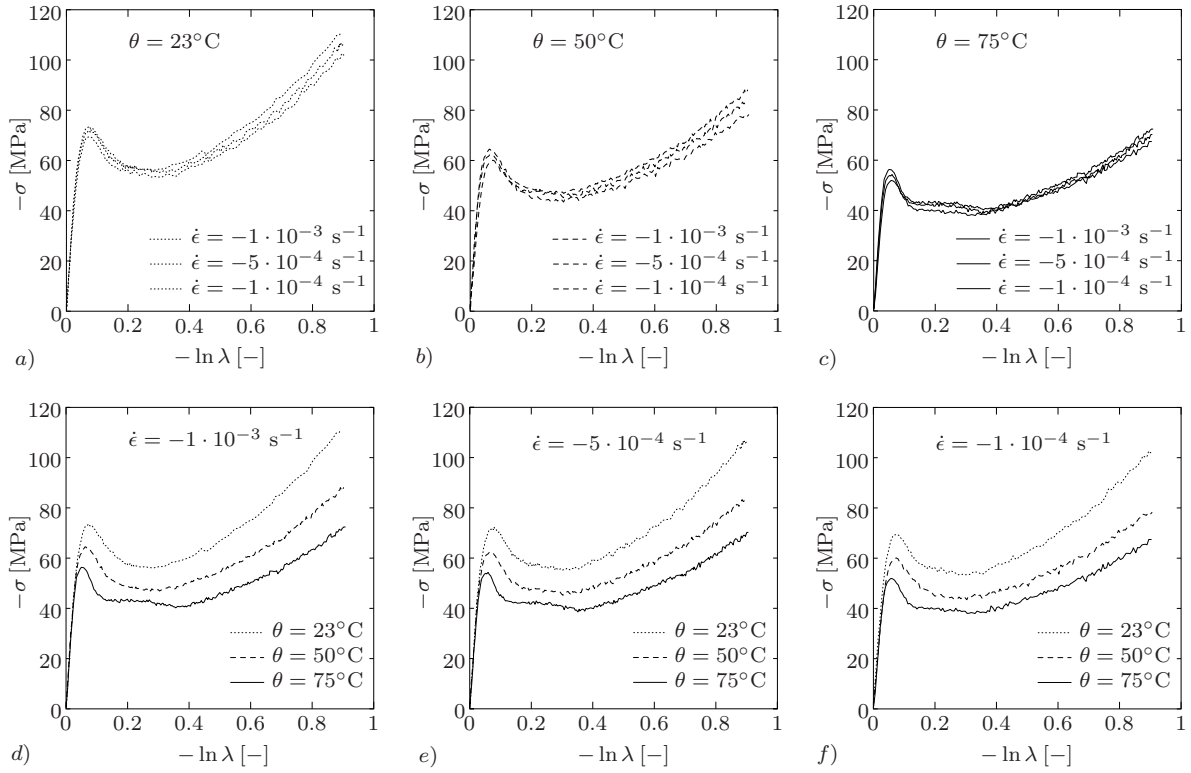

Figure 2.6: True stress vs. true strain plots of the uniaxial compression experiments. *a)* to *c)* true strain rate dependency: *a)* $\theta = 23°\text{C}$. *b)* $\theta = 50°\text{C}$. *c)* $\theta = 75°\text{C}$. *d)* to *e)* temperature dependency: *d)* $\dot{\epsilon} = -1 \cdot 10^{-3}$ s^{-1}. *e)* $\dot{\epsilon} = -5 \cdot 10^{-4}$ s^{-1}. *f)* $\dot{\epsilon} = -1 \cdot 10^{-4}$ s^{-1}.

ever, the amount of strain softening in the post-yield region is not highly influenced. It has also been found that the yield strain is shifted towards lower values as the temperature increases. This is due to the fact that amorphous glassy polymers show a high viscoelasticity at temperatures around T_g, but well below it, the slope of the initial viscoelastic region does not change much at different temperatures, leading to a shift of the yield strain with respect to the variation of the yield stress, for example, in the small strain region the response of the material at the true strain rate $\dot{\epsilon} = -1 \cdot 10^{-3}$ s^{-1} is identical up to a true stress of approx. −50MPa regardless of the temperature (see Figure 2.6d). The amount of strain hardening which can be characterized by the slope of the curve after strain softening also depends on the temperature to some extent: as the temperature increases, the slope decreases, implying a drop in the amount. Furthermore, from Figures 2.6a to 2.6c it can be seen that at an increment in temperature reduces considerable the material rate dependency, i.e. in Figure 2.6a the displayed plots are more spaced from each other than that in Figure 2.6c.

An interesting feature of this material arises at 75°C where for all three true strain rates the same *plateau* in the strain softening is observed (see Figure 2.6c). Initially we attributed the appearance of this plateau or loss of curvature to a rise in friction when deforming the cylindrical specimens. The experiments at $\theta = 75°\text{C}$ were repeated yielding always a homogeneously deformed piece and the same true strain-true stress curve. At this temperature the part of the material molecular network that dissociates seems to impact the region between the end of softening and the beginning of hardening, reaching its extreme in Figure 2.6f where the deformation of the material takes place in the mentioned region under almost constant true stress, i.e. part of the strain softening

and hardening seems to be replaced by a plateau.

2.3. Plane Strain Compression

As an extension to the already-presented experimental work on homogeneous compression experiments on polycarbonate, plane strain compression tests were carried out. The experimental setup is similar to that described in Dupaix & Boyce [32] on PETG, but unlike the way they proceeded, another standardized procedure was rigorously planned and followed during this work.

2.3.1. Specimen Preparation. Test specimens with cross section of 8×8 mm were machined from injection moulded cubic blocks with transverse area of 10×10 mm and height of 15 mm. Prior to testing, the pieces were stored in an ambient environment at room temperature and normal humidity. Trial experiments were conducted using specimens of 8 mm in height, see Figure 2.7a (left). Independently of how carefully

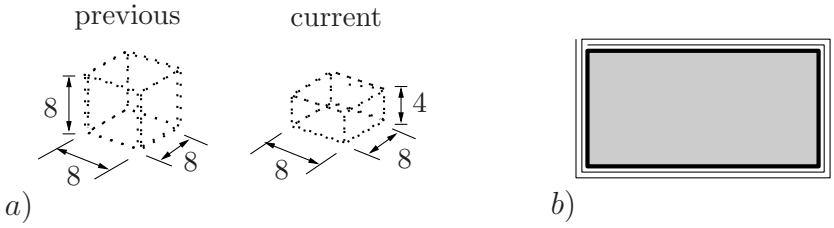

Figure 2.7: *a*) Previous and current dimensions (in mm) of the specimens used in the plane strain compression experiments. *b*) Sketch of the the packaging method of the specimen with teflon film.

the lubricant was applied, the deformed test samples were strongly bulged and barreled, leading to a second stress drop in the corresponding true stress-true strain curve. This negative effect can be mainly attributed to the severe friction developed between the channel die and the specimen surface. This phenomenon also appeared in the experimental curve based on the plane strain compression data of polycarbonate reported by Boyce, Arruda & Jayachandran [18]. They attributed this awkward response to diffuse micro-shear banding presented at moderate strains ($< -30\%$) but still considered the deformation to be *globally homogeneous* or *macroscopically homogeneous*. In order to relax the effect of friction from the material response and exclude the second stress-drop phenomenon, the specimen's height was then stepped down to 4 mm, as depicted in Figure 2.7a (right), and the specimen was then wrapped up with two full folds using a sheet of Teflon film. Figure 2.7b also gives the illustration of the standardized folding method. Based on these treatments, it turned out to have largely alleviated the above mentioned problems. Figure 2.8a and 2.8b show the improvement of the experimental results and Figure 2.8c gives a picture of the shapes of the undeformed and deformed specimens with different heights. From the latter it can be clearly seen that the specimen with 4mm in height deforms homogeneously when subjected to pure shear deformation, whereas the one with 8mm in height gives the typical *barreled* shape caused by friction.

2.3.2. Standardized Experimental Procedure. After warming up the MTS machine for 20 min with cycling amplitude of total 90 mm and at a frequency around 0.10 Hz, one specimen was wrapped up with a Teflon film as described in Chapter 2.3.1. Following that, the enfolded specimen was hanged in the upper corner of the channel die which is

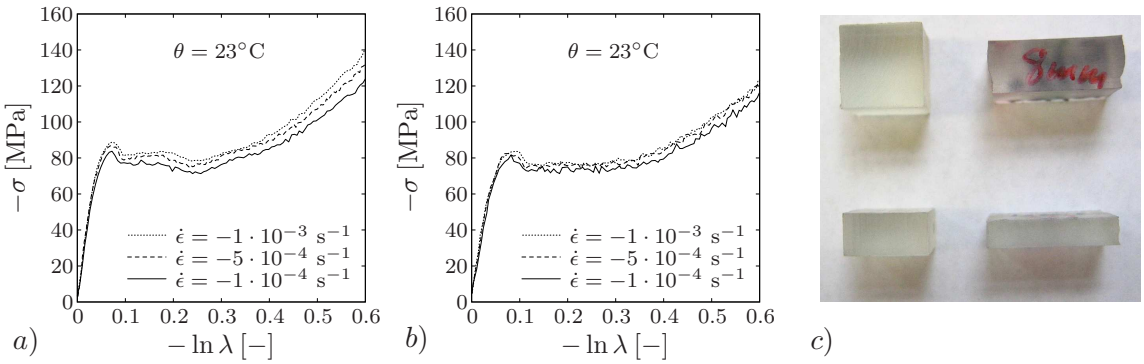

Figure 2.8: Reduction of the second stress drop in the true stress-true strain diagram of the plane strain compression experiments at different true strain rates under 23°C by use of specimens of height *a*) 8mm and *b*) 4mm. *c*) Comparison between the undeformed (left column) and deformed (right column) specimen configurations with heights of 8 mm (upper row) and 4 mm (lower row).

depicted in Figure 2.9a. Upon setting the temperature to a desired value, the chamber was turned on to heat up the whole testing environment with the chamber door closed for at least 100 min in order to achieve thermal equilibrium in both the specimen and the channel die. After that, a commercial lubricant, WD–40, was applied in the channel die and also on top of the Teflon film to reduce the friction and avoid shearing effects. Complying with the suggestion from the provider of WD–40 [5], care was taken so that no lubricant got in touch with the specimen. Afterwards, the specimen was finally positioned into the center bottom of the channel die (see Figure 2.9b) and closed with a cubic punch. More waiting time, approximately 20 min, was also compulsory to counterbalance the considerable heat loss of the chamber while lubricating and positioning the specimen, which induced more or less 5°C drop in temperature. Finally, the specimen was pre-loaded with 300 N to press out the specimen, the Teflon film, and the punch (see Figure 2.9c).

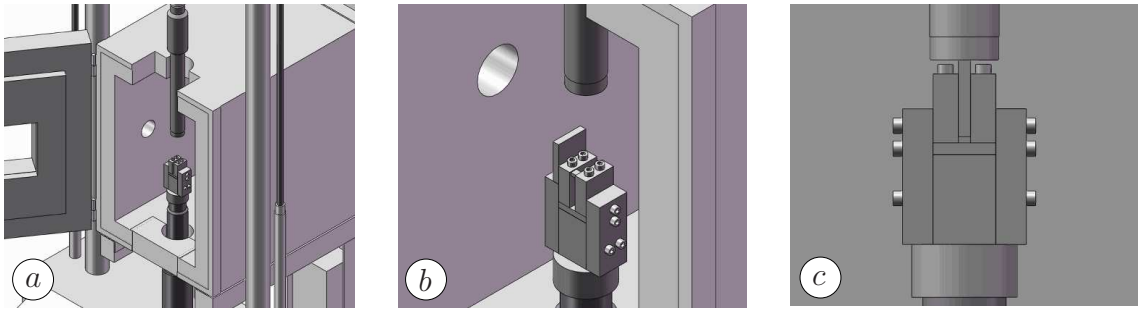

Figure 2.9: *a*) Testing machine and environmental chamber assembled together for the pure shear compression experimental setup. *b*) The specimen and the upper die are placed inside the chamber to be warmed up to the testing temperature. *c*) Full assembly ready for testing. The heated cubic specimen has been moved to the bottom of the lower die and the upper die has been placed on top of it.

Test samples were compressed at the already mentioned temperatures and *isothermal* true strain rates to the final true strain of -0.68 (corresponding to a final height of the specimen of ≈ 2 mm). The regulation of the temperature was performed identically as for the case of uniaxial compression experiments.

2.3.3. Results and Observations. If under uniaxial compression repeatability was already complicated to acquire, under plane strain compression this becomes even more difficult, compelling to perform many experiments to evaluate it. The results presented here, plotted in Figure 2.10, were selected from the mentioned parallel repeating experiments taking into consideration the final geometries of the deformed test samples. The strain rate dependency is shown in detail in Figure 2.11a-c and the temperature dependency can be seen in Figure 2.11d-f. An interesting plot is the one in Figure 2.12 showing the deformation state dependency of the material, i.e. a comparison of the uniaxial compression and the pure shear results. The compliance factor C also had to be taken into account in this case since the maximum force applied by the testing machine largely exceeded the one applied in uniaxial compression experiments. The overall repeatability of the plane strain compression experiments will be further discussed in Chapter 2.3.4.

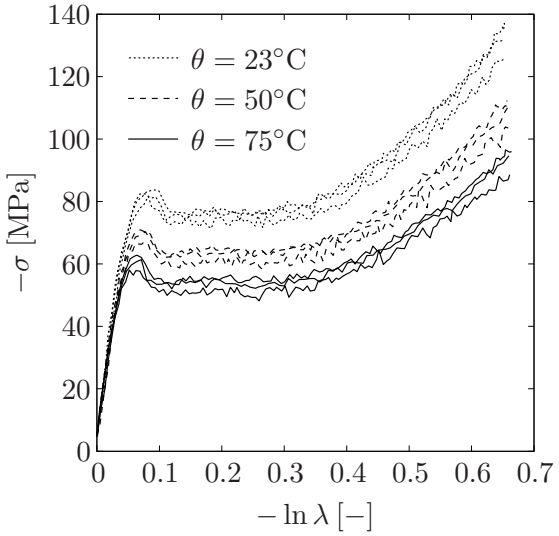

Figure 2.10: True stress vs. true strain results of the plane strain compression experiments revealing the true strain rate- and the temperature dependency of polycarbonate. The rates $\dot{\epsilon} = -1 \cdot 10^{-3}$ s^{-1}, $\dot{\epsilon} = -5 \cdot 10^{-4}$ s^{-1} and $\dot{\epsilon} = -1 \cdot 10^{-4}$ s^{-1} at each temperature are not explicitely marked but it should be noted that the stiffer the observed response, the higer the corresponding true strain rate.

As for the case of uniaxial compression, the true strain rate was also found to affect the yield stress under pure shear. Figure 2.10 shows this relatively small effect at each testing temperature. Again, the amount of the strain softening as well as the strain hardening appeared to be relatively independent of the employed true strain rates similar to that shown in Chapter 3.1.4. In Figure 2.11 can be observed that there is a pronounced drop in yield stress with an increase in temperature even though the amount of strain softening does not appear to strongly depend on it. The strain hardening is found to depend less on temperature than uniaxial compression, i.e. compare for example Figures 2.6d and 2.11d. In the latter the slope of the strain hardening seems to be the same at all three temperatures, whereas in Figure 2.6d the curves at this stage seem to *diverge*. Similarly to uniaxial compression, under pure shear the yield strain is shifted to lower values as the temperature is increased.

Deformation State Dependency. In Figure 2.12 two states of deformation can be seen manifesting almost the same behavior in the elastic range. This consists of a dramatic stress increase confined to small true strain values. However, due to the solid

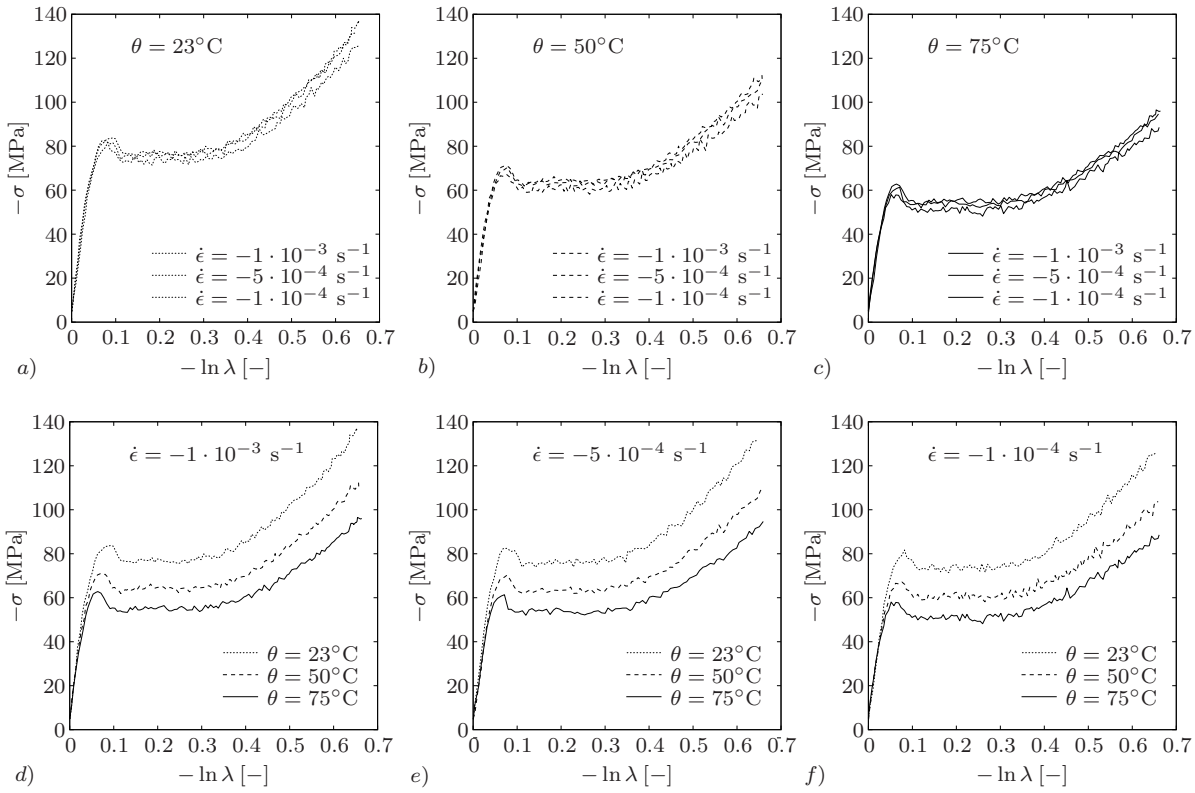

Figure 2.11: True stress vs. true strain results of the plane strain compression experiments. *a*) to *c*) true strain rate dependency: *a*) $\theta = 23°C$. *b*) $\theta = 50°C$. *c*) $\theta = 75°C$. *d*) to *e*) temperature dependency: *d*) $\dot{\epsilon} = -1 \cdot 10^{-3}$ s^{-1}. *e*) $\dot{\epsilon} = -5 \cdot 10^{-4}$ s^{-1}. *f*) $\dot{\epsilon} = -1 \cdot 10^{-4}$ s^{-1}.

constraint of the channel die which reduces the freedom of motion by one degree, plane strain compression exhibits a stronger stress response in both yield and post yield regions comparing with uniaxial experiments carried out under the same conditions. The difference in yield stress does not seem to rely on the deformation rate but on the temperature if the figures are compared vertically (true strain rate dependency) and horizontally (temperature dependency). The higher the temperature, the smaller the difference in yield stress of the two deformation modes. In addition, the variation of the stresses in the post yield region also becomes smaller with increasing temperature.

2.3.4. Repeatability. Under pure shear conditions, much higher loads have to be applied to the specimen in order to deform it. This means that the probability of obtaining an inhomogeneous, and therefore non-repeatable, result increases. With the aim of confirming this repeatability 8 experiments under plane strain compression were carried out under each strain rate and temperature. In addition, the final profiles of the employed specimens were also taken into account to assess the repeatability, among which 3 to 4 experimental results under each test condition were selected and compared in Figure 2.13. Despite the small differences throughout the whole true stress-true strain diagram due to unavoidable friction, the results of the repeating experiments fit each other in a sufficient manner. As it can be seen in Figures 2.13a and 2.13c, at lower true strain rates the repeatability seems to worsen. This might have a rather technical than micromechanical origin since a true strain rate as low as $\dot{\epsilon} = -1 \cdot 10^{-4}$ s^{-1} demands very high accuracy from the feed back control of the testing machine, making it more difficult to comply with when the load reaches the hardening region towards the end of the experiment.

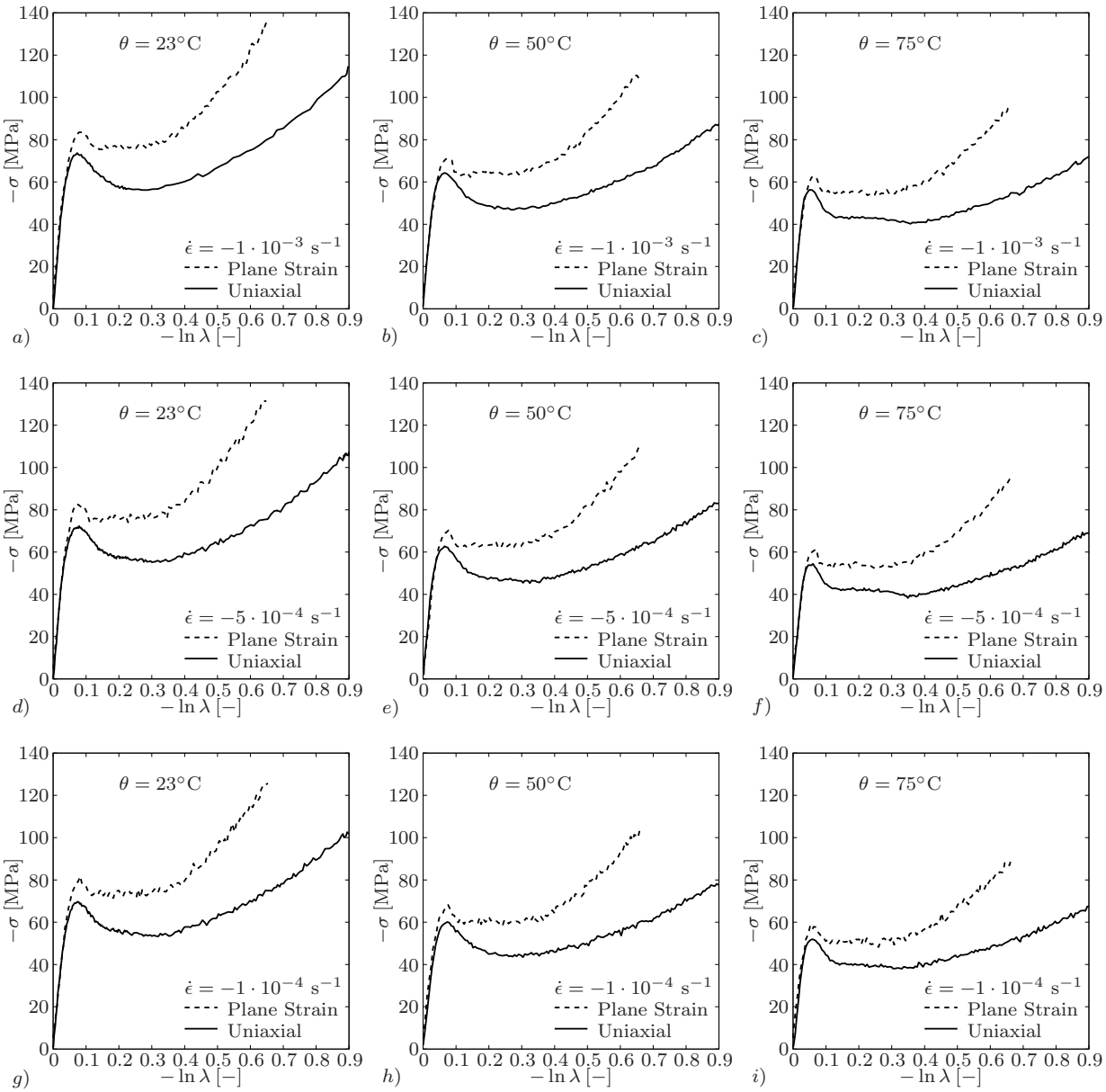

Figure 2.12: Comparisons of true stress vs. true strain results between uniaxial and plane strain compression experiments at different true strain rates and temperatures.

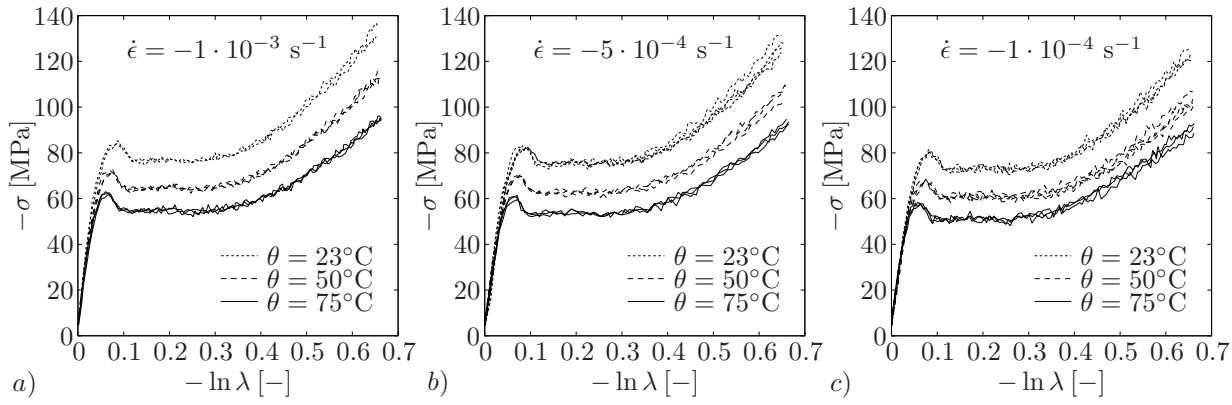

Figure 2.13: Repeatability of the plane strain compression experiments at different true strain rates and temperatures. At a constant true strain rate of *a)* $\dot{\epsilon} = -1 \cdot 10^{-3}$ s^{-1}. *b)* $\dot{\epsilon} = -5 \cdot 10^{-4}$ s^{-1}. *c)* $\dot{\epsilon} = -1 \cdot 10^{-4}$ s^{-1}.

2.4. Thermo-Mechanical Uniaxial Compression Experiments

In order to enrich the set of experimental results presented so far in this work, additional *inhomogeneous* thermomechanical uniaxial compression experiments were carried out using cylindrical specimens at 23°C (room temperature) and 2 different constant true strain rates, namely $\dot{\epsilon} = -1 \cdot 10^{-1}$ s^{-1} and $\dot{\epsilon} = -1 \cdot 10^{-2}$ s^{-1}. The intention of using the above mentioned true strain rates was to deliberately increase the temperature of the specimen via deformation, giving room for additional thermomechanical effects within the material such as the thermal softening caused by adiabatic heating. These kind of experiments are termed *inhomogeneous* since the temperature increment caused by the above true strain rates is not homogeneously distributed throughout the specimen, yielding a barrel-formed deformed test piece. This can be clearly seen in Figure 2.14 where the initial geometry of a cylindrical specimen (Figure 2.14a) is displayed together with the final shape of a specimen deformed isothermally under uniaxial compression (Figure 2.14b) and the final shape of a specimen deformed thermomechanically using the two higher true strain rates mentioned above (Figure 2.14c).

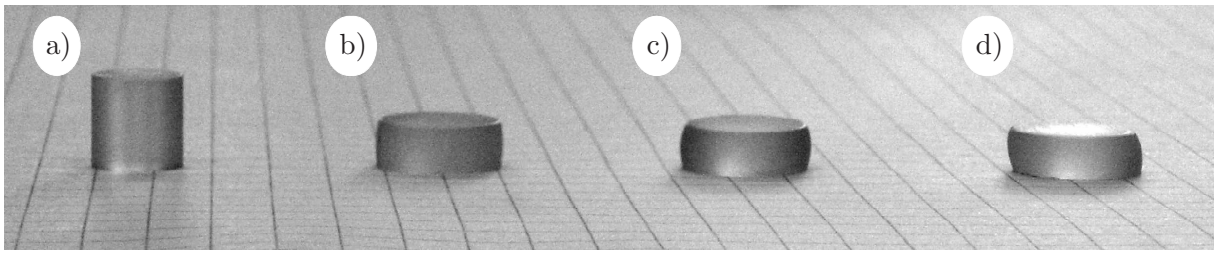

Figure 2.14: a) undeformed specimen, b) specimen deformed *isothermally* at $\dot{\epsilon} = -2 \cdot 10^{-4}$ s^{-1}, c) specimen deformed *thermomechanically* at $\dot{\epsilon} = -1 \cdot 10^{-1}$ s^{-1} presenting barreling due to inhomogeneous distribution of temperature, d) sheared specimen.

Since the thermomechanical behavior of glassy polymers was the aim of these new set of experiments, these were carried out only at room temperature ($\theta = 23$°C) to isolate this phenomenon from further thermal influences. The testing conditions for this uniaxial compression experiments as well as the pre- and post-processing of the experimental data were the same as those described in Chapter 2.1. The experimental procedure followed was similar to the one described in Chapter 2.2.1 with the only discrepancy that the fastest true strain rate, $\dot{\epsilon} = -1 \cdot 10^{-1}$ s^{-1}, brought new difficulties to the experimental procedure since the duration of an experiment at this true strain rate (~ 5 seconds) was considerably shorter than those made before. This, in conjunction with hardware and software constraints, resulted in a missed data aquisition from the linear elastic region up to the yield point. To solve this problem the recording of the experimental data had to be initiated 5 seconds before the actual deformation started. For more details on the execution of experiments at higher true strain rates the reader is referred to Weigert [92].

2.4.1. Results and Observations. The true stress-true strain diagrams in Figure 2.15 present the experimental results obtained at the laboratory. Various experiments at each true strain rate had to be made to exclude mistakes in the setup and secure repeatability. The rate dependency of the yield point, following the tendency already shown by polycarbonate when deformed under isothermal conditions, is reduced but existent. The overall mechanical response seems to be the same for both rates up to the end of the

strain softening, where the heat that could not be dissipated to the surroundings for the case of the fastest rate begins to impact the strain hardening of the material. This explains why the two curves in Figure 2.15 tend to cross each other towards the end of the experiment, being this chiefly caused by a temperature-softening under the true strain rate $\dot{\epsilon} = -1 \cdot 10^{-1}\text{s}^{-1}$. For the true strain rate $\dot{\epsilon} = -1 \cdot 10^{-2}$ s^{-1} the influence of the non-dissipated heat seemed to have faded away by the time that the strain–hardening was reached. This will be later supported by the simulation of these experimental results.

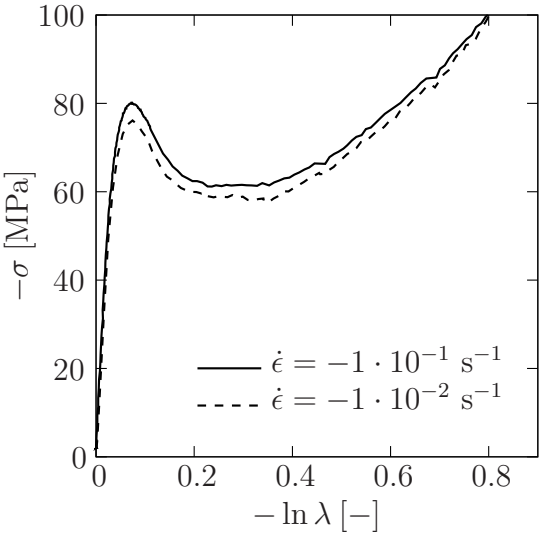

Figure 2.15: True stress–true strain diagrams of the uniaxial compression experiments for the true strain rates $\dot{\epsilon} = -1 \cdot 10^{-1}$ s^{-1} and $\dot{\epsilon} = -1 \cdot 10^{-2}$ s^{-1} at room temperature (23°C).

By comparison of the specimens in Figure 2.14 one can observe that at higher true strain rates barreling effects appear (Figure 2.14c). Based on simulations that will be presented later, this barreling can be ascribed to the inhomogeneous temperature evolution inside the specimen, causing the zones with higher temperatures to soften more. At lower true strain rates the heat has time to dissipate to the surroundings, yielding a homogeneously deformed specimen (Figure 2.14b).

3. Cold Drawing of a Dumbbell-Shaped Specimen

In many engineering thermoplastics under stretching, a substantial part of the plastic deformation occurs in an unstable way, more readily observed in amorphous polymers at a temperature close to or lower than the glass transition temperature T_g. This instability in the form of a neck and its propagation has been extensively studied in the literature, however, the experimental data that can be found are normally limited to some particular aspects of the global phenomena as mentioned by Marquez-Lucero, G'sell & Neale [61]. An overview on the tensile tests on polymers has been discussed in Chapter 1.3.

3.1. Experimental Setup

In the series of tensile experiments done in this work, a set of normative operations were devised and applied to record the intrinsic behavior of polycarbonate dumbbell-shaped specimens by monitoring its deformation process with two angled CCD cameras. Some special treatments had also to be applied to the specimen to increase the grey scale on the observed surface in order that the already-mentioned system ARAMIS could successfully post-process the recorded images. Adjustable illumination via LEDs (Light-Emitting Diode) was employed to uniformly lighten the specimen surface being observed. A frame-like structure was attached to the door of the environmental chamber together with a long beam carrying a sliding block which provided a sufficiently stable support and convenient positioning of the CCD cameras. The so-called calibration process, understood as the procedure through which the ARAMIS system measures the angle between the two cameras, was also standardized, enabling to perform the calibration outside the environmental chamber, considerably simplifying this otherwise tedious process.

3.1.1. Illumination of the Experiments. Two types of illumination have been considered to be used in 3–D experiments. The first, consisting of the use of the spot lights shown in Figure 3.1a, exhibited several disadvantages. Among the problems was the great amount of heat generated by the spotlights which greatly affected the temperature of the specimen, heating it up to a value away from the desired one. Also disadvantageous was the fact that the illumination provided by the round lamps was not uniformly distributed on the specimen surface, contrary to what calibration demands. Besides, the illuminators must be placed inside the environmental chamber due to the light reflection of the chamber's window if positioned outside, so this also raised the difficulty of the illumination source to be flexible and small enough to fit inside the chamber.

With regard to the above mentioned problems, another medium of illumination, the LED cold light illuminator, was tested inside the chamber. A group of 16 LEDs were connected in parallel to each other by a multi-functional wiring board which was further linked to a voltage-tunable power supply. The power supply is able to adjust the voltage applied to the LEDs and grants them the capability of continuous brightness regulation. Since the LED is a source of cold light, it did not affect the experiment. Due to the optical characteristics of the LED, it is also capable of providing relatively concentrated light and sufficient brightness by employing two sets of LEDs, see Figure 3.1b. The LED illumination finally turned out to be more effective and suitable for the current experimental configuration.

3.1.2. Arrangement of the Cameras. A constant distance between the cameras and the chamber's door is a crucial condition that must be fulfilled when carrying out

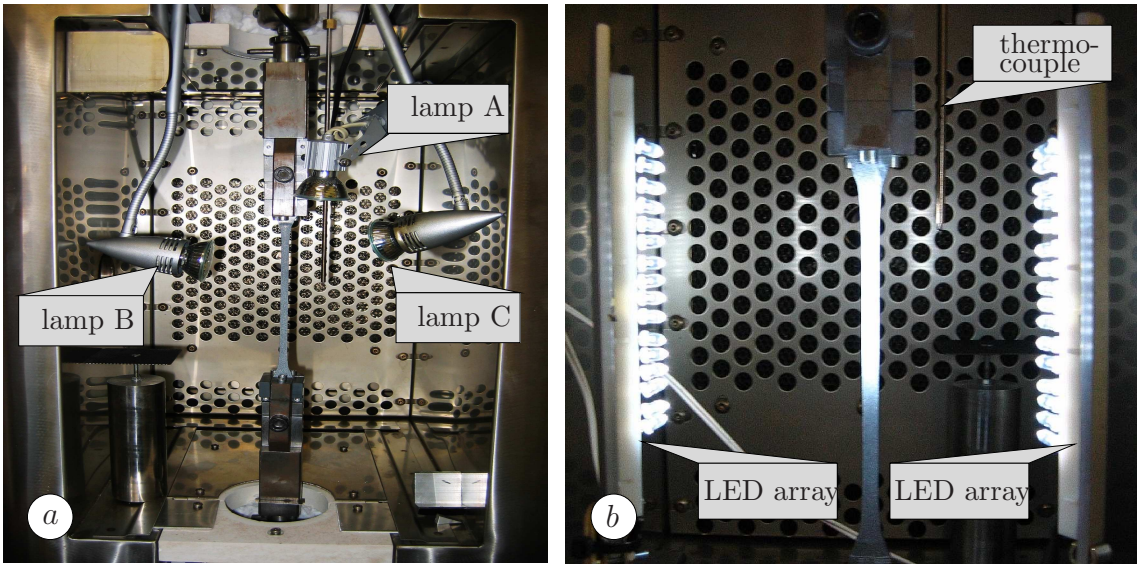

Figure 3.1: a) Illumination via three spot lamps. b) Illumination by use of two LED arrays.

3–D experiments since the glass of the chamber window acts as an extension of the camera lenses. This was enforced by mounting the CCD cameras onto the chamber's door by means of two devices constructed for this purpose; a carrier for the cameras to be supported on the chamber's door (Figure 3.2a) and a fine-adjusting mechanism to accurately modify the direction of each camera individually (Figure 3.2b). With the mentioned support mechanism, showed totally in Figure 1.8a, it was possible to move the cameras in five degrees of freedom, facilitating the alignment of these with respect to the object to be observed.

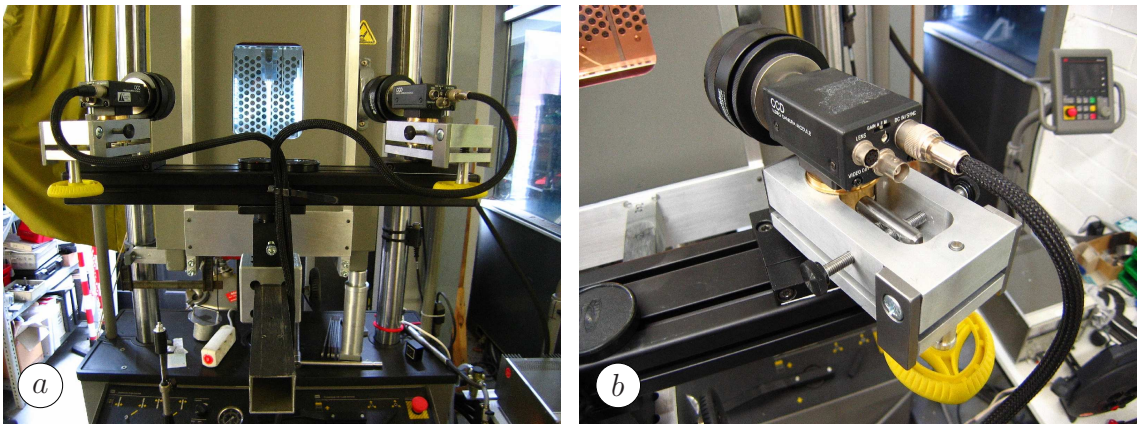

Figure 3.2: a) Arm holding the beam supporting the cameras. The whole construction is attached to the chamber door. b) Device produced to align the cameras individually

Camera Alignment. Measurements in the three dimensional space require the two cameras to meet at approximately the same point on the specimen's surface. The distance from the lense to the observed surface needs to be set in a way that the angle between the two cameras lies between 20° and 60° as suggested in GOM [40]. The width limitation of the observation window on the chamber's door should also be taken into consideration at

the same time. Thus, to compromise between the accuracy and the practical situation at hand, the angle between the cameras was set to approximately 34°. This angle, together with a distance from the cameras to the specimen of 540mm, yielded a maximum length of the recognized gauged section of the flat specimen of around 44 mm. Once the cameras are well aligned to the operational position with the chamber door closed, the aperture and the focus of the lenses needed to be adjusted in order to acquire adequate brightness and a sharp contour of the specimen in the camera view. In general, the aperture (f-number) should be as large as possible, i.e. the diaphragm should be closed as much as possible to obtain a better field depth.

3.1.3. System Calibration. Before taking measurements, the system has to be calibrated using a calibration object which is a square image printed with a specific pattern of white circular points covering an area of 35×28 mm^2 (see Figure 5.10). Although the variation of illumination in the images taken at specifically required positions can be automatically compensated for in ARAMIS, it is still recommended to supply adequate illumination for each position of the calibration object. The standard calibration procedure listed in GOM [40] was seriously and rigorously followed, nevertheless, for an exhaustive analysis of the execution of calibration the reader is referred to Qu [77], where this process as well as the possible problems encountered when carrying it out are extensively covered.

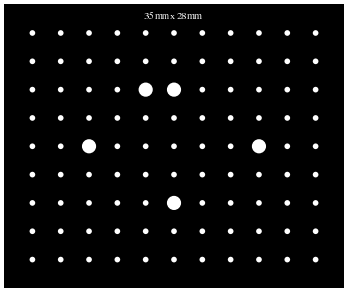

Figure 3.3: Calibration object having an area of 35×28 mm^2. Depending on the size of the object to be observed and the distance to the cameras, different sizes of calibration objects must be chosen.

Calibration Outside the Environmental Chamber. Thanks to the above detailed hardware used to attach the cameras to the chamber door it was possible to calibrate the ARAMIS system while keeping the door open as shown in Figure 1.8b. This considerably simplified the calibration process since throughout it the calibration object must be repeatedly moved, and this construction provides an ideal access to the calibration object. Important is to mention that the setup of the cameras must be done while looking at the object to be deformed (in this case the flat specimen). Once the cameras are directed to accurately capture the specimen and while keeping the chamber door open, the calibration object must be placed at approximately the same distance from the cameras as the specimen was. This procedure ensures that the object will be ideally placed in the focal point of the two cameras after calibration, assuring the best possible 3–D results. In the current experimental setup, the cameras, the environmental chamber and the calibration object are considered to form a closed system, therefore the proposed method considerably enhances the performance of the calibration.

3.1.4. Employed Tensile Specimens. As far as the specimen shape concerns, reference investigators such as Boyce & Arruda [17] or G'Sell et al. [43] have used cylindrical hour-glass shaped specimens instead of flat ones since the latter tend to *grow obliquely* as G'Sell et al. [43] described, leading to a complex combination of shear and extensional strains. Nevertheless, further problems by using the hour-glass specimen are also evident, e.g. both the stress and strain components vary along the loading direction and the radial axis, making the post processing complex. Another complication is brought forward by the optical measurement system due to the fact that it needs constant focus beforehand to get the best resolution for post-processing. Using specimens with circular cross-section will worsen the image post-processing since not the whole specimen surface that is viewable to both cameras can be correctly focused, making dumbbell-shaped flat specimens a more suitable choice. Some treatments applied to the test samples were required since the neck may appear at any position along the gauged section of the specimen. Also the measurement system demands an appropriate coating of the specimen surface to be observed in order to facilitate the surface recognition throughout the experiment. As mentioned before, there are basic requirements on the specimen preparation in order to maximize the size of the recognized 3–D surface. This essentially consists of an uniformly distributed pattern on the object surface intended to imprint contrast on it to unambiguously match each pixel in the recorded images from the left camera to the right one, see GOM [40]. Again, the reader is referred to Qu [77] for a detailed description of the coating process of a tensile specimen. The flat specimen needed to be slightly abraded to increase the surface roughness so that the coating sat better on the polycarbonate surface when applied.

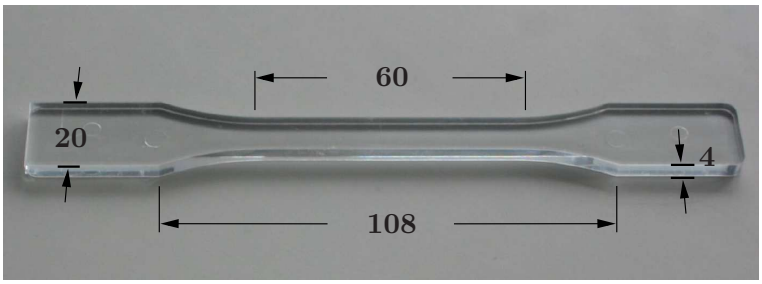

Figure 3.4: Geometry and dimensions of the dumbbell-shaped specimen used for tensile experiments. The dimensions are given in mm.

Furthermore, the specimen may neck at any point in the gauge section whereas it is desired for it to initialize within the scope of the cameras. Hence more abrasion was exerted at relatively the same position on each specimen where the onset of the neck was required to start. Additional experiments were conducted to investigate the structural effects of the spray coating and grinding on the polycarbonate specimens, which will be detailed in Chapter 3.4.

3.2. Standardized Experimental Procedure

Based on the preliminaries discussed in the previous chapters, a standard procedure was developed for both the execution of the tensile experiments and the post-processing of the obtained data.

3.2.1. Experimental Data Acquisition. The environmental chamber was turned on and the internal temperature was set to the desired value (23, 50 or 75°C) up to which the chamber was adiabatically heated for approximately 90 min. After coating the specimen it was swiftly aligned and secured in the tensile machine in order to bring the specimen, as fast as possible, to the desired temperature inside the chamber. This was to avoid idle times while being kept in open air since the sprayed coating began to dry and harden immediately, risking the appearance of cracks on the surface to be photographed by the ARAMIS system. Following that, the machine control was switched to force and applied 100 N as a pre-load for the specimen. This setup was then put to heat for another 30 min to homogenize the temperature inside the environmental chamber and the specimen. in Chapter 3.4 the influence of the duration of the additional heating time on the mechanical response of the tensile specimens was studied. As it can be seen in Figure 3.13c there is basically no difference between leaving the prepared specimen sitting inside the environmental chamber for 60 or 30 minutes, making it possible to start the experiment earlier without running the risk of drying the specimen coating, resulting in the already mentioned negative consequences, and at the same time ensuring that the desired temperature has been reached by the flat specimen. The latter can be asserted by the fact that polycarbonate, as many other glassy polymers, presents large sensitivity to temperature, yielding different load–displacement diagrams even when the temperature is only slightly changed from one experiment to another. Figure 3.13c clearly shows that this is not the case.

An important issue to be considered here is that the deformation of the specimen and the image acquisition of it must start at the same time. The version of ARAMIS (4.7.4-2) available at the *Material Testing Laboratory* of the Institute of Applied Mechanics (Civil Engineering) of the University of Stuttgart, where the experimental work was carried out, does not support an automatic synchronization between the start of the deformation by the testing machine and the beginning of the image acquisition by the ARAMIS system. This is not a trivial task since, as it will be shown in the subsequent chapters, synchronization is crucial to identify the position of the 3–D experimental results along the load-displacement diagram, which for the case presented here was done manually. ARAMIS acquired images at a rate of 30 frames/min for the first 140 sec while most of the elastic elongation of the specimen was surpassed and continued with a rate of 60 frames/min until the number of 860 images was reached in approximately 15 min and 28 sec, by which the neck almost propagated out of the scope of the cameras. However, the specimen was kept deforming to get a full range of the force and displacement data up to 100mm, being this value of displacement the maximum stroke allowed by the MTS machine. The entire tensile experiment lasted approximately 50 min and 19 sec for a deformation velocity of $\dot{u} = 2\text{mm/min}$.

3.2.2. Data Post–Processing. As mentioned before, the software and hardware used to obtain inhomogeneous three-dimensional experimental results presented additional challenges to the processes of data acquisition as well as to the post-processing of those data. It was due to those limitations that a compromise had to be made between the number of images and the post-processing parameters contained in the ARAMIS system to get as many images as possible with a reliable accuracy but being able to minimize the time required to solve the project, the latter meaning to correlate the images from the left camera with those from the right camera. At the end 860 steps (images) were captured in each experiment, being this an adequate number to observe in detail the neck

propagation throughout the monitored specimen surface, which required almost two days to be fully correlated. The calculation of the strain was also affected by the version of the system, which required the assistance of the GOM technical support who suggested time-consuming but effective counter measures. For more information on the acquisition of the 3–D strain distributions from inhomogeneous experiments see Qu [77].

3.3. Isothermal Results and Observations

In this Chapter the final results of the tensile experiments obtained from the MTS testing machine will be first presented. Then, means the integrated optical measurement system, the cold-drawing process will be further described. At last, the neck velocity and the natural draw ratio at loaded state are computed based on the information provided by ARAMIS. The employed deformation rate of 2mm/min was chosen based on the results reported in Maher, Haward & Hay [59] where a series of tensile experiments were conducted using an infrared camera to study the heat generated in the necking area during the drawing process of diverse glassy polymers. The experimental curve presented there in Figure 3a for polycarbonate shows that a drawing speed $\dot{u} = 2$ mm/min minimizes the *percentage of mechanical work converted to heat* α_m where the mentioned deformation rate, corresponding to a value of the so-called *reciprocal drawing speed* c_v^{-1} of $30.0 \cdot 10^3 \mathrm{m}^{-1}\mathrm{s}$, yields a value for α_m of less than 0.1%. Hence, the tension experiments presented in this chapter were conducted using the displacement rate of 2 mm/min at the temperatures 23, 50 and 75°C to ensure isothermal conditions by excluding the influence of heat accumulation when drawing the specimens, totally dissipating any heat generated to the surroundings, making temperature increments negligible.

3.3.1. Load-Displacement Diagram. Figure 3.5 depicts the load vs. displacement diagrams obtained from tensile experiments carried out at three different temperatures with the same loading rate of $\dot{u} = 2$ mm/min. The overall load-displacement curve for such a deformation state shows that homogeneous deformation occurs on the initial elongation of the specimen. The stiff elastic response is then followed by a nonlinear elastic-inelastic transition up to the yield point, corresponding to the initiation of the neck which thins the specimen to a smaller cross-sectional area at some point. The neck further localizes in a short time, brings a dramatic drop of force and stabilizes. Continuous extension is achieved by causing the neck to travel along the gauged section of the dumbbell-shape specimen, drawing more material into the necked region with a nearly constant load. It regains stiffness once the neck reaches the end of the gauged section and the strain hardening phenomenon with an increasing load takes place until the specimen is unloaded or finally fails. During the neck propagation, two regions develop at the same time and cover the entire length of the specimen, namely the un-necked and the necked zones. A transition area dividing these two regions is commonly termed as *transition front* (Hutchinson & Neale [51]) or *shoulder* (Marquez, G'sell & Neale [61]).

Temperature has three main influences on the overall mechanical behavior of polycarbonate under tension. *i*) It affects the yield point: an increment in temperature lowers the value of the maximum force at yield. *ii*) It shifts the yield point towards lower values of displacement when increased. *iii*) The amount of load drop lowers when the temperature is increased, reducing from approximately 607 N at 23°C to 436 N at 75°C.

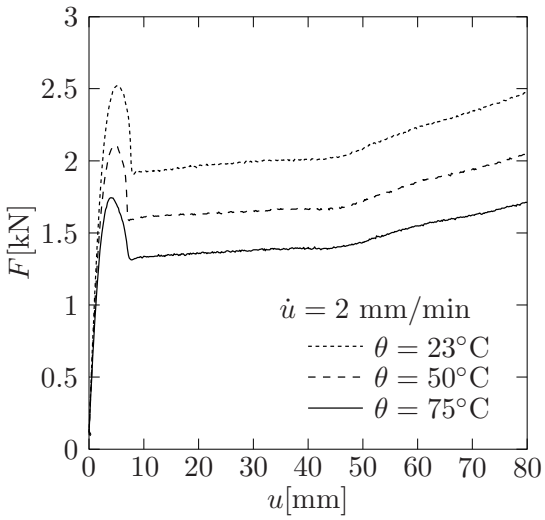

Figure 3.5: Load–displacement diagrams obtained under tension for the deformation rate $\dot{u} = 2$ mm/min and the temperatures 23, 50 and 75°C.

3.3.2. 3–D Experimental Results. In Figure 3.6 the full field distribution of the major strain on the recognized specimen surface and the corresponding live images from the optical measurement system are displayed together with the load vs. displacement diagram for 23°C. Based on the synchronization of the mentioned diagram with the 3-D inhomogeneous strain distributions, the deformation process can be described as follows: the flat specimen is homogeneously deformed up to approximately point *a*), after that a viscous transition up to the yield point in stage *b*) is observed, marking the beginning of the formation of the neck which starts to nucleate around stage *c*), getting finally stabilized at the end of the load drop at stage *d*). The neck then travels along the specimen clearly defining the necked and un-necked regions shown in stages *e*) and *f*), being the latter the last picture captured by ARAMIS.

To give an idea of the size of the identified images and to what portion of the specimen they correspond the boundary of the 3–D surface was projected onto the pictures taken by the left camera of the ARAMIS system. Note that for the 3–D strain distributions only the points appearing on the reference configuration (Figure 3.6a) are taken into account for the whole deformation of the observed object. No new points coming later into the scope of the cameras due to deformation will be considered by the system but points appearing in the reference configuration and leaving the scope of the cameras afterwards will be lost. This explains the fact that all the 3–D surfaces are smaller than the reference one. In Figure 3.7 a comparison of the propagation of the neck at three different temperatures is shown. It appears that the reference image at 50°C is wider than those at 23 and 75°C. This is independent of temperature and it is simply due to the fact that ARAMIS could recognize a wider three-dimensional surface when the experiment at 50°C was performed. Factors like illumination or specimen coating (spraying) can affect the size of the recognized surface.

As a preliminary observation on the effect of temperature on the nucleation, stabilization and propagation of the neck it is worth to mention that the main differences in the deformation state at the three temperatures displayed in Figure 3.7 are at the deformation stages *c* and *d*, i.e. where strain softening occurs. This minor discrepancies are expected to take place since after the yield point (stage *b*) the neck nucleation is a highly unstable

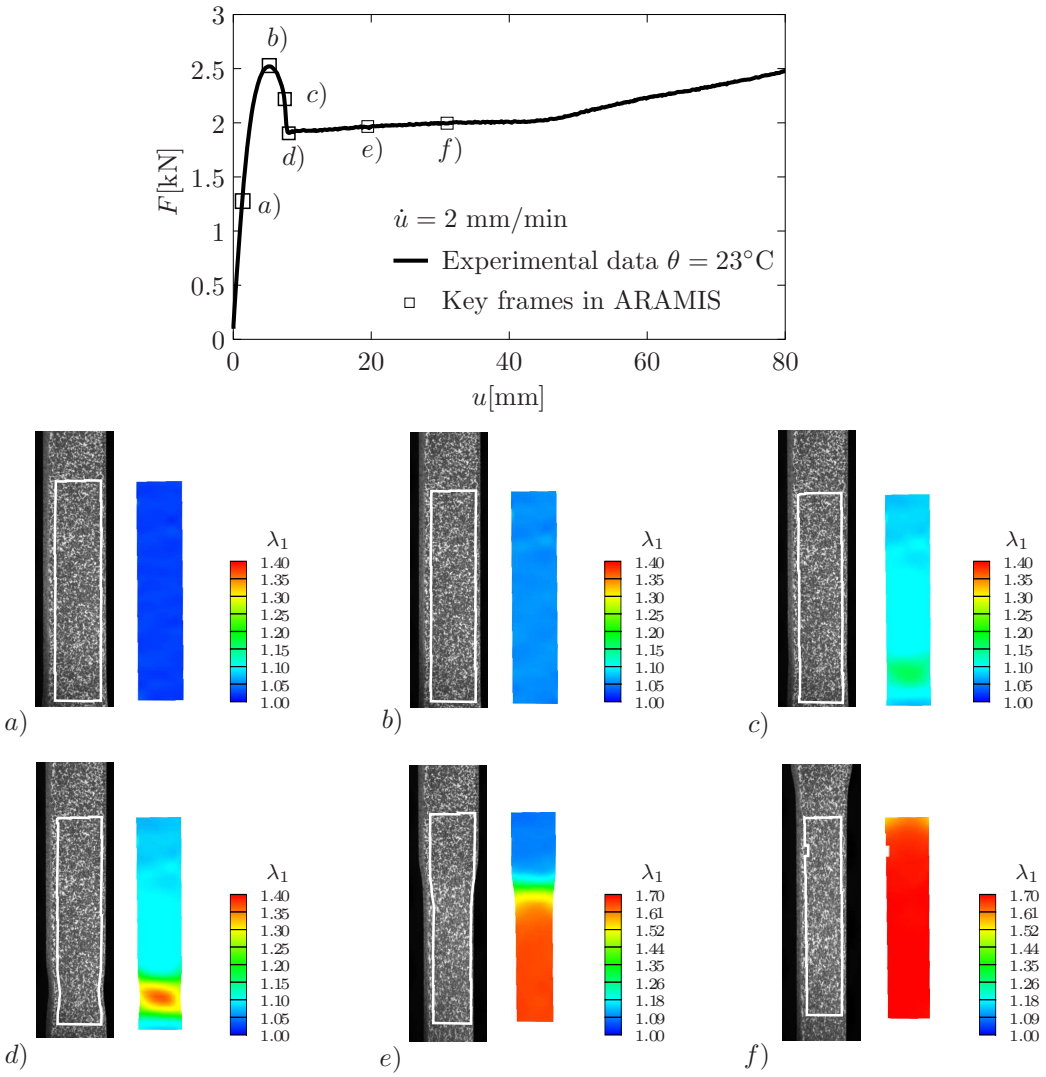

Figure 3.6: Illustration of six stages $a) - f)$ of the tensile deformation of PC at 23°C, the images on the left side are taken by the cameras and the post processed results on the right side show the corresponding distribution of the major strain on the recognized surface.

event that can easily be influenced by temperature or pressure. Besides these factors, it has been mentioned before that the experiments presented in this work are intended to serve as a reference for constitutive model validation, which applied to the inhomogeneous tensile experiments results in the demand that the neck nucleates at the same place along the specimen geometry in all tests, meaning that the specimens had to be treated in such a way that caused the neck to appear always at approximately the same position. For this purpose when the gauged section of the specimen was grinded for the application of the coating required by the grating method used in ARAMIS, the part where the neck was desired to start was longer grinded, assuring the appearance of the neck always at the lower part of the gauged section of the flat specimens. This process chiefly altered the deformation process at the stages c and d as shown in Figure 3.13b.

The calculated data of the inhomogeneous major strain distribution gives the possibility of computing the velocity of the neck propagation. From the result of the 3D optical measurement it was found that the necking zone is invariably accompanied by a dramatic change in major strain. Figure 3.8, showing the 3D strain distribution on the recognized

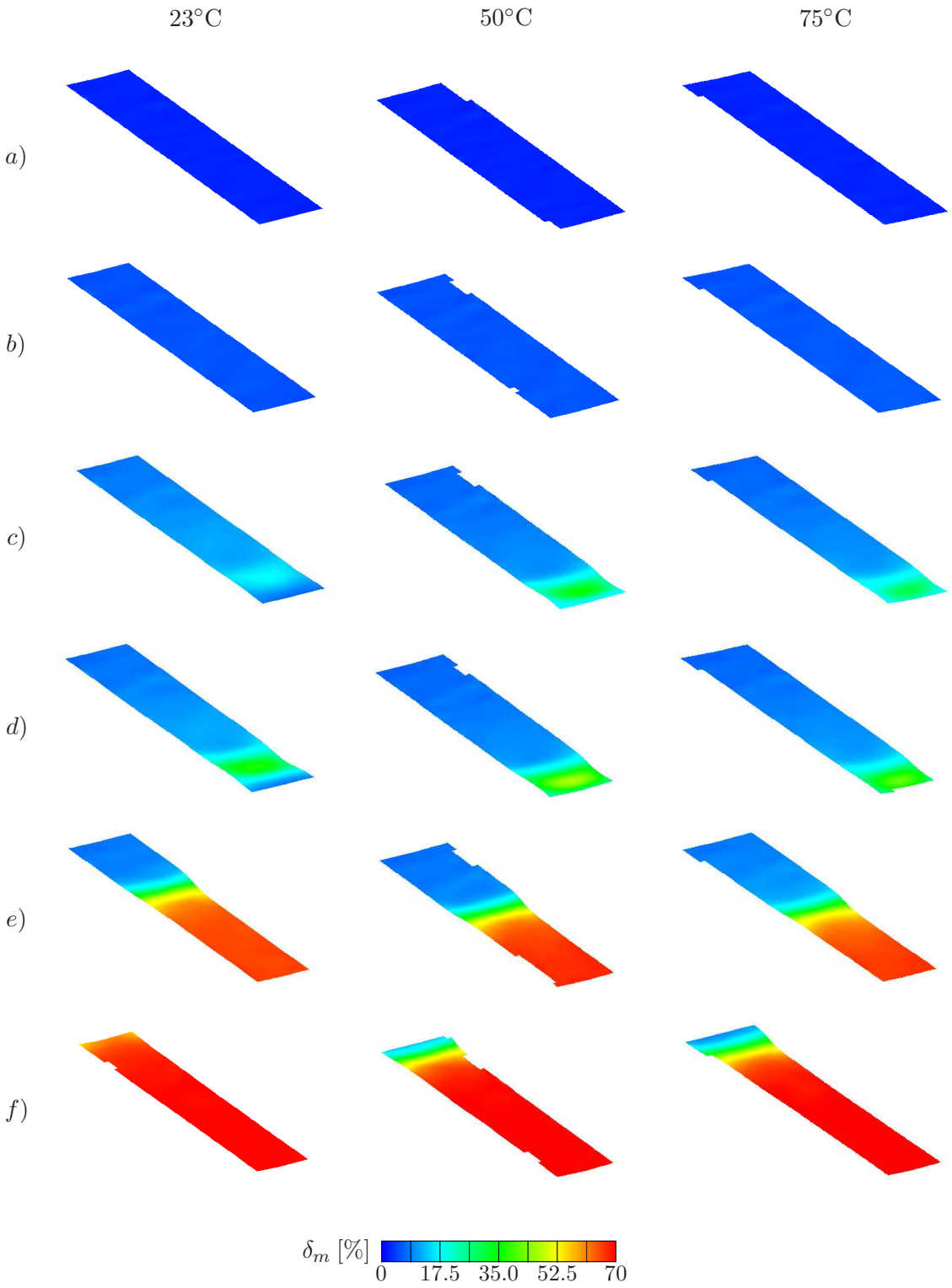

Figure 3.7: Major strain distributions obtained with the ARAMIS system at three different temperatures. The labels of the rows *a*)-*f*) at 23°C indicate the deformation stages labeled with the same letters in Figure 3.6.

specimen surfaces at different temperatures, demonstrates that 35% major strain (green) is an adequate value to trace the position of the neck shoulder with respect to time since the transition zone between necked and un-necked regions presents such an amount of the

major strain at all three temperatures. By tracking the 35% major strain in the recorded data it is possible to extract the location of those section points undergoing that strain and plot them against their corresponding time, the slope of which will represent the neck velocity at each temperature.

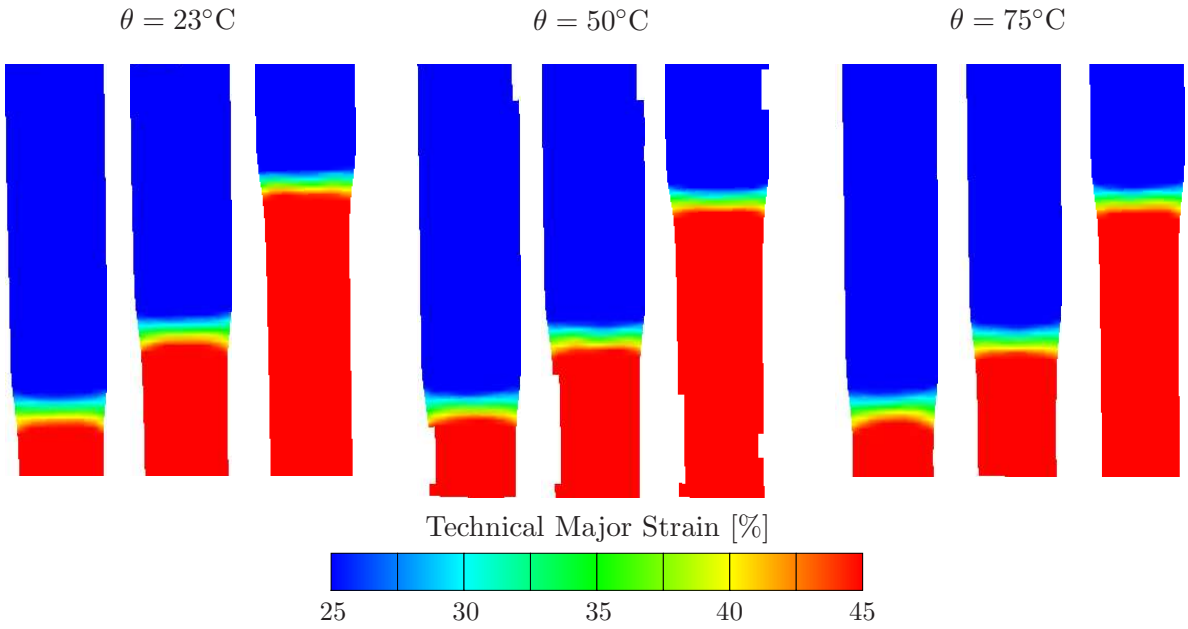

Figure 3.8: Major strain distributions at the stages of deformation 5, 7 and 11min under the temperatures 23. 50 and 75°C. The values of the technical major strain were narrowed to emphasize the amount observed at the transition zone (neck).

Having this confirmation at hand, the required information was extracted by firstly defining a straight line (termed as a *section* in ARAMIS) along the longitudinal mid-plane of the recognized specimen surface at the undeformed stage. Then this section was automatically discretized into points by the software, having a total section length of 44.3 mm. The local major strain distributions along the defined section are plotted in Figure 3.9 in a timely manner. From there, the position of the points reporting 35% major strain were recorded for further computation of the neck velocity. Note that despite all efforts to initiate the necking process at the same position for each tensile experiment the neck nucleated at slightly different points along the gauged section of the dumb-bell shaped specimens. This caused that in the plot shown in Figure 3.9a the curves corresponding to 50°C and 75°C were shifted towards the right to match that of 23°C, aligning the neck initiation areas to the same position for the ease of comparison. However, this alignment did not affect the interpretation of the material behavior. The analysis of the plots shown in Figure 3.9 will give more light into the necking process and how temperature affects it.

Pre-Yield Behavior. In Figure 3.9, the constant value of the major strain along the reference section length within the scope of the first 3 minutes of the duration of the experiment suggests that the test sample was undergoing a homogeneous elongation in the elastic range of deformation at all three temperatures. The overlap of the curves at 2 min in Figure 3.9a shows that the amount of the elastic deformation does not depend on temperature, at least for the applied deformation rate. This is confirmed by focusing on the location of the first section point on each two-minute curve at three temperatures

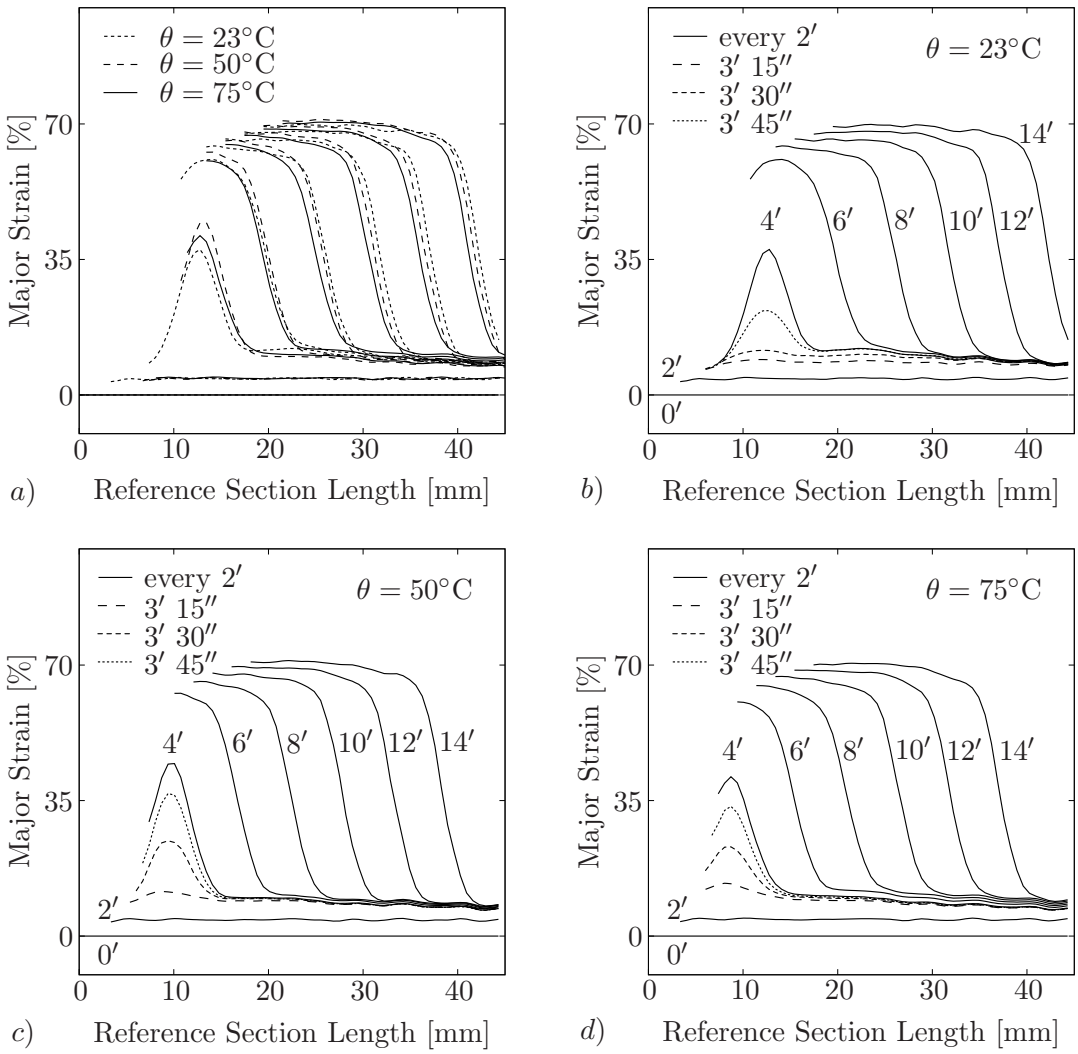

Figure 3.9: Major strains plotted against the reference section length of the specimen surface. a) Comparison of curves for all temperatures every 2 min. b) - d) Isothermally at temperatures $\theta = 23°C$, $\theta = 50°C$ and $\theta = 75°C$, respectively.

shown in Figure 3.9b, c and d which was found to have moved 3.35 mm along the loading direction, regardless of temperature. Taking a closer look to the curves at 2 min, the plots show an average major strain of $4.2\% \sim 4.3\%$ across the monitored section length. Since the extension of the specimens is believed to be uniform till at least 2 min, a simple calculation revealed that the elongation of the gauged section after 2 min lied between 2.5 mm and 2.6 mm for an initial length of the gauged section of 60 mm (see Figure 3.4). Additionally, if the loading speed of the testing machine (2 mm/min) is considered, the total displacement of the loading cylinder was 4 mm at the mentioned time. It is noticeable that thanks to the results obtained from the inhomogeneous experiments it is possible to ascertain that more than 35% of the elastic deformation was consumed between the end of the gauged section and the point where the specimen is fixed to the grips of the machine.

Yield and post-yield behavior. The maximum load was applied to the specimen approximately after 2 min 37 sec for the experiment at 23°C, 2 min 18 sec at 50°C and 2 min 10 sec at 75°C. This corroborated what was observed in the load–displacement

diagrams of Figure 3.5 where the yield point shifted to lower values of deformation with increasing temperature, implying a shorter time for the occurrence of the yield phenomenon at higher temperatures. Even at the point of maximum load, for each temperature individually, the major strain along the monitored specimen surface was still homogeneous. Immediately after this maximum an increase of the strain localization at the point where the neck began was observed, coinciding with a dramatic load drop.

After approximately 4 min for all temperatures, when the neck stabilized at the end of the load drop and began to propagate, there was not much influence of temperature found on the deformation of the specimen in both the necked and un-necked regions (compare the magnitude of the major strain at different temperatures for each specific time in Figure 3.9a). However, at each fixed temperature, the major strain increased continuously in the necked zone with the ongoing neck propagation whereas in the un-necked region at the same time, it showed a certain time dependency only at high temperatures. As an example of the latter, in Figure 3.9d (75°C) the un-necked region after 40mm of the reference section length shows a higher variation in major strain than Figure 3.9c (50°C) after the same point. This is explained by the softening suffered by the whole test piece due to the higher temperature.

Another data series exported from the ARAMIS projects is shown in Figure 3.10. It depicts the relative displacements of all the observable section points with respect to their original reference positions on the time evolution at three temperatures. A comparison of Figure 3.10b, c and d is shown in Figure 3.10a by aligning the neck initiation areas to the same position. Identically as previously found, till the onset of a neck, the specimen was deforming uniformly, resulting in straight lines in the diagram across the whole monitored section. Once the neck initiated and stabilized the curve rose up and bended in the necking area originating a new linear segment in the diagram. The slope of the curves in both the necked and un-necked regions increased very slowly with further straining, implying a steady deforming state in those regions.

3.3.3. Neck Velocity. The concept of the *neck velocity* has no clear definition and is rarely used in the literature simply because the neck always travels with a continuous elongation of the specimen, making the point to be taken as origin hard to define, what could lead to an ambiguous measurement of the displacement of the neck. Conveniently in this work, the position of the neck becomes relevant once the neck begins to propagate along the gauged section of the flat specimen. Then, the interpretation of the *neck velocity* can be taken as absolute since the reference point, located at the upper edge of the recognized surface, becomes steady and does not move after the onset of the neck. By organizing and processing the correlated data displayed in Figure 3.9 and 3.10 the neck position-time diagram in Figure 3.11 was obtained, from which the velocity can be derived from the slopes of the presented curves. The mean value of the *neck velocity* is computed to be $\bar{\dot{u}}_n \simeq 3.0$ mm/min in this experiment series. It can be concluded that once the neck stabilizes, it travels along the gauged section of the specimen at the same and nearly constant speed within the range of temperatures used. In other words, the neck velocity does not seem to be affected by temperature under the employed deformation rate. This finding can also be qualitatively observed in Figure 3.8 since all the stages of deformation displayed there correspond to the same time, and therefore same displacement of the actuating cylinder, and the neck appears always at the same position for all 3 cases.

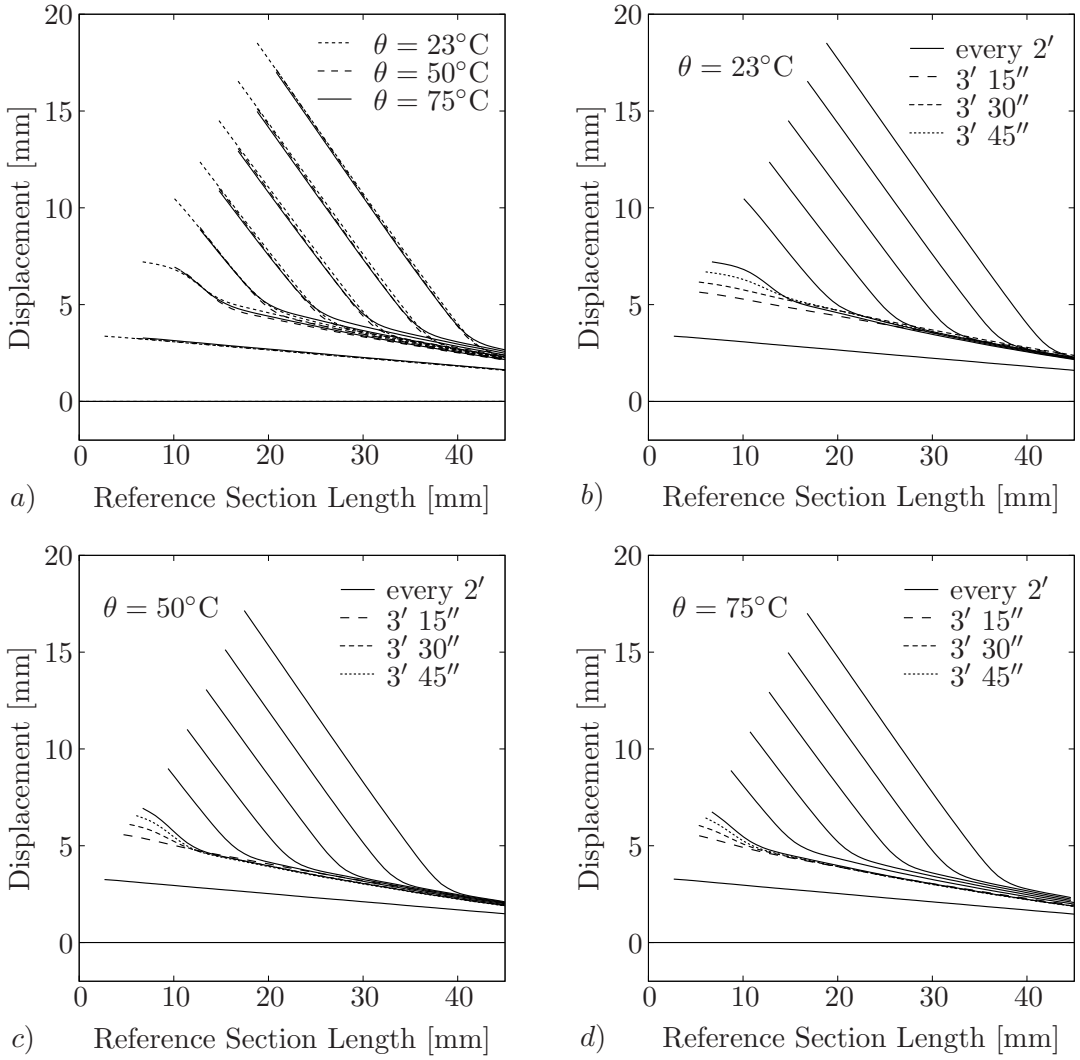

Figure 3.10: Point displacements plotted against reference section length of the specimen surface. a) Comparison of curves for all temperatures every 2 min. b) - d) Isothermally at temperatures $\theta = 23°C$, $\theta = 50°C$ and $\theta = 75°C$, respectively.

3.3.4. Natural Draw Ratio. The natural draw ratio λ_n is an important mechanical quantity serving to present the extensibility or ductility of the material. As defined by Allison & Ward [6], it is the ratio of the cross-sectional area before and after drawing. If we assume that the volume change during the cold-drawing is negligible, the natural draw ratio can be further determined by the variation of the distance between two benchmark lines (or points in our case) on the specimen surface from its undeformed state to the necked state. Zhou & Chudnovsky [93] performed tensile experiments on dumbbell-shaped specimens of polycarbonate at an initial strain rate of 3×10^{-4} s^{-1} in a wide temperature range. They reported a weak temperature dependence of the natural draw ratio, a slight increase from 1.65 at 23°C to 1.72 at 115°C was observed. Based on the data behind Figure 3.10, we derived the natural draw ratio using two Chapter points spaced approximately 2 mm from each other in the necked region. The distance variation in between the points was recorded every minute after the neck began to propagate steadily and the natural draw ratio was finally plotted in Figure 3.12 against different temperatures. Therein, we find no major influence of temperature on the natural draw ratio and it is observed to be relatively constant at the temperature range we

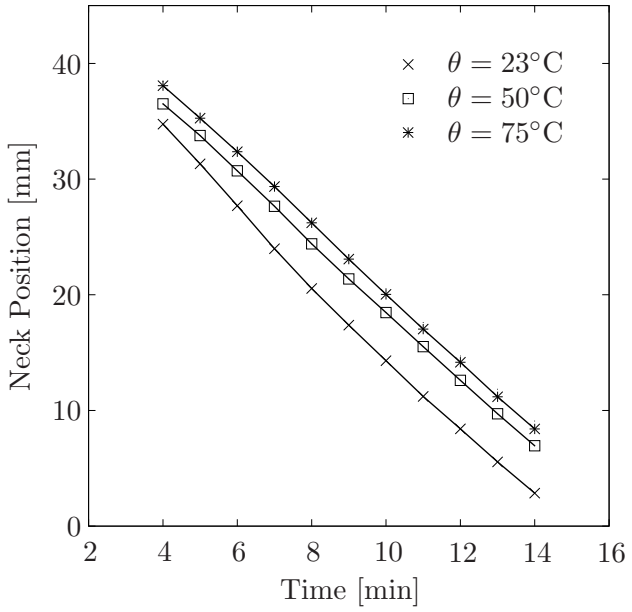

Figure 3.11: Velocities of the neck propagation at different temperatures. The neck velocity is first considered after 4 minutes since at this time the neck stabilizes and begins to propagate along the gauged section of the flat specimens.

applied. The distinction comparing to Allison & Ward's observation is ascribed to the difference in measurement. The earlier results were based on measurements of the unloaded specimen after deformation while our optical measurement technique allows real-time monitoring under ongoing straining. If we take the unloading process into consideration, at a higher temperature, more irreversible deformation is stored in the unloaded specimen, resulting in a slightly less spring back of the material than that at lower temperatures. It is the higher recoverable strain at a higher temperature that causes the natural draw ratio to rise after unloading. To prove this, we then measured the width and thickness of our deformed but unloaded specimens and the natural draw ratios were calculated from the ratios of the cross-sectional areas, the same method as Allison & Ward utilized. The results were also plotted together in Figure 3.12 and the expected temperature dependence is revealed. Note that, the transversal area of the gauged section along the drawn specimen is not uniform, typically the minimum area exhibits in the position of neck initialization and becomes continuously increased towards the gripping region. Thus the natural draw ratios of the unloaded specimens presented in Figure 3.12 are comprised of a maximum and a minimum for each temperature. The magnitude difference of this quantity between the unloaded and loaded specimens is due to the fact that the optical measurement ceased to capture the images before the strain hardening which further decreased the cross-Chapteral area of the specimen, leading to a higher value of the natural draw ratio.

3.4. Repeatability

In order to observe the repeatability of the tensile experimental results, three or more additional experiments were carried out at each temperature. The results are displayed in Figure 3.13a where it can be seen that besides the end of the strain softening region, which is highly sensitive to the treatment for localizing the neck, the overall responses at each test condition consist with the presented experimental results in Chapter 3.3.1.

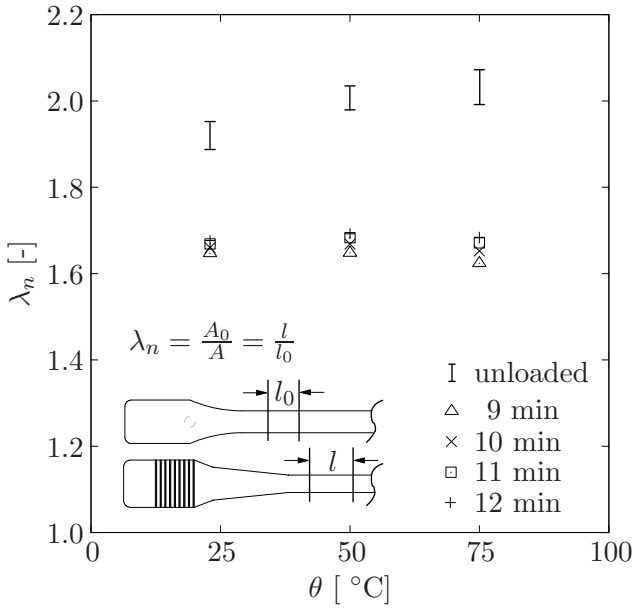

Figure 3.12: Natural draw ratio λ_n at different loading stages and temperatures.

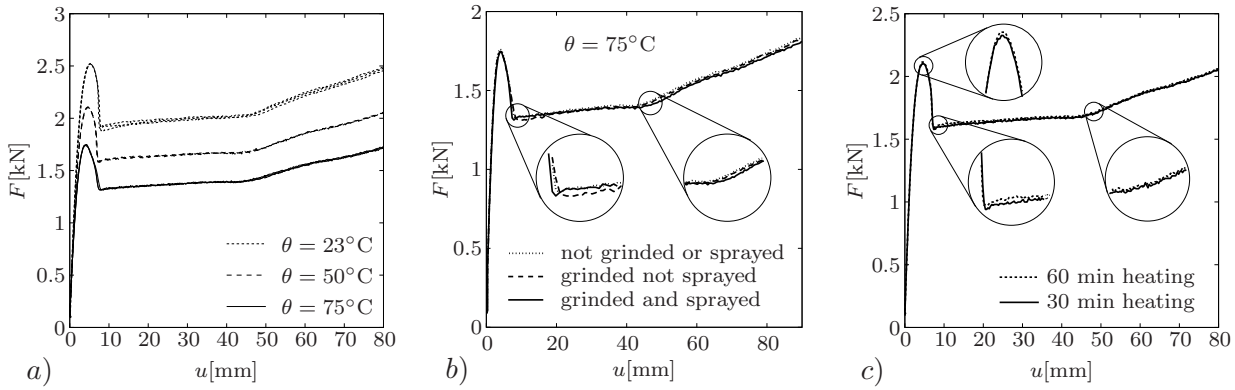

Figure 3.13: *a*) Test repeatability under different temperatures. *b*) Comparison between the mechanical behavior using different specimen surface treatments at 75°C. *c*) Comparison bewtween influences of heating time before tests under 50°C start.

When utilizing ARAMIS, grinding and spraying on the specimen surface are the mandatory and standard treatment in the optical measurement. However, a comparison was done by performing two additional experiments to decouple and reveal the effects of grinding and spray coating: one with a virgin specimen which was left untreated and the other with a ground surface but not sprayed. Figure 3.13b shows the results at the same temperature (50°C), from which we observe almost no determinative differences in the mechanical response by use of those surface treatments.

Note that this series of tensile experiments were implemented and followed exactly as what was stated in Chapter 3.2. One additional experiment was carried out at 50°C to examine whether 30 min heating time of the specimen together with the already heated chamber is sufficient to bring the temperature of the specimen to the same level. Therefore, the heating time was extended to 60 min and the final results were compared in Figure 3.13c. Nevertheless, no difference is found in the mechanical response of the material, implying that 30 min heating time as we used in the standard procedure is sufficient for the specimen to achieve the desired temperature.

4. Thermo–Elasto–Visco Plasticity of Glassy Polymers

Almost all of the works on glassy polymers describe the local viscoplastic deformation by a *plastic map theory* in connection with the *multiplicative decomposition* of the deformation gradient as considered from different perspectives in KRÖNER [55], LEE [56] and MANDEL [60]. This is accompanied by a particular assumption with regard to the plastic rotation, such as proposed by BOYCE, PARKS & ARGON [21] or ANAND & GURTIN [7]. In contrast, so–called *plastic metric theories* proposed in MIEHE [68, 69, 67] avoid a priori a plastic rotation and substantially simplify the geometric setting. These approaches are to in the author's opinion very well suited for a purely phenomenological models of finite plasticity. The formulations MIEHE & KECK [74] and MIEHE, GÖKTEPE & MÉNDEZ [73] of finite inelasticity for rubbery and glassy polymers under isothermal conditions demonstrate successful applications of this framework. The latter work applies an *additive decomposition* of Lagrangian logarithmic strains as proposed in MIEHE, APEL & LAMBRECHT [71] and MIEHE & APEL [70]. The analogy of the constitutive setting within the logarithmic strain space and the geometrically linear theory of plasticity makes this approach extremely transparent and attractive with regard to its numerical formulation. The goal of this work is to apply such a formulation to non–isothermal inelasticity of glassy polymers.

We discuss aspects of the numerical implementation of coupled thermo-elasto-visco plasticity of glassy polymers in the logarithmic strain space. We start with a summary of the relevant tensors of finite strain plasticity and proceed with the construction of a general constitutive framework of thermoviscoplasticity where the relevant constitutive equations entering the formulation are defined. Two constitutive models for thermoviscoplastic flow are presented and their main internal variables are defined. Afterwards, the global algorithms for the solution of the coupled thermomechanical problem governed by the balance of linear momentum and energy are given. Finally, we make some remarks concerning the linearization of the global algorithms and the finite element implementation.

4.1. Basic Tensorial Objects of Plastic Metric Thermoplasticity

Deformation and Temperature Gradients. Let $\mathcal{B} \subset \mathcal{R}^3$ be the reference configuration of the body of interest and $\boldsymbol{\varphi}(\boldsymbol{X}, t)$ the nonlinear *deformation map* at time of the solid $t \in \mathcal{R}_+$. $\boldsymbol{\varphi}_t$ maps points $\boldsymbol{X} \in \mathcal{B}$ of the reference configuration $\mathcal{B}$ onto points $\boldsymbol{x} = \boldsymbol{\varphi}_t(\boldsymbol{X}) \in \boldsymbol{\varphi}_t(\mathcal{B})$ of the current configuration. The material deformation gradient

$$\boldsymbol{F} := \nabla_X \boldsymbol{\varphi}(\boldsymbol{X}, t) \quad \text{with} \quad J := \det[\boldsymbol{F}] > 0 \tag{4.1}$$

maps tangent vectors of material curves onto tangent vectors of the deformed material curves. Consider the *temperature field* $\theta(\boldsymbol{x}, t)$ defined on the reference configuration $\mathcal{B} \subset \mathcal{R}^3$ of the solid. We denote

$$\boldsymbol{T} := \nabla_X \theta(\boldsymbol{X}, t) \tag{4.2}$$

as the material temperature gradient.

Current and Reference Metric. Let furthermore $\boldsymbol{g}$ and $\boldsymbol{G}$ denote the standard covariant metric tensors on the current configuration and the reference configuration, respectively. By application of Cartesian coordinates we have the index representations

$g_{ab} = \delta_{ab}$ and $G_{AB} = \delta_{AB}$ in terms of the Kronecker symbol. We denote the tensors

$$\boldsymbol{C} := \boldsymbol{F}^T \boldsymbol{g} \boldsymbol{F} \qquad \text{and} \qquad \boldsymbol{c} := \boldsymbol{F}^{-T} \boldsymbol{G} \boldsymbol{F}^{-1} \tag{4.3}$$

on the reference configuration and the current configuration as *convected current metric* and as *convected reference metric*, respectively. The associated index representations are $C_{AB} = g_{ab} F^a{}_A F^b{}_B$ and $c_{ab} = G_{AB} (F^{-1})^A{}_a (F^{-1})^B{}_b$.

Plastic Metric. The history dependence of the inelastic stress response can be described by taking into account so–called internal variables in addition to the primary deformation variables. The evolution of these internal variables is then determined by additional constitutive functions. Let $\boldsymbol{G}^p$ with initial condition $\boldsymbol{G}^p(t = t_0) = \boldsymbol{G}$ denote the covariant Lagrangian *plastic metric*. Then its Eulerian counterpart

$$\boldsymbol{c}^p := \boldsymbol{F}^{-T} \boldsymbol{G}^p \boldsymbol{F}^{-1} \tag{4.4}$$

is obtained by a composition $(c^p)_{ab} = (G^p)_{AB} (F^{-1})^A{}_a (F^{-1})^B{}_b$ with the linear tangent map $\boldsymbol{F}$. The evolution of $\boldsymbol{G}^p$ and $\boldsymbol{c}^p$ is governed by a plastic flow rule.

Logarithmic Elastic Strains. A particular dependence of a Lagrangean elastic strain variable on current and the plastic metric $\boldsymbol{C}$ and $\boldsymbol{G}^p$ is provided by the *additive decomposition*

$$\boldsymbol{\varepsilon}^e := \boldsymbol{\varepsilon} - \boldsymbol{\varepsilon}^p \tag{4.5}$$

in the logarithmic strain space as suggested in Miehe & Lambrecht [75]. Here,

$$\boldsymbol{\varepsilon} := \frac{1}{2} \ln \boldsymbol{C} \qquad \text{and} \qquad \boldsymbol{\varepsilon}^p := \frac{1}{2} \ln \boldsymbol{G}^p \tag{4.6}$$

are the Hencky–type total and plastic strains, respectively. Due to the one–to–one relationship between $\boldsymbol{\varepsilon}^p$ and $\boldsymbol{G}^p$, we consider in what follow the logarithmic plastic strain $\boldsymbol{\varepsilon}^p$ as the internal variable which describes the local plastic deformation. For the subsequent outline of a thermodynamic framework, the representation of the rate of total logarithmic strain is of particular importance. To this end, we introduce the relationships

$$\dot{\boldsymbol{\varepsilon}} = \mathbb{Q} : \dot{\boldsymbol{F}} \quad \text{and} \quad \dot{\mathbb{Q}} = \mathbb{L} : \dot{\boldsymbol{F}} \tag{4.7}$$

in terms of the fourth and sixth order nominal transformation tensors defined by

$$\mathbb{Q} := \partial_{\boldsymbol{F}} \boldsymbol{\varepsilon} \quad \text{and} \quad \mathbb{L} := \partial^2_{\boldsymbol{F}\boldsymbol{F}} \boldsymbol{\varepsilon} \,, \tag{4.8}$$

respectively. These transformation tensors play a central role in the subsequent treatment. For the explicit forms of the transformation tensors of the stresses and tangent in the logarithmic strain space to their nominal, Lagrangian or Eulerian counterparts we refer to Miehe & Lambrecht [75].

Stress Tensors and Heat Flux Vectors. Let $\boldsymbol{\sigma}$ denote the contravariant Eulerian (true) Cauchy stress tensor and $\boldsymbol{\tau} := J\boldsymbol{\sigma}$ the Kirchhoff stress. Then

$$\boldsymbol{P} := \boldsymbol{\tau} \boldsymbol{F}^{-T} \qquad \text{and} \qquad \boldsymbol{S} := \boldsymbol{F}^{-1} \boldsymbol{\tau} \boldsymbol{F}^{-T} \tag{4.9}$$

are the first Piola *nominal stress tensor* and the Lagrangian symmetric Piola stress tensor, respectively, having the index notation $P^{aB} = \tau^{ab} (F^{-1})^B{}_b$ and $S^{AB} = \tau^{ab} (F^{-1})^A{}_a (F^{-1})^B{}_b$. Furthermore, let $\boldsymbol{q}$ denote the contravariant Eulerian (true) heat flux vector and $\boldsymbol{h} := J\boldsymbol{q}$ the Kirchhoff–type heat flux. Then

$$\boldsymbol{Q} := \boldsymbol{h} \boldsymbol{F}^{-T} \tag{4.10}$$

is the Lagrangian heat flux vector, having the index notation $Q^A = h^a (F^{-1})^A{}_a$.

4.2. General Constitutive Framework of Thermoviscoplasticity

The state of the material at a local material point is assumed to be described by the total Hencky strain $\boldsymbol{\varepsilon}$, the plastic strain $\boldsymbol{\varepsilon}^p$ that have been introduced in (4.6) and the absolute temperature θ. The thermomechanical potential, the Helmholtz *free energy*, is then formulated in terms of the state variables

$$\boxed{\Psi = \hat{\Psi}(\boldsymbol{\varepsilon}, \boldsymbol{\varepsilon}^p, \theta)} \tag{4.11}$$

per unit reference volume. With this functional dependency at hand, we get the intrinsic (local) *dissipation* from the Clausius-Planck inequality

$$\mathcal{D}_{loc} := \boldsymbol{P} : \dot{\boldsymbol{F}} - \dot{\Psi} - H\dot{\theta} \;\geq\; 0 \,, \tag{4.12}$$

defined per unit reference volume. Here, $\boldsymbol{P}$ is the *nominal stress* tensor introduced in (4.9) and H the *entropy* per unit of the reference volume. Incorporation of the time derivative of the free energy gives the expression

$$\mathcal{D}_{loc} = (\boldsymbol{P} - \partial_{\boldsymbol{\varepsilon}}\hat{\Psi} : \mathbb{Q}) : \dot{\boldsymbol{F}} - (H + \partial_\theta \hat{\Psi})\,\dot{\theta} - \partial_{\boldsymbol{\varepsilon}^p}\hat{\Psi} : \dot{\boldsymbol{\varepsilon}}^p \;\geq\; 0 \;. \tag{4.13}$$

The constitutive expressions for the nominal stress tensor $\boldsymbol{P}$ and the entropy H are then determined by the free energy. Following a standard argument, we obtain

$$\boldsymbol{P} = \partial_{\boldsymbol{\varepsilon}}\hat{\Psi}(\boldsymbol{\varepsilon}, \boldsymbol{\varepsilon}^p, \theta) : \mathbb{Q} \qquad \text{and} \qquad H = -\partial_\theta \hat{\Psi}(\boldsymbol{\varepsilon}, \boldsymbol{\varepsilon}^p, \theta) \,. \tag{4.14}$$

Note that the nominal stresses can be written in the form $\boldsymbol{P} = \boldsymbol{\pi} : \mathbb{Q}$. They are determined by the stresses $\boldsymbol{\pi} := \partial_{\boldsymbol{\varepsilon}}\hat{\Psi}(\boldsymbol{\varepsilon}, \boldsymbol{\varepsilon}^p, \theta)$ in the logarithmic space dual to $\boldsymbol{\varepsilon}$, but mapped by the transformation tensor $\mathbb{Q}$ defined in (4.8). This is a direct consequence of the constitutive formulation in the logarithmic strain space. These assumptions reduce the Clausius-Planck inequality (4.13) to the form

$$\mathcal{D}_{loc} = \boldsymbol{\sigma}^p : \dot{\boldsymbol{\varepsilon}}^p \;\geq\; 0 \qquad \text{with} \qquad \boldsymbol{\sigma}^p := -\partial_{\boldsymbol{\varepsilon}^p}\hat{\Psi}(\boldsymbol{\varepsilon}, \boldsymbol{\varepsilon}^p, \theta) \,, \tag{4.15}$$

where we introduced per definition the thermodynamic driving stress tensor $\boldsymbol{\sigma}^p$ conjugate to the plastic strains $\boldsymbol{\varepsilon}^p$ in the logarithmic strain space. In order to complete the local overall constitutive framework we need to define the evolution equation for the plastic strains $\boldsymbol{\varepsilon}^p$. To this end, we consider an isotropic, isochoric viscoplastic flow in the direction of the thermodynamic driving force. This gives the structure

$$\dot{\boldsymbol{\varepsilon}}^p = \dot{\gamma}^p \frac{\operatorname{dev}[\boldsymbol{\sigma}^p]}{|\operatorname{dev}[\boldsymbol{\sigma}^p]|} \,, \tag{4.16}$$

in terms of the amount $\dot{\gamma}^p$ of viscoplastic flow, which has to be specified by a separate constitutive equation. Here, $\operatorname{dev}[\boldsymbol{\sigma}^p] := \boldsymbol{\sigma}^p - \frac{1}{3}\operatorname{tr}[\boldsymbol{\sigma}^p]\,\mathbf{1}$ with $\operatorname{tr}[\cdot] := (\cdot){:}\mathbf{1}$ denotes the deviator of the driving force. Note that for the initial value of the plastic strain tensor $\boldsymbol{\varepsilon}^p(\boldsymbol{X}, t_0) = \mathbf{0}$, the plastic deformation remains volume conserving, i.e.

$$\operatorname{tr}[\boldsymbol{\varepsilon}^p] = 0 \quad \Rightarrow \quad \det[\boldsymbol{G}^p] = 1 \,. \tag{4.17}$$

This is in accordance with the finite viscoplastic behavior of ductile glassy polymers that undergo plastic deformations chiefly by *shear yielding* without exhibiting dilative plastic

flow, such as *crazing*. Inserting (4.16) into (4.15), the restriction dictated by the second law of thermodynamics finally reads

$$\mathcal{D}_{loc} = \mid \mathrm{dev}[\boldsymbol{\sigma}^p] \mid \dot{\gamma}^p \geq 0 \ . \tag{4.18}$$

As a consequence, the model is said to be thermodynamically consistent for a *positive amount of viscoplastic flow* $\dot{\gamma}^p \geq 0$. For the thermomechanical modeling of isotropic glassy polymers under consideration, the formulation of the plastic strain rate is a critical point of the constitutive modeling and discussed in the subsequent setting. We assume a general dependence

$$\boxed{\dot{\gamma}^p = \hat{f}^p(\mathrm{dev}[\boldsymbol{\sigma}^p], \theta) \geq 0} \tag{4.19}$$

on the driving force $\boldsymbol{\sigma}^p$ and the temperature θ. The Specific functions $\hat{\Psi}$ and $\hat{f}^p$ for the stored free energy and the amount of viscoplastic flow are outlined in Chapter 4.4. The constitutive equations of coupled thermoplasticity are completed by a constitutive assumption with regard to the heat flux. In this treatment, the flux in the interior of the body is assumed to be governed by an isotropic Eulerian Fourier–type law for the Kirchhoff heat flux $\boldsymbol{h}$. This gives the constitutive formulation

$$\boldsymbol{Q} = -k\, \boldsymbol{C}^{-1}\boldsymbol{T} \tag{4.20}$$

for the Lagrangian heat flux defined in (4.20) in terms of the material temperature gradient $\boldsymbol{T}$ defined in (4.2). This ansatz provides a positive dissipation

$$\mathcal{D}_{con} := -\frac{1}{\theta}\boldsymbol{Q} \cdot \boldsymbol{T} \geq 0 \tag{4.21}$$

for positive heat conductivity parameter $k > 0$. Note the coupling of the heat flux with the deformation, governed by its dependence on the current metric $\boldsymbol{C}$ defined in (4.3), which is a positive definite tensor.

4.3. The Global Equations of Coupled Thermoviscoplasticity

We now embed the above outlined general constitutive functions into the global balance equations, which govern the initial boundary value problem of coupled thermoplasticity at finite strains. The first set of equations cover the balances of linear and angular momentum

$$\rho_0 \dot{\boldsymbol{v}} = \mathrm{Div}[\boldsymbol{P}] + \boldsymbol{\gamma} \quad \text{and} \quad \boldsymbol{F}\boldsymbol{P}^T = \boldsymbol{P}\boldsymbol{F}^T \ . \tag{4.22}$$

Here, $\boldsymbol{v} := \partial_t \boldsymbol{\varphi}_t$ is the material velocity field, ρ_0 the density of the reference configuration and $\boldsymbol{\gamma}$ a prescribed body–force field. $\boldsymbol{P}$ is the nominal stress field introduced in (4.9) and Div[•] the divergence operator with respect to the Lagrangian coordinates $\boldsymbol{X}$. The second essential global equation is the balance of internal energy

$$\rho_0 \dot{E} = \boldsymbol{P} : \dot{\boldsymbol{F}} + \mathrm{Div}[-\boldsymbol{Q}] + \mathcal{R} \ . \tag{4.23}$$

E is the internal energy density with respect to the volume of the reference configuration. $\boldsymbol{Q}$ denotes the Lagrangian heat-flux vector introduced in (4.20) and R a prescribed heat source with respect to the unit of the reference volume. $\boldsymbol{P} : \dot{\boldsymbol{F}}$ is the stress power with respect to the unit of the reference volume. Based on the Legendre transformation

$E = \Psi + \theta H$, we obtain by insertion of the constitutive equations (4.14) and (4.15) the evolution $\dot{E} = \boldsymbol{P} : \dot{\boldsymbol{F}} + \theta \dot{H} - \mathcal{D}_{loc}$. Insertion into (4.23) give the evolution equation for the entropy

$$\theta \dot{H} = \mathrm{Div}[-\boldsymbol{Q}] + \mathcal{R} + \mathcal{D}_{loc} \ . \tag{4.24}$$

in terms of the plastic dissipation $\mathcal{D}_{loc} \geq 0$ defined in (4.18). Starting from $(4.14)_2$, we obtain the constitutive rate equation $\theta \dot{H} = c\,\dot{\theta} - \mathcal{H}$ with the *heat capacity*

$$c := -\theta \partial^2_{\theta\theta} \hat{\Psi}(\boldsymbol{\varepsilon}, \boldsymbol{\varepsilon}^p, \theta) \tag{4.25}$$

and the *latent heating*

$$\mathcal{H} := \theta \partial_\theta \left[\, \boldsymbol{P} : \dot{\boldsymbol{F}} - \mathcal{D}_{loc} \, \right] = (\theta \partial_\theta \boldsymbol{P}) : \dot{\boldsymbol{F}} - (\theta \partial_\theta \boldsymbol{\sigma}^p) : \dot{\boldsymbol{\varepsilon}}^p \ . \tag{4.26}$$

Insertion into (4.24) finally gives an evolution equation for the temperature

$$c\,\dot{\theta} = \{ \ \mathrm{Div}[-\boldsymbol{Q}] + \mathcal{R} \ \} \ + \ \{ \ \mathcal{H} + \mathcal{D}_{loc} \ \} \ . \tag{4.27}$$

Note that the first bracket vanishes in an adiabatic process, i.e for $\boldsymbol{Q} \equiv 0$ and $\mathcal{R} \equiv 0$. Equation (4.27) is known as the coupled temperature evolution equation of thermoplasticity. The last two terms on the right-hand side characterize the latent (thermoelastic) and dissipative coupling effects. Similar to applications of metal thermoplasticity we expect the situation $|\mathcal{H}| << \mathcal{D}_{loc}$. Investigations of Miehe [66] for entropic thermoelasticity demonstrated the small amount of latent heating. In our subsequent investigation we neglect the latent heating effect in the temperature evolution equation (4.27) by setting

$$\mathcal{H} \approx 0 \ . \tag{4.28}$$

With regard to the construction of staggered solution algorithms for the coupled thermomechanical problem in Chapter 4.6, we write the global field equations as a first-order evolution system

$$\left.\begin{array}{rl} \dot{\boldsymbol{\varphi}} & = \boldsymbol{v} \ , \\ \dot{\boldsymbol{v}} & = \mathrm{Div}[\boldsymbol{P}]/\rho_0 \ , \\ \dot{\theta} & = \mathrm{Div}[-\boldsymbol{Q}]/c + \mathcal{D}_{loc}/c \ , \end{array}\right\} \tag{4.29}$$

where we have dropped the given source terms $\boldsymbol{\gamma}$ and $\mathcal{R}$ in order to obtain a more compact representation. We regard the right hand-side of (4.29) as a function of the *primary variables* $\{ \boldsymbol{\varphi}, \boldsymbol{V}, \theta \}$, i.e. the deformation field, the velocity field and the temperature field. Now consider a time interval $[\, t_n, \, t_{n+1} \,] \subset \mathcal{R}$ where the solution at time t_n is assumed to be known. Then the initial-boundary-value problem of coupled thermoplasticity is completed by the initial conditions

$$\{ \boldsymbol{\varphi}, \boldsymbol{v}, \theta \}|_{(t=t_n)} = \{ \boldsymbol{\varphi}_n, \boldsymbol{v}_n, \theta_n \} \tag{4.30}$$

for the primary variables. The essential boundary conditions for the deformation field and the temperature field are

$$\boldsymbol{\varphi} = \bar{\boldsymbol{\varphi}} \quad \text{on} \ \ \partial\mathcal{B}_\varphi \qquad \text{and} \qquad \theta = \bar{\theta} \quad \text{on} \ \ \partial\mathcal{B}_\theta \ . \tag{4.31}$$

Finally, one has to take into account boundary conditions for the tractions and the heat exchange, i.e.

$$\boldsymbol{P} \cdot \boldsymbol{n} = \bar{\boldsymbol{t}} \quad \text{on} \ \ \partial\mathcal{B}_t \qquad \text{and} \qquad \boldsymbol{Q} \cdot \boldsymbol{n} = \bar{q} \quad \text{on} \ \ \partial\mathcal{B}_q \ , \tag{4.32}$$

where $\boldsymbol{n}$ is the outward normal on the surface $\partial\mathcal{B}$ of the reference configuration. This surface is decomposed according to $\partial\mathcal{B} = \partial\mathcal{B}_\varphi \cup \partial\mathcal{B}_t = \partial\mathcal{B}_\theta \cup \partial\mathcal{B}_q$ and $\partial\mathcal{B}_\varphi \cap \partial\mathcal{B}_t = \emptyset$, $\partial\mathcal{B}_\theta \cap \partial\mathcal{B}_q = \emptyset$. The heat exchange is often assumed to be governed by a constitutive equation formulated in terms of the surface temperature of the form

$$\bar{q} = -k_c\,[\,\theta - \theta_\infty\,] \tag{4.33}$$

where $k_c > 0$ is a convection coefficient and θ_∞ a given temperature of the surrounding medium.

4.4. Specific Constitutive Functions for Glassy Polymers

We now specify the above outlined general constitutive functions for glassy polymers. This concerns specific representations of the free energy function $\hat{\Psi}$ introduced in (4.11) and the viscoplastic flow function $\hat{f}^p$ introduced in (4.19). A great advantage of the proposed formulation in the logarithmic strain space is the simple structure of these equations, which adopt representation of the geometrically linear theory at small strains.

4.4.1. Additive Split of the Free Energy Function. The free energy is assumed to be additively decomposed into *thermoelastic* and *plastic* contributions according to

$$\hat{\Psi}(\boldsymbol{\varepsilon}, \boldsymbol{\varepsilon}^p, \theta) = \hat{\Psi}^e(\boldsymbol{\varepsilon} - \boldsymbol{\varepsilon}^p, \theta) + \hat{\Psi}^p(\boldsymbol{\varepsilon}^p, \theta)\ . \tag{4.34}$$

Note that the first thermoelastic contribution $\hat{\Psi}^e$ is considered to be a function of the elastic logarithmic strain $\boldsymbol{\varepsilon}^e$ defined in (4.5), acting as a potential for the nominal stress. Here, we exploit the additive kinematic structure in the logarithmic strain space. The plastic contribution $\hat{\Psi}^p$ to the free energy defines the energy stored due to plastic configuration alteration, acting as a potential for post-yield hardening through back stresses. Note that, due to the above additive split of the free energy, the dissipative driving force defined in (4.15) appears in the form

$$\boldsymbol{\sigma}^p = \boldsymbol{\pi} - \boldsymbol{\pi}^p \quad \text{with} \quad \boldsymbol{\pi} := \partial_{\boldsymbol{\varepsilon}^e}\hat{\Psi}^e(\boldsymbol{\varepsilon} - \boldsymbol{\varepsilon}^p, \theta) \quad \text{and} \quad \boldsymbol{\pi}^p := \partial_{\boldsymbol{\varepsilon}^p}\hat{\Psi}^p(\boldsymbol{\varepsilon}^p, \theta) \tag{4.35}$$

in terms of the *stress and back–stress tensors* $\boldsymbol{\pi}$ and $\boldsymbol{\pi}^p$ in the logarithmic strain space, respectively. Note, that only the deviatoric part of the driving force $\boldsymbol{\sigma}^p$ enters the flow rule (4.16).

4.4.2. Thermoelastic Contribution to Free Energy. Experimental observations indicate that the deformation in the pre-yield branch is limited to small values compared to the plastic strains attained. For this reason, linear elasticity in the logarithmic strain space is considered to be sufficient for the current scope. For the isotropic thermoelastic response, we adopt from Miehe [66, 67] the constitutive function

$$\hat{\Psi}^e(\boldsymbol{\varepsilon}^e, \theta) = \frac{\kappa}{2}\,\mathrm{tr}^{\,2}[\boldsymbol{\varepsilon}^e] - \kappa\alpha\,\mathrm{tr}[\boldsymbol{\varepsilon}^e](\theta - \theta_0) + \hat{\mu}(\theta)|\,\mathrm{dev}[\boldsymbol{\varepsilon}^e]|^2 + c\,(\,\theta - \theta_0 - \theta\ln[\frac{\theta}{\theta_0}]\,) \tag{4.36}$$

where κ, μ, α and c are the bulk modulus, the shear modulus, the thermal expansion coefficient and the heat capacity coefficient, respectively. The reference ambient temperature is denoted by θ_0. The parameters κ, α and c are considered as constants. as suggested in Boyce, Montagut & Argon [20], the shear modulus $\mu = \hat{\mu}(\theta)$ is assumed to be dependent on the temperature through the empirical relation

$$\hat{\mu}(\theta) = \exp[\,\log(\mu_0) - h(\theta - \theta_0)\,] \tag{4.37}$$

in terms of the modulus μ_0 at the reference temperature θ_0 and sensitivity parameter h. Exploitation of $(4.14)_1$ give the nominal stress

$$\boldsymbol{P} = \boldsymbol{\pi} : \mathbb{Q} \quad \text{with} \quad \boldsymbol{\pi} := -p\mathbf{1} + 2\mu\,\mathrm{dev}[\boldsymbol{\varepsilon}^e] \quad \text{and} \quad p := -\kappa\,(\mathrm{tr}[\boldsymbol{\varepsilon}^e] - \alpha(\theta - \theta_0)) \ , \tag{4.38}$$

which are obtained from the linear stress function $\boldsymbol{\pi}$ in the logarithmic strain space by a post-processing with the transformation tensor $\mathbb{Q}$ defined in (4.8).

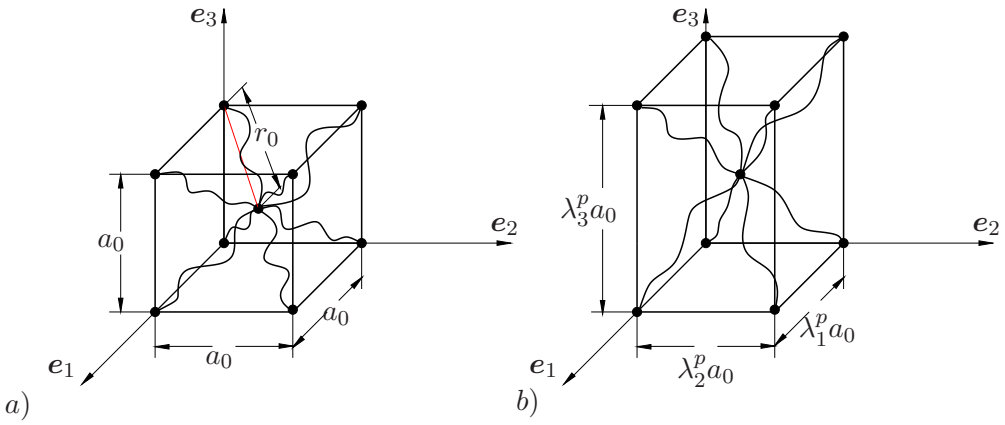

Figure 4.1: 8-chain network in a) undeformed and b) deformed configuration.

4.4.3. Plastic Contribution to Free Energy. The second contribution to the free energy describes a characteristic kinematical hardening effect due to the back stress $\boldsymbol{\pi}^p$ introduced in $(4.35)_3$. This backstress models the intramolecular resistance to the plastic flow due to the alignment of the chains in the principal deformation direction. For this reason, it is common practice to model the post-yield strain hardening by using *polymer network models*. Those models provide a bridge between microscopic and macroscopic deformations through particular kinematical assumptions. Typical examples are the *three chain model* of James & Guth [53] and Wang & Guth [90], the affine *full network model* of Treloar & Riding [86, 88], the non–affine *eight chain model* of Arruda & Boyce [10] and the non–affine *microsphere model* of Miehe, Göktepe & Lulei [72]. The stored free energy due to the distorted polymer network in plastically deformed glassy polymers is assumed to be isotropic and formulated in terms of the *plastic principal stretches* $\{\lambda^p_A\}_{A=1,3}$, i.e. the eigenvalues of the plastic stretch tensor $\boldsymbol{U}^p := \boldsymbol{G}^{p\,1/2} = \exp[\boldsymbol{\varepsilon}^p]$. These are obtained by a spectral decomposition of the plastic Hencky strain $\boldsymbol{\varepsilon}^p$, which is a function of the plastic metric $\boldsymbol{G}^p$ through (4.6). We write

$$\boldsymbol{\varepsilon}^p = \sum_{A=1}^{3} \epsilon^p_A\, \boldsymbol{n}^p_A \otimes \boldsymbol{n}^p_A \quad \text{and} \quad \lambda^p_A := \exp[\epsilon^p_A] \ , \tag{4.39}$$

where $\{\boldsymbol{n}^p_A\}_{A=1,3}$ are the plastic principal directions. With the macroscopic plastic principal stretches $\{\lambda^p_A\}_{A=1,3}$, one computes an *network stretch* Λ^p. For the eight chain model of Arruda & Boyce [10], this network stretch is obtained from

$$\Lambda^{p2} := \frac{1}{3}[\lambda^{p2}_1 + \lambda^{p2}_2 + \lambda^{p2}_3] = \frac{1}{3}\mathrm{tr}[\boldsymbol{G}^p] \ . \tag{4.40}$$

Here, the plastic stretch of a chain extending from the center of a plastically deformed rectangular prism having the edges oriented in the principal plastic directions $\boldsymbol{n}^p_A$ is assumed

to be representative for the whole polymer network, see Figure 4.1a. A more complicated relationship gives the microsphere model. We refer to the recent isothermal approach to glassy polymers by Miehe, Göktepe & Mendez [73] and Göktepe [38]. With the above network stretch relationship $\Lambda^p = \hat{\Lambda}^p(\boldsymbol{\varepsilon}^p)$ at hand, one expresses the energetic state of the full network by the energy of a fictitious prototype chain. For a typical Langevin function, we then are able to define the plastic part of the free energy to

$$\hat{\Psi}^p(\boldsymbol{\varepsilon}^p, \theta) = \hat{\mu}_p(\theta)\hat{N}_p(\theta)\left(\Lambda_r^p\mathcal{L}^{-1}(\Lambda_r^p) + \ln\frac{\mathcal{L}^{-1}(\Lambda_r^p)}{\sinh\mathcal{L}^{-1}(\Lambda_r^p)}\right) . \tag{4.41}$$

Where μ_p and N_p are the material parameters standing for the plastic shear modulus and the number of segments in the fictitious prototype chain, respectively. The function $\mathcal{L}^{-1}$ denotes the inverse of the well-known Langevin function defined by $\mathcal{L}(\cdot) := \coth(\cdot) - 1/(\cdot)$. It can be approximated by the Padè approximation $\mathcal{L}^{-1}(\Lambda_r^p) \approx \Lambda_r^p\,(3 - \Lambda_r^{p2})/(1 - \Lambda_r^{p2})$ as proposed by Cohen [29]. Note that the parameter N_p controls the limited extensibility range of chains through the relative plastic network stretch $\Lambda_r^p := \Lambda^p/\sqrt{N_p}$. Then, the backstress in the logarithmic space defined in $(4.35)_3$ is obtained by the chain rule operation

$$\boldsymbol{\pi}^p := \partial_{\Lambda^p}\tilde{\Psi}^p(\Lambda^p, \theta)\,\partial_{\boldsymbol{\varepsilon}^p}\hat{\Lambda}^p(\boldsymbol{\varepsilon}^p) . \tag{4.42}$$

The first part is directly obtained from (4.41), the second part from (4.40) and (4.39), yielding

$$\partial_{\Lambda^p}\tilde{\Psi}^p = \hat{\mu}_p(\theta)\Lambda^p\frac{3 - \Lambda_r^{p2}}{1 - \Lambda_r^{p2}} \qquad \text{and} \qquad \partial_{\boldsymbol{\varepsilon}^p}\hat{\Lambda}^p = \sum_{A=1}^{3}\frac{\lambda_A^{p2}}{3\Lambda^p}\boldsymbol{n}_A^p \otimes \boldsymbol{n}_A^p , \tag{4.43}$$

where we made use of the result $\partial_{\boldsymbol{\varepsilon}^p}\epsilon_A^p = \boldsymbol{n}_A^p \otimes \boldsymbol{n}_A^p$. Finally, insertion into (4.42) gives the representation of the backstress tensor

$$\boldsymbol{\pi}^p := \frac{\hat{\mu}_p(\theta)}{3}\frac{3 - \Lambda_r^{p2}}{1 - \Lambda_r^{p2}}\boldsymbol{G}^p \qquad \text{with} \qquad \boldsymbol{G}^p = \sum_{A=1}^{3}\lambda_A^{p2}\boldsymbol{n}_A^p \otimes \boldsymbol{n}_A^p . \tag{4.44}$$

Refer to Appendix A for the derivatives obtained by the application of the chain rule required to obtain the results above. Note that only the deviatoric part of the backstress $\boldsymbol{\pi}^p$ enters the flow rule (4.16). The plastic shear modulus $\mu_p = \hat{\mu}_p(\theta)$ in the plastic free energy (4.41) depends on the temperature through the standard expression

$$\hat{\mu}_p(\theta) = \hat{n}_p(\theta)k_B\theta \tag{4.45}$$

of the entropic polymer network theory, see Treloar [87]. Here, $n_p = \hat{n}_p(\theta)$ is the chain density and k_B the Boltzmann constant. However, experiments of glassy polymers show that the strain hardening decreases with increasing temperature. Hence, in contrast to cross–linked rubbers where n and N are considered as constants, the parameters n_p and N_p for the strain hardening of glassy polymers formed by entanglements are considered to be temperature–dependent. Raha & Bowden [78] and Arruda, Boyce & Jayachandran [11] proposed the dependence

$$\hat{n}_p(\theta) = B - D\exp[\,-E_a/R\theta\,] \tag{4.46}$$

of the chain density on the temperature, where B and D are material parameters. E_a is the dissociation energy and R the gas constant. Equation (4.46) describes the thermal

dissociation of entanglements in the molecular network. Introducing the constraint that the molecular network breaks down when the glass transition temperature is reached, i.e. $\hat{n}_p(\theta_g) = 0$, one gets the relationship between the two constants B and D

$$B/D = \exp[\,-E_a/R\theta_g\,] \tag{4.47}$$

as suggested in Basu & van der Giessen [14]. A mass–type balance assumes the number of molecular links to be constant, i.e.

$$\hat{n}_p(\theta)\hat{N}_p(\theta) = \hat{n}_p(\theta_0)\hat{N}_p(\theta_0) = \text{const.}\ , \tag{4.48}$$

see Arruda, Boyce & Jayachandran [11] and references therein. This equation determines the current number of chain segments in terms of the current chain density (4.46) via

$$\hat{N}_p(\theta) = \frac{\hat{n}_p(\theta_0)}{\hat{n}_p(\theta)}\hat{N}_p(\theta_0)\ . \tag{4.49}$$

4.5. Micromechanically–Based Thermoviscoplastic Flow

We now specify the constitutive function $\hat{f}^p$ in (4.19) which determines the amount $\dot{\gamma}^p$ of viscoplastic flow. As stated in (4.19), we make this flow dependent of the driving force $\boldsymbol{\sigma}^p$ with the specific structure (4.35) and the temperature θ. The viscoplastic flow of amorphous glassy polymers is a thermally activated stochastic process occurring locally at sites undergoing rotation of local chain segments, see Kocks, Argon & Ashby [54]. In the context of a polycrystalline material, we can imagine the thermally-activated process as the thermal release of dislocations from regions in which the stress is below some of the peaks of glide resistance. During the homogeneous deformation of glassy polymers after yielding, these local events occur at a much larger scale as compared to one single process at the molecular level. This activation process is conventionally described by the Arrhenius-type equation

$$\dot{\gamma}^p = \hat{f}^p(\mathrm{dev}[\boldsymbol{\sigma}^p], \theta) = \dot{\gamma}_0 \left[\exp\left(-\frac{\Delta F_f}{k_B\theta}\right) - \exp\left(-\frac{\Delta F_b}{k_B\theta}\right)\right]\ . \tag{4.50}$$

in terms of the so-called Boltzmann factor $\exp(-\Delta F_{\{f,b\}}/k_B\,\theta)$ which depends on the Boltzmann constant k_B the temperature θ and the amount of the activation free enthalpy, also called $forward/backward$ activation energy, $\Delta F_{\{f,b\}}$, which will be prescribed for each model separately. For the sake of simplicity from this point on we assume $k_B = k$ for the Boltzmann constant which should not be mistaken with the thermal conductivity appearing in (4.20). In the present constitutive framework we apply two different micromechanically motivated models for plastic flow in glassy polymers. First, the predictive properties of the well-accepted *double-kink theory* of Argon [8] and Boyce, Parks & Argon [21] based on the wedge disclinations, see Figure 4.2a, will be studied. Afterwards, the more complicated and more predictive model developed in Hasan & Boyce [47] and Hasan [46], will be validated as well. The latter considers the presence of a free-volume as a favorable condition for a local site to undergo local shear transformation. In this second model, additionally to the presence of free-volume, which can be described as local unstable voids, the distribution in the free-volume size is also taken into account.

4.5.1. Double-Kink Model. In this theory for the *low temperature* plastic deformation in glassy polymers, the microstructure is initially considered to be an isotropic distribution of randomly zig-zagging polymer molecules, each of which threads through the other. The initiation of plastic strain at a local site is assumed to be caused by the rotation of segments of molecular chains from their initial random orientation into a direction parallel to the principal tensile extension. The process is easier to be visualized as the addition of a molecular kink to the slanted segment AB in Figures 4.2a and 4.2b. The formation of a kink produces the incremental extension and molecular orientation locally. In Figure 4.2, the process of wedge disclination loop has been shown for a reverse deformation problem for illustrative purposes. The resistance offered by the surrounding medium to the formation of the double-kink in the molecular chain is modeled as the elastic interaction of the chains with its neighbors. The rotation of local chain segment produces a strain increment that results in the boundary displacement, enabling an externally applied stress τ to do some work ΔW, which reduces the free energy $\Delta F_{\{f,b\}}$ to the forward activation enthalpy $\Delta F_f = \Delta F - \Delta W$ only. Upon the release of the applied stress, there exists a finite possibility for the molecular segment to return to its original undeformed configuration. The double kink configuration is only irreversible if the surrounding chains also undergo the same process of rotation and the locally stored elastic energy in the surrounding region of the double-kink is dispersed. This local process happens at many points simultaneously and results in a gradual shift from an unaligned orientation to aligned polymer segments. It should be noted that at each unit of time, there is a certain density of sites which reverse their alignment and return to their initial orientation.

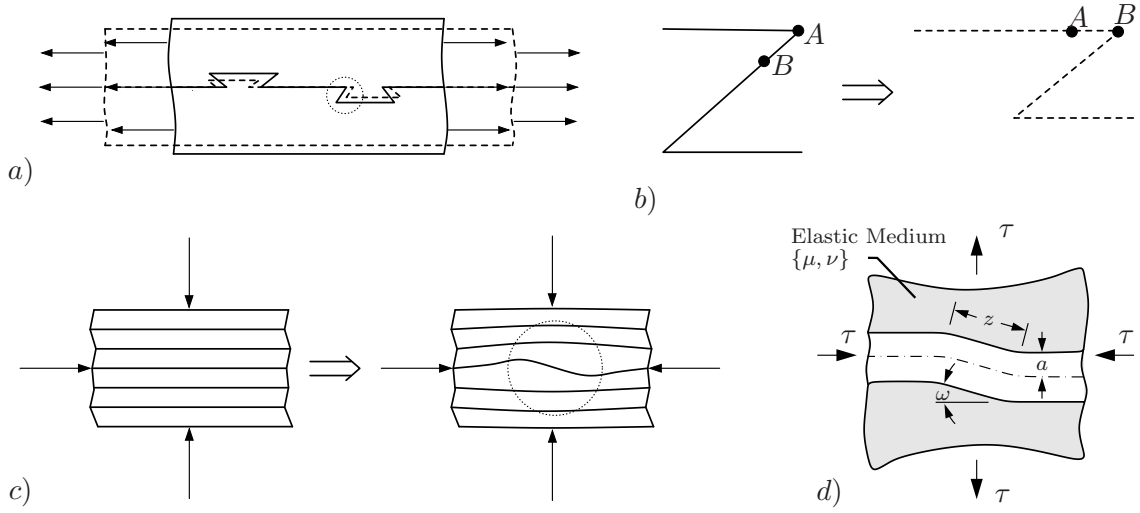

Figure 4.2: *a*) Rotation of local poymer chain segments through the formation of kink. *b*) The unit process of deformation consisting of unbending and bending of a molecular segment at an active corner. *c*) Schematic representation of the the double-kink in polymer chains under reverse deformation. *d*) Zoom in of the marked region in *c*) showing the main molecular components entering the formulation.

Li & Gilman [57] computed the free energy associated with the formation of a double-kink by modeling the displacement field via two wedge disclination loops extending over the chain diameter with their two centers of rotation separated by a finite length. The process can be imagined by considering the molecular chain to be a cylinder surrounded by an elastic medium and the process of formation of a double-kink by two wedge disclinations

equivalent to removal of a triangular wedge shaped material from a pair of incisions and plugging them into the opposite side, followed by joining together all the gaps produced in the cylinder (Figure 4.2d). The free energy of the wedge disclinations was computed based on the distant stress field

$$\Delta F = \frac{3\mu\pi a^3\omega^2}{16(1-\nu)} - \frac{9\mu\pi a^3\omega^2}{8(1-\nu)}\Big(\frac{a}{z}\Big)^5 \ , \tag{4.51}$$

where μ is the shear modulus, ω the strength of the wedge disclinations and ν Poisson's ratio. The parameter z denotes the distance of separation between the two loops and a is the diameter of the cylinder representing the molecular chain. In (4.51), the first term refers to the self energies of the two wedge disclination loops while the second represents their interaction energy. The work done by the external shear stress τ during the formation of the pair of molecular kinks is given as

$$\Delta W = \pi a^3\omega^2\tau\left(\frac{a}{z}\right) \ . \tag{4.52}$$

Thus, the forward activation enthalpy takes the form

$$\Delta F_f = \Delta F - \Delta W = \frac{3\mu\pi a^3\omega^2}{16(1-\nu)} - \frac{9\mu\pi a^3\omega^2}{8(1-\nu)}\Big(\frac{a}{z}\Big)^5 - \pi a^3\omega^2\tau\left(\frac{a}{z}\right) \ . \tag{4.53}$$

In (4.53) an energy extremum appears in the z coordinate. We obtain the saddle point configuration by differentiating the free activation enthalpy with respect to z/a for constant ω and τ/μ, which results in

$$\Big(\frac{z}{a}\Big)^\star = \left(\frac{45}{8(1-\nu)}\frac{\mu}{\tau}\right)^{\frac{1}{6}} \ . \tag{4.54}$$

Substituting (4.54) in (4.53) yields

$$\Delta F_f = \frac{3\mu\pi a^3\omega^2}{16(1-\nu)}\left[1 - \left(\frac{\tau}{s_0}\right)^{\frac{5}{6}}\right] \ , \tag{4.55}$$

with the athermal shear strength $s_0 := 0.077\mu/(1-\nu)$. It is important to mention that the second Arrhenius-type term in (4.50), related with the backward activation energy, is not existent in the double-kink law. Boyce, Parks & Argon [21] accounted for a phenomenological evolution of strain softening after the macroscopic yielding by proposing an evolution for the athermal shear strength s_0

$$\dot{s} = h\,(1 - s/s_{ss})\,\dot{\gamma}^p \quad \text{with} \quad s(0) = s_0 \quad \text{and} \quad s(\infty) = s_{ss} \ . \tag{4.56}$$

When the expression for ΔF_f is used in the Arrhenius-type evolution equation for the macroscopic strain rate we get

$$\dot{\gamma}^p = \dot{\gamma}_0 \exp\left[-\frac{As}{\theta}\left(1 - \Big\{\frac{\tau}{s}\Big\}^{\frac{5}{6}}\right)\right] \ , \tag{4.57}$$

with the effective driving force τ in terms of the invariant $\sqrt{J_2(\mathrm{dev}[\boldsymbol{\sigma}^p])}$ of the driving stress deviator

$$\tau := \sqrt{\frac{\mathrm{dev}[\boldsymbol{\sigma}^p] : \mathrm{dev}[\boldsymbol{\sigma}^p]}{2}} = \frac{|\,\mathrm{dev}[\boldsymbol{\sigma}^p]\,|}{\sqrt{2}} \ . \tag{4.58}$$

$\dot{\gamma}_0$ and $A := 39\pi\omega^2 a^3/16k$ are material parameters. It can be noted here that the plastic strain rate begins to increase when the applied stress τ starts to become greater than the athermal shear strength s, which can be looked up as a yield limit. Insertion of $(4.58)_3$ into (4.57) yields the final form

$$\boxed{\dot{\gamma}^p = \dot{\gamma}_o \exp\left[-\frac{A\,s}{\theta}\left(1 - \left\{\frac{|\operatorname{dev}[\boldsymbol{\sigma}^p]\,|}{s\sqrt{2}}\right\}^{\frac{5}{6}}\right)\right] \geq 0}\,. \tag{4.59}$$

It can be noted that the concept of an orientated chain segment returning to its original state continuously during the deformation is not comprehensively taken into consideration. The double-kink molecular chain segment is assumed to interact effectively with only two neighboring molecules on the plane of formation of the kink and the return of a rotated chain segment to its original state is possible without the production of a back strain when the segment causes an orientation of one of its two neighboring chain segments having a lesser forward activation barrier. For a much more detailed implementation of the double kink model in 3–D the reader is refered to the recent works of Göktepe [38] and Miehe, Göktepe & Mendez [73]. The next molecular model explaining plastic flow in glassy polymers does not make such an assumption and is more probabilistic in nature.

4.5.2. Micromechanical Model Based on the Distribution of Free Volume. The concept of *free volume* was introduced during the early investigations involving the influence of the instantaneous microstructural state of the material on the ease of molecular mobility. This term was used in the sense of vacancies which facilitate the drifting motion of a molecule. The free volume theory in this case considers the ease of local chain segment rotation to depend on the availability of *excess* or *empty volume*. Experiments carried out by Hasan et al. [48] have monitored the relationship between the microstructural state of the glassy polymers and the macroscopic response by monitoring the free volume using an experiment known as Positron Annihilation Lifetime Spectroscopy (PALS). In the context of understanding the overall mechanical response of the material, we focus here on the microstructural changes during the post-yield strain softening of it. The mentioned PALS experiments were conducted on cylindrical specimens of PMMA previously heated to 15°C above the glass transition temperature for roughly 3hr in order to erase any thermal prehistory of the material. The effect of post-yield straining was studied by conducting uniaxial compression tests up to varying levels of strains for the same temperature and constant strain rate.

In the PALS experiments, a positron obtained from the β^+ decay of radioactive sources is shot into the sample. As the positron enters the sample, they quickly annihilate with electrons into γ quanta. A fraction of the positrons entering the sample forms positronium (Ps), which are hydrogen-like atoms, exist in two distinct states, viz. o-Ps (orthopositronium) and p-Ps (para-positronium). Both the positrons as well as positronium tend to move towards low-density regions, to minimize their energy prior to annihilation. Owing to the varied lifetime of o-Ps, p-Ps and positron in vacuum and condensed sample matter, we can characterize the microstructure of the material by analyzing the characteristic positron lifetime spectrum, which is is usually split into three components. It would be important to note that the lifetime of o-Ps ($1.40 \cdot 10^{-07}$s) is much higher than lifetime of p-Ps ($1.20 \cdot 10^{-10}$s) in vacuum. The study involves observing the longest lifetime τ_3 and the normalized intensity I_3 of o-Ps as a qualitative indication of the mean free volume size

and the density of free volume sites. The larger the average free volume size, the longer the lifetime τ_3 of the o-Ps atoms due to lesser overlap with the molecular electrons. The greater the number of free-volume sites, the higher the probability (normalized intensity I_3) that an incident positron will annihilate as o-Ps. When the results of the PALS experiment are compared along side the true stress vs. true strain response of the material, we observe that the value of I_3 remains constant whereas τ_3 increases during the part of the response exhibiting strain softening. These results indicate an increase in free volume content during the strain softening in the true stress vs. true strain response!

In the second constitutive model presented in this work, the changes occurring in the microstructure of glassy polymers during deformation are characterized by the evolution in the distribution of the aforementioned free volume. The contribution of Hasan & Boyce [47] to the representation of plastic flow in glassy polymers is two-fold. *First*, well aware of the fact that local molecular rearrangements in glassy polymers are thermoreversible, they included a mechanism to acquaint for these reverse transformations occurring inside the material. This yielded the *b*ackward activation term seen in (4.50). *Second*, they characterized the distributed nature of the microstructure by taking into consideration a distribution of free volume sizes that can be correlated with a distribution of activation energies for the thermalized, local inelastic shear transformations that occur during plastic flow. The higher the size of the free volume, the easier it is for the local chain segments to rotate, or in other words, the lesser the forward activation enthalpy, which in turn corresponds to a higher probability of occurrence of a local, strain-producing transformation event. We begin the mathematical representation of the model from the classical form of the Arrhenius-type equation presented in (4.50). If we assume the plastic strain increment during the forward transformation to be $+\Delta\gamma$ and that during the backward transformation to be $-\Delta\gamma$, then the macroscopic plastic flow rate is given by

$$\dot{\gamma}^p := \dot{\gamma}_0 \int_0^\infty \int_0^\infty \psi(\Delta F_f, \Delta F_b) \left[\exp\left(-\frac{\Delta F_f}{k\theta} \right) - \exp\left(-\frac{\Delta F_b}{k\theta} \right) \right] d\Delta F_f \; d\Delta F_b \tag{4.60}$$

where the term $\dot{\gamma}_o$ is defined as

$$\dot{\gamma}_o = \omega_0 D \Delta\gamma = \omega_0 \frac{V}{\omega} \frac{2\gamma^T \omega}{V} = \omega_0 2\gamma^T \; . \tag{4.61}$$

The total number of shear transformation sites D can be computed from the reciprocal of the activation volume ω. V is the total volume, ω_0 is the attempt frequency and γ^T is the shear transformation strain. The term $\psi(\Delta F_f, \Delta F_b)$ is a probability density function that represents the distribution over the activation energy space due to the distribution of free volume in the microstructure. Figure 4.3 shows the *pseudo-Gaussian* distribution function employed for this purpose. It has a *finite bandwidth* constructed from the monotonic parts of $\exp(x)\sin(x)$ between the range a to $a + \frac{3\pi}{4\alpha}$ and $\exp(-x)\sin(x)$ between $a + \frac{3\pi}{4\alpha}$ and $a + \frac{3\pi}{2\alpha}$. The explicit function reads

$$\psi(\Delta F) \; = \; \begin{cases} \frac{1}{2A_1} \exp\left(\alpha(\Delta F - a)\right) \sin\left(\alpha(\Delta F - a)\right) & \text{if} \quad a \; \leq \; \Delta F \; \leq \; a + \frac{3\pi}{4\alpha} \\ \frac{1}{2A_2} \exp\left(-\alpha(\Delta F - a')\right) \sin\left(\alpha(\Delta F - a')\right) & \text{if} \quad a + \frac{3\pi}{4\alpha} \; \leq \; \Delta F \; \leq \; a + \frac{3\pi}{2\alpha} \\ 0 & \text{otherwise} \; . \end{cases} \tag{4.62}$$

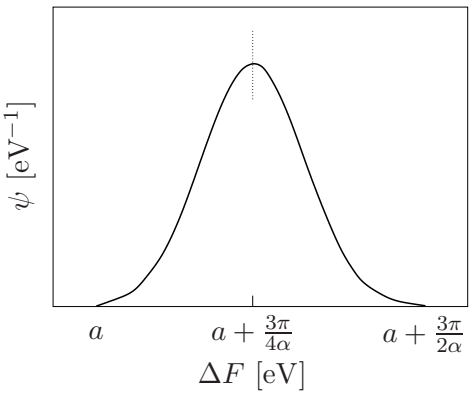

Figure 4.3: The pseudo-gaussian distribution function of activation energies for the thermalized, local inelastic shear transformations that occur during plastic flow.

The terms A_1 and A_2 normalize the area under the monotonic parts of each curve,

$$A_1 = \int_a^{a+\frac{3\pi}{4\alpha}} \exp\left(\alpha(\Delta F - a)\right) \sin\left(\alpha(\Delta F - a)\right) d\Delta F = \frac{1}{2\alpha}[1 + \sqrt{2}e^{3\pi/4}] \ ,$$

$$A_2 = \int_{a+\frac{3\pi}{4\alpha}}^{a+\frac{3\pi}{2\alpha}} \exp\left(-\alpha(\Delta F - a')\right) \sin\left(\alpha(\Delta F - a')\right) d\Delta F = A_1/e^{\pi}$$

where $a' = a + \frac{\pi}{2\alpha}$. With the intention to obtain a general macroscopic rate flow that takes into account the forward and backward activation processes, we can trace back the single-valued form of the effective forward activation enthalpy in the double-kink model by substituting a Dirac delta function as ψ in (4.60). The Dirac delta function can be thought of as a single-valued function on the real line which is zero everywhere except at the origin, where it is infinite

$$\delta(x) = \begin{cases} \infty & \text{if } x = 0 \\ 0 & \text{if } x \neq 0 \end{cases} \quad \text{with} \quad \int_{-\infty}^{+\infty} \delta(x) dx = 1 \ .$$

When (4.60) is integrated with $\psi(\Delta F_f, \Delta F_b) := \delta(\Delta F_f, \Delta F_b)$, the form of the Arrhenius-type equation used in the double-kink model (dropping the exponential containing ΔF_b) can be derived. The terms involving the forward activation enthalpy ΔF_f and the backward activation enthalpy ΔF_b can be recast into a so-called *Eyring form* for the stress dependence of the activation free energy by assuming $p = q = 1$ in (4.55)

$$\Delta F_f = \Delta F_0 \left[1 - \left(\frac{\tau}{\tau_0}\right)^p\right]^q \tag{4.63}$$

yielding

$$\Delta F_f = \Delta F_0 - \tau \Delta\nu \quad \text{with} \quad \Delta\nu := \Delta F_0/\tau_0 \ . \tag{4.64}$$

Inserting $(4.64)_1$ in (4.60) and introducing a similar dependence for the backward activation enthalpy on the stress we get

$$\dot{\gamma}^p := \dot{\gamma}_0 \int_0^{\infty} \psi(\Delta F) \left[\exp\left(-\frac{\Delta F - \tau \Delta\nu_\tau^\star(\theta)}{k\theta}\right) - \exp\left(-\frac{\Delta F + \tau \Delta\nu_\tau^\star(\theta)}{k\theta}\right) \exp\left(\frac{S}{k\theta}\right)\right] d\Delta F \ , \tag{4.65}$$

with the material parameter $\Delta\nu_\tau^\star(\theta)$ as the temperature dependent shear activation volume. $\Delta\nu_\tau^\star(\theta)$ is scaled by the shear modulus μ over a range of temperatures below the glass transition temperature T_g in the form

$$\mu(\theta_0)\Delta\nu_\tau^\star(\theta_0) = \mu(\theta)\Delta\nu_\tau^\star(\theta) \ . \tag{4.66}$$

In (4.65), the newly introduced term S represents the mean local transformation strain energy stored in the neighborhood of a forwardly activated site. It prevents the same local site from undergoing repeated transformations by exerting a back stress on the transformed region and hence increase the forward activation enthalpy for further activations. Therefore, S is added to the probability of backward transformations. The term involving forward activation enthalpy does not include any contribution from S based on the assumption that the sites without having any stored local transformation energy in their vicinity would be the primary contributor to the plastic strains. The pressure dependency of the yield can also be introduced through the pressure activation volume term $\Delta\nu_p^\star(\theta)$ in (4.65)

$$\begin{aligned}\dot\gamma^p := \dot\gamma_0 \int_0^\infty \psi(\Delta F) \left[\exp\left(-\frac{\Delta F - \tau\Delta\nu_\tau^\star(\theta) + p\Delta\nu_p^\star(\theta)}{k\theta}\right)\right. \\ \left. - \exp\left(-\frac{\Delta F + \tau\Delta\nu_\tau^\star(\theta) - p\Delta\nu_p^\star(\theta)}{k\theta}\right)\exp\left(\frac{S}{k\theta}\right)\right] d\Delta F \ ,\end{aligned} \tag{4.67}$$

where the pressure activation volume $\Delta\nu_p^\star(\theta)$ shows a similar dependency on temperature as the shear activation volume in (4.66)

$$\kappa(\theta_0)\Delta\nu_p^\star(\theta_0) = \kappa(\theta)\Delta\nu_p^\star(\theta) \ . \tag{4.68}$$

Splitting the terms which are function of ΔF in (4.67) yields

$$\begin{aligned}\dot\gamma^p := \dot\gamma_0 \int_0^\infty \psi(\Delta F)\exp\left(-\frac{\Delta F}{k\theta}\right) \left[\exp\left(-\frac{-\tau\Delta\nu_\tau^\star(\theta) + p\Delta\nu_p^\star(\theta)}{k\theta}\right)\right. \\ \left. - \exp\left(-\frac{\tau\Delta\nu_\tau^\star(\theta) - p\Delta\nu_p^\star(\theta) + S}{k\theta}\right)\right] d\Delta F \ .\end{aligned} \tag{4.69}$$

Using the intervals specified for ψ in (4.62), we can rewrite the previous equation as,

$$\begin{aligned}\dot\gamma^p := \left[\exp\left(\frac{\tau\Delta\nu_\tau^\star(\theta) - p\Delta\nu_p^\star(\theta)}{k\theta}\right) - \exp\left(\frac{-\tau\Delta\nu_\tau^\star(\theta) + p\Delta\nu_p^\star(\theta) + S}{k\theta}\right)\right] \\ \left(\int_a^{a+\frac{3\pi}{4\alpha}} \dot\gamma_0\psi(\Delta F)\exp\left(-\frac{\Delta F}{k\theta}\right) d\Delta F + \int_{a+\frac{3\pi}{4\alpha}}^{a+\frac{3\pi}{2\alpha}} \dot\gamma_0\psi(\Delta F)\exp\left(-\frac{\Delta F}{k\theta}\right) d\Delta F\right) \ .\end{aligned} \tag{4.70}$$

Integrating the complete equation over the activation energy space returns the macroscopic flow rule for this model based on the distribution of the free volume. The terms $\dot\gamma_1^p$ and $\dot\gamma_2^p$ can be verified by using the method of integration by parts.

$$\boxed{\dot\gamma^p := (\dot\gamma_1^p + \dot\gamma_2^p)\left[\exp\left(\frac{\tau\Delta\nu_\tau^\star(\theta) - p\Delta\nu_p^\star(\theta)}{k\theta}\right) - \exp\left(\frac{-\tau\Delta\nu_\tau^\star(\theta) + p\Delta\nu_p^\star(\theta) + S}{k\theta}\right)\right]} \tag{4.71}$$

where

$$\dot{\gamma}_1^p = \dot{\gamma}_0 \exp\left(-\frac{a}{k\theta}\right) \frac{1}{1+(1-\hat{\eta})^2} \left[\frac{\sqrt{2}+e^{3\pi(1-\hat{\eta})/4}(2-\hat{\eta})}{\sqrt{2}+2e^{3\pi/4}}\right] ,$$

$$\dot{\gamma}_2^p = \dot{\gamma}_0 \exp\left(-\frac{a'}{k\theta}\right) \frac{1}{1+(1+\hat{\eta})^2} \left[\frac{\sqrt{2}e^{\pi/4}e^{-\pi\hat{\eta}}+(2+\hat{\eta})e^{\pi}e^{-\pi\hat{\eta}/4}}{\sqrt{2}e^{\pi/4}+2e^{\pi}}\right]$$

and $\hat{\eta} = \alpha^{-1}/k\theta$. The mathematical model seeks to capture the temperature (θ), pressure (p) and rate dependency of the macroscopic yield in glassy polymers by means of describing the evolution in the distribution of local free volume sites at the microstructure level. The three internal variables present in this mathematical model are the position a and range α^{-1} of the distribution $\psi(\Delta F)$ as well as the mean locally stored transformation strain energy S.

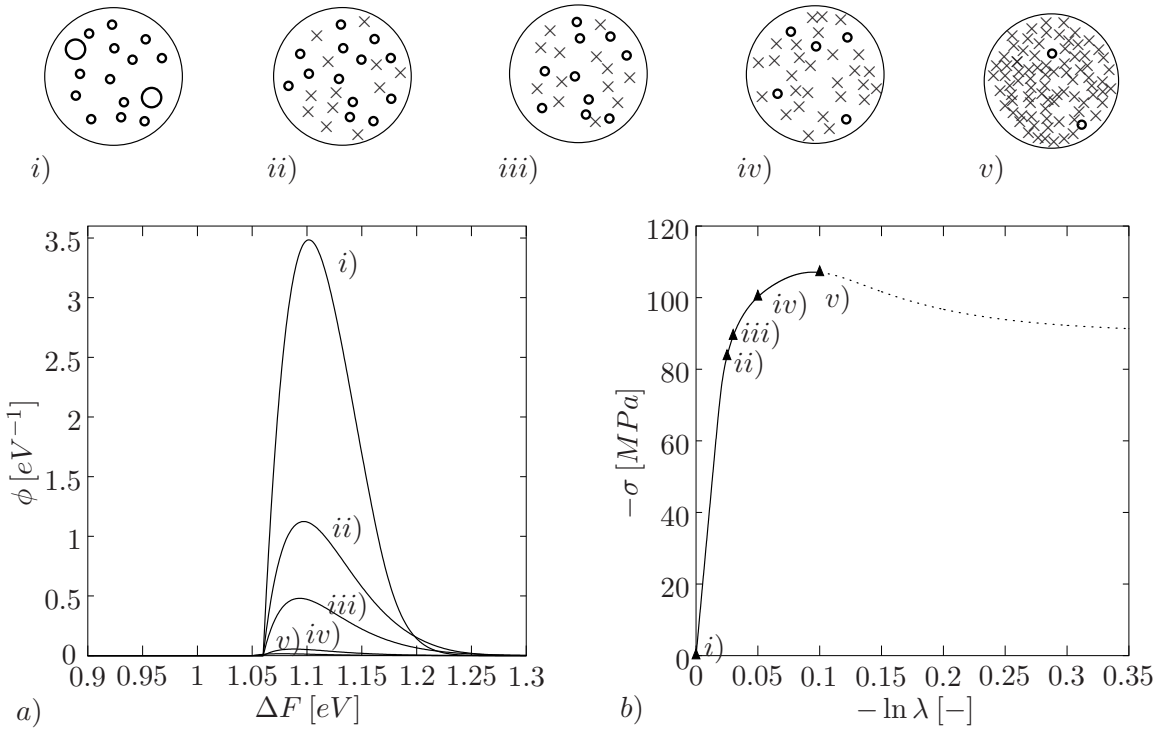

Figure 4.4: Evolution of microstructure during inelastic deformation *before* yield. *a*) Curves marking the distribution of the probablity distribution of available sites $\phi(\Delta F)$. *b*) True stress vs. true strain curve showing the levels at which the microstructure is schematically drawn. *i*)–*v*) Schematic representation of the evolution in microstructure.

A schematic representation of the microstructure at certain pre-defined levels of strain and its associated distribution function $\phi := \psi(\Delta F)\exp\left(-\frac{\Delta F}{k\theta}\right)$ over the activation energy space are shown in Figures 4.4 and 4.5. The circles ($\circ$) in this schematic representation of the microstructure stand for the *free volume sites*, where the varying radius represent their distribution; the cross marks ($\times$) represent the *mean locally stored transformation strain energy*. The flow process is split into two figures, wherein Figure 4.4 depicts the pre-yield region whereas Figure 4.5 covers the post-yield strain softening.

The five pre-defined regions marked *i*) to *v*) in Figure 4.4, marking the strain levels 0, 0.025, 0.03, 0.05 and 0.1, are chosen as presented in Hasan & Boyce [47]. As it can be clearly seen, there are several sites having a reasonably large free volume size that

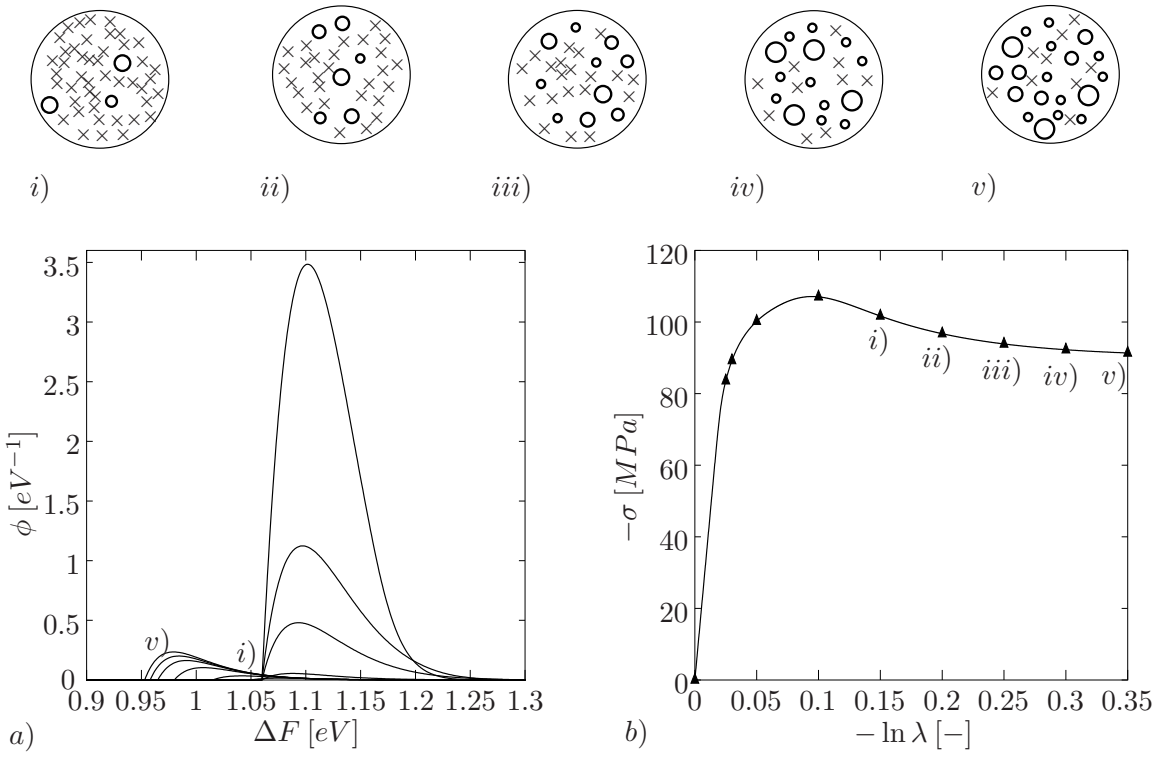

Figure 4.5: Evolution of microstructure during inelastic deformation *after* yielding. *a)* Curves marking the distribution of the probablity distribution of available sites $\phi(\Delta F)$. *b)* True stress vs. true strain curve showing the levels at which the microstructure is schematically drawn. *i)*–*v)* Schematic representation of the evolution in microstructure.

can be easily transformed in the early stages of deformation. The larger the free volume size, the easier it becomes for the local chain segments to rotate, and therefore, the lesser the forward activation enthalpy required for the rotations. In *ii)* the radius of the circles decreases as the presence of cross signs increases, indicating that the transformation strain energy elastically stored in the relatively rigid surrounding material of these free volume sites is larger. This has two effects: firstly, the stored energy applies a back stress which facilitates backward transformations after the removal of the applied load. Secondly, the locally stored energy prevents multiple shear transformation events to occur at the same site and thereby increases their forward activation enthalpy barrier, represented by decrease in radius. As the stress level increases in stages *iii)* - *v)*, more sites having relatively lesser free volume get forwardly activated, contributing to the inelastic strains. The increasing non-linear elastic to inelastic transition in the pre-yield region of the true stress–true strain diagram in Figure 4.4b is observed as the shift of the fraction of the distribution $\phi(\Delta F)$ towards higher activation energy with increasing true strain. As the stress level reaches the macroscopic yield, the process of progressively transforming higher activation energy sites becomes more difficult due to the depletion of further material in the neighborhood for the storage of local transformation strain energy. The locally stored mean transformation strain energy hereafter goes into the creation of new *soft sites* which have a relatively high free volume size as depicted in Figure 4.5. Here, we look at five regions in the post-yield process at strain levels 0.15, 0.20, 0.25, 0.30 and 0.35. The creation of new sites facilitates the flow in the material without much hindrance, resulting in strain softening until the material reaches a steady-state flow condition. This is evident from the shift of the curves representing $\phi(\Delta F)$ to the left (lower activation energy) after

the yield. There is a constant increase in the number of the free volume sites that are responsible for the increasing shift from i) to v).

Evolution of Internal Variables. As described in Chapter 4.5.2, the model explains the non-linear pre-yield elastic to inelastic transition, yielding and post-yield strain softening in terms of the evolution in microstructure (distribution of free volume sites $\phi(\Delta F)$). The internal variables a and α^{-1} describe the distribution of the probability density function, which can be correlated with the available distribution of free volume. Based on the physical picture presented in the previous section, the evolution of the internal variables represents the development in microstructure mathematically. The evolution of a generic internal variable x based on the concept of first order kinetics is given as

$$\partial_{\gamma^p} x = \frac{[x - x_{eq}(\tau)]\omega}{\dot{\gamma}^p} \ , \tag{4.72}$$

where ω is known as the effective activation frequency. The internal variable a defines

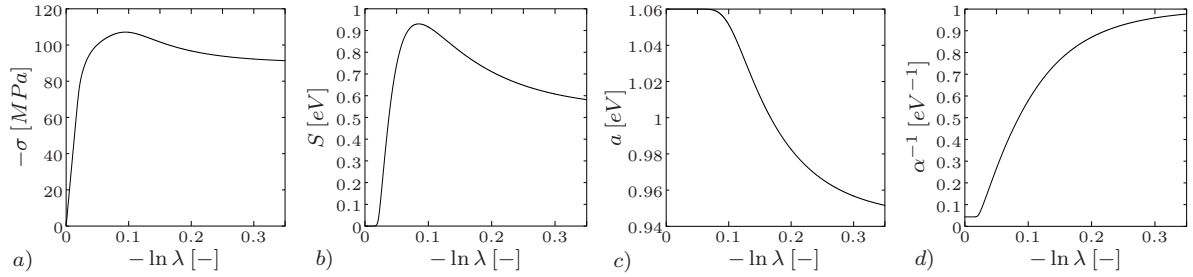

Figure 4.6: Evolution of internal variables for the case of one-dimensional problem. *a*) True stress vs. true strain curve at temperature $\theta = 273°C$ and true strain rate $\dot{\varepsilon} = 0.001s^{-1}$. *b*) Evolution of mean local transformation strain energy $S[eV]$. *c*) Evolution of $a[eV]$. *d*) Evolution of $\alpha^{-1}[eV^{-1}]$.

the left most position of the distribution $\psi(\Delta F)$. As seen in Figure 4.6c for a purely one-dimensional case having no kinematic hardening, no shift in the value of a is observed until the stress value reaches the yield point (seen in Figure 4.6c as its corresponding yield strain). The decrease is marked by the creation of new sites in the post-yield region with high free volume size, which shifts the distribution towards lower activation energy levels. The evolution equation for a is given as

$$\dot{a} = [a_{eq} - a] f(\gamma^p)\omega \tag{4.73}$$

where the value of a does not change till its value is lesser than the parameter a_{eq}. Figure 4.6a represents the true stress–true strain curve for a one-dimensional problem of visco-plasticity at a temperature $\theta = 23°\mathrm{C}$ and true strain rate $\dot{\epsilon} = 1 \cdot 10^{-3}\ \mathrm{s}^{-1}$. The material parameters for this study were taken from Hasan & Boyce [47]. The function $f(\gamma^p)$ is defined in terms of a double exponential function that remains close to 0 at lower stress and rapidly increases to unity in the vicinity of the yield stress

$$f(\gamma^p) = \exp\left(-\zeta \exp\left(-\zeta\gamma^p\right)\right) \ . \tag{4.74}$$

The variable $\dot{\alpha}^{-1}$ characterizes the range of $\psi(\Delta F)$ and as seen in Figure 4.6d for the one-dimensional case, gaining in non-linearly with increasing deformation. The modeling

of the non-linear elastic to inelastic transition in the pre-yield region is done by the non-linear evolution in $\dot{\alpha}^{-1}$ as a consequence of the rapid decrease in the regions of relatively high local free volume. The increase in $\dot{\alpha}^{-1}$ increases the range of the effective activation energy. The evolution equation for $\dot{\alpha}^{-1}$ takes the form

$$\dot{\alpha}^{-1} = [\alpha^{-1} - \alpha_{eq}^{-1}]\omega \ . \tag{4.75}$$

The mean local transformation strain energy S plays a crucial role in the complete model as the term responsible for the creation of new free volume sites after yield has occurred. In the evolution of S, a first term $\beta\tau\dot{\gamma}^p$ is considered as the fraction β of the stored inelastic work of deformation $\tau\dot{\gamma}^p$ increasing the value of S. Additionally, a second term is included decreasing S due to the expenditure of the mean local transformation strain energy in creating potential sites for the inelastic strain to occur. The first term has a dominant effect during the pre-yield region and the second is largely responsible for the decrease in the overall value of S during the post-yield strain softening. This evolution takes finally the form

$$\dot{S} = \beta\tau\dot{\gamma}^p - S\omega \ , \tag{4.76}$$

with

$$\beta = \beta_1[1 + \beta_2 \exp\left(-\beta_3\gamma^p\right)] \tag{4.77}$$

meaning that the rate of storage of the inelastic work decreases with increasing inelastic strain. Figure 4.6b shows the evolution with true strain for S in the one-dimensional case. In each of the evolution equations for the internal variables, the term ω signifies the effective activation energy. We observe that the evolution of ω is analogous to $\dot{\gamma}^p$,

$$\begin{aligned}\dot{\omega} := &\left[\exp\left(\frac{\tau\Delta\nu_\tau^\star(\theta) - p\Delta\nu_p^\star(\theta)}{k\theta}\right) - \exp\left(\frac{-\tau\Delta\nu_\tau^\star * (\theta) + p\Delta\nu_p^\star(\theta) + S}{k\theta}\right)\right] \\ &\left(\int_a^\infty \dot{\omega}_0\psi(\Delta F)\exp\left(-\frac{\Delta F}{k\theta}\right)d\Delta F\right) \ ,\end{aligned} \tag{4.78}$$

$$\dot{\omega} := (\omega_1 + \omega_2)\left[\exp\left(\frac{\tau\Delta\nu_\tau^\star(\theta) - p\Delta\nu_p^\star(\theta)}{k\theta}\right) - \exp\left(\frac{-\tau\Delta\nu_\tau^\star(\theta) + p\Delta\nu_p^\star(\theta) + S}{k\theta}\right)\right] \ , \tag{4.79}$$

where

$$\omega_1 = \dot{\omega}_0\exp\left(-\frac{a}{k\theta}\right)\frac{1}{1 + (1-\hat{\eta})^2}\left[\frac{\sqrt{2} + e^{3\pi(1-\hat{\eta})/4}(2-\hat{\eta})}{\sqrt{2} + 2e^{3\pi/4}}\right] \ ,$$

$$\omega_2 = \dot{\omega}_0\exp\left(-\frac{a'}{k\theta}\right)\frac{1}{1 + (1+\hat{\eta})^2}\left[\frac{\sqrt{2}e^{\pi/4}e^{-\pi\hat{\eta}} + (2+\hat{\eta})e^{\pi}e^{-\pi\hat{\eta}/4}}{\sqrt{2}e^{\pi/4} + 2e^{\pi}}\right] \ ,$$

and $\hat{\eta} = \alpha^{-1}/k\theta$. For a much more detailed implementation of the theory of the distributed free volume in 3–D see Iyer [52].

4.6. Algorithmic Implementation of Finite Thermoviscoplasticity

In this chapter we discuss aspects of the numerical implementation of the model of thermoviscoplasticity outlined above. We construct a staggered global solution procedure for the coupled thermomechanical problem governed by the balance of linear momentum and energy, outline details of the constitutive update algorithm for the dissipative variables and perform, with regard to the application of Newton–type iterative solvers, a consistent linearization of the nonlinear system of equations.

4.6.1. Thermomechanical Coupling Algorithm. In the interval $[\,t_n,\,t_{n+1}\,]$ the system of thermomechanical equations (4.29) can be integrated. This results in a time-discrete system of equations which is fully coupled in the variables $\{\,\boldsymbol{\varphi}_{n+1},\,\boldsymbol{v}_{n+1},\,\theta_{n+1}\}$ at time t_{n+1}. Algorithms for such a monolithic set of non-linear coupled thermomechanical equations have been discussed for example by Argyris & Doltsinis [2] and Simo & Miehe [31], among others. In contrast to this approach, we consider here a scheme which yields an algorithmic decoupling within the time interval and result in partitioned symmetric structures for mechanical and thermal sub–problems. We base the construction of this algorithm on the methodology of operator-splitting which has been applied to coupled thermomechanical problems by Simo & Miehe [83] and Miehe [66, 67]. The algorithm is obtained by a split of the non-linear evolution system (4.29) into the two parts

$$(M):\ \left\{\begin{array}{rl}\dot{\boldsymbol{\varphi}} &= \boldsymbol{v}\\ 0 &= \mathrm{Div}[\boldsymbol{P}]\\ \dot{\theta} &= 0\end{array}\right.\quad\text{and}\quad (T):\ \left\{\begin{array}{rl}\dot{\boldsymbol{\varphi}} &= 0\\ \dot{\boldsymbol{v}} &= 0\\ \dot{\theta} &= \mathrm{Div}[-\boldsymbol{Q}]/c+\mathcal{D}_{loc}/c\end{array}\right. \tag{4.80}$$

for the quasistatic case. Problem (M) defines an isothermal sub-problem at *frozen temperature* θ_n which can be solved for the configuration $\boldsymbol{\varphi}$ and the velocity $\boldsymbol{v}$. Problem (T) is a pure thermal heat-conduction problem at *frozen configuration* $\boldsymbol{\varphi}$ which can be solved for the temperature θ. In a typical time step $\Delta t := t_{n+1} - t_n$, the thermomechanical coupling algorithm is considered as the composition

$$ALGO_{TM} = ALGO_T \circ ALGO_M \tag{4.81}$$

of two sub-algorithms.

Mechanical Predictor. The first sub-algorithm is an *isothermal deformation predictor* based on a backward Euler integrator is governed by the two equations

$$(ALGO_{M1}):\ \hat{G}_M(\delta\boldsymbol{\varphi},\boldsymbol{\varphi}) := \int_{\mathcal{B}} \nabla_X\delta\boldsymbol{\varphi} : \hat{\boldsymbol{P}}^{algo}(\nabla_X\boldsymbol{\varphi};\boldsymbol{\mathfrak{q}}_n,\theta_n)dV = 0 \tag{4.82}$$

for the update of the deformation $\boldsymbol{\varphi}$ under quasi–static conditions

$$(ALGO_{M2}):\ \boldsymbol{v} = (\boldsymbol{\varphi}-\boldsymbol{\varphi}_n)/\Delta t \tag{4.83}$$

for the update of the velocity $\boldsymbol{v}$. All variables without subscript are understood to be evaluated at time t_{n+1}. The algorithmic stresses $\boldsymbol{P}^{algo}$ are obtained by executing the local stress update algorithm outlined in the equations (4.85)–(4.92) below at *frozen temperature* θ_n. The weak form (4.82) is obtained from the time-discrete counterpart of $(4.80)_2$ by a standard Galerkin procedure. Here, we dropped the stress boundary term in order to get a compact representation. $\delta\boldsymbol{\varphi}$ is a virtual displacement field defined on the reference configuration $\mathcal{B}$), that satisfies the homogeneous mechanical boundary conditions $\delta\boldsymbol{\varphi} = 0$ on $\partial\mathcal{B}_\varphi$).

Thermal Corrector. A second sub-algorithm is a *heat conduction corrector*, again based on the backward Euler integrator,

$$(ALGO_T):\ \hat{G}_T(\delta\theta,\theta) := \int_{\mathcal{B}}\{\,\delta\theta\,\frac{c}{\Delta t}\,(\theta-\theta_n)+\nabla_X\delta\theta\cdot k\boldsymbol{C}^{-1}\nabla_X\theta-\delta\theta\,\mathcal{D}^{algo}_{loc}\,\}dV = 0\,. \tag{4.84}$$

It determines the current temperature θ at *frozen deformation and velocity* $\boldsymbol{\varphi}$ and $\boldsymbol{v}$, which were obtained in the predictor phase. The expression follows by a standard Galerkin procedure from the time-discrete counterpart of $(4.80)_6$. Again, we dropped the surface term in order to keep the representation compact. The algorithmic dissipation $\mathcal{D}_{loc}^{algo}$ follows from the local update algorithm of the dissipative variables within the isothermal deformation predictor phase, see (4.93) below. $\delta\theta$ denotes a virtual temperature field defined on the reference configuration $\mathcal{B}$, which satisfies the homogeneous thermal boundary conditions $\delta\theta = 0$ on $\partial\mathcal{B}_\theta$. The overall thermomechanical coupling algorithm (4.81) in a typical time step is the composition of the two sub-algorithms (4.82) and (4.84).

Alternatively to the *isothermal split* algorithm described above, an *isentropic split* has also been used in our group in the past. A problem $(ALGO_M)$ now defines an *isentropic* deformation at *frozen entropy* H_n which can be solved for the configuration $\boldsymbol{\varphi}$ and the velocity $\boldsymbol{v}$. Problem $(ALGO_T)$ is again a pure thermal heat conduction problem at *frozen configuration* $\boldsymbol{\varphi}$. However, problem $(ALGO_M)$ is *not* a pure mechanical problem since it is accompanied by a temperature change due to the thermoelastic heating effect. This class of thermomechanical coupling algorithm has been proposed by Armero & Simo [9] and proved to be absolutely stable.

4.6.2. Constitutive Update Algorithm at Frozen Temperature. Within the above isothermal predictor phase, we update the viscoplastic flow by means of a deformation–driven update algorithm. This algorithm computes for prescribed deformation the change of the internal variables within the time increment $[\,t_n,\, t_{n+1}\,]$ under consideration. These updates follow from the coupled system of local equations

$$\boldsymbol{r} := \begin{bmatrix} \partial_{\boldsymbol{\varepsilon}^p}\hat{\Psi}(\boldsymbol{\varepsilon}, \boldsymbol{\varepsilon}^p, \theta_n) + \boldsymbol{\sigma}^p \\ \boldsymbol{\varepsilon}^p - \boldsymbol{\varepsilon}_n^p - (\gamma^p - \gamma_n^p)\mathrm{dev}[\boldsymbol{\sigma}^p]/|\,\mathrm{dev}[\boldsymbol{\sigma}^p]\,| \\ \gamma^p - \gamma_n^p - \Delta t\dot{\gamma}_o \exp[\,-(A\,s/\theta_n)(\,1 - \{\,|\,\mathrm{dev}[\boldsymbol{\sigma}^p]\,|/s\sqrt{2}\,\}^{5/6}\,)\,] \\ s - s_n - h(1 - s/s_{ss})(\gamma^p - \gamma_n^p) \end{bmatrix} = \boldsymbol{0} \qquad (4.85)$$

The first equation is the definition of the driving force (4.15) at the current time. The sequent equation states a fully implicit backward Euler–type integration of the flow rule (4.16) The third equation contains the increment of the viscoplastic flow (4.59) in the time increment $[\,t_n,\, t_{n+1}\,]$. Finally, the last equation contains the implicit update to the evolution equation (4.56) for the softening variable. The system (4.85) determines for a deformation–driven scenario, i.e. for prescribed total logarithmic strain $\boldsymbol{\varepsilon}$ the dissipative variables

$$\mathfrak{q} := \{\, \boldsymbol{\sigma}^p, \boldsymbol{\varepsilon}^p, \gamma^p, s \,\} \qquad (4.86)$$

at the current time t_{n+1}. The nonlinear system (4.85) is linearized and solved by a local Newton algorithm

$$\mathfrak{q} \Leftarrow \mathfrak{q} - [\hat{\boldsymbol{A}}(\mathfrak{q})]^{-1}\hat{\boldsymbol{r}}(\mathfrak{q}) \quad \text{with} \quad \hat{\boldsymbol{A}} := \partial_{\mathfrak{q}}\hat{\boldsymbol{r}}(\mathfrak{q}) \qquad (4.87)$$

until convergence is achieved in the sense $|\hat{\boldsymbol{r}}(\mathfrak{q})| \leq tol$. For given dissipative variables, evaluation of the potential equation (4.14) gives the current stresses in the logarithmic strain space

$$\boldsymbol{\pi}^{algo} = \partial_{\boldsymbol{\varepsilon}}\hat{\Psi}(\boldsymbol{\varepsilon}, \boldsymbol{\varepsilon}^p, \theta_n) \qquad (4.88)$$

The sensitivity of these stresses with respect to increments of the total logarithmic strains

$$\Delta\boldsymbol{\pi}^{algo} = \mathbb{c}^{algo} : \Delta\boldsymbol{\varepsilon} \qquad (4.89)$$

defines the *tangent moduli* consistent with the algorithm (4.85) in the logarithmic space. With the above outlined linearization of the constitutive algorithm at hand, this tangent operator assumes the closed form representation

$$\mathfrak{c}^{algo} = \partial^2_{\boldsymbol{\varepsilon}\boldsymbol{\varepsilon}}\hat{\Psi} - \begin{bmatrix} \partial^2_{\boldsymbol{\varepsilon}\boldsymbol{\varepsilon}^p}\hat{\Psi} \\ \boldsymbol{0} \\ 0 \\ 0 \end{bmatrix}^T \hat{\boldsymbol{A}}^{-1} \begin{bmatrix} \partial^2_{\boldsymbol{\varepsilon}^p\boldsymbol{\varepsilon}}\hat{\Psi} \\ \boldsymbol{0} \\ 0 \\ 0 \end{bmatrix} . \tag{4.90}$$

With the constitutive tangent moduli in the logarithmic strain space at hand, we compute the algorithmic nominal stresses $\boldsymbol{P}^{algo}$ and consistent nominal moduli $\mathbb{C}^{algo}$, governing the sensitivity

$$\Delta\boldsymbol{P}^{algo} = \mathbb{C}^{algo} : \Delta\boldsymbol{F} \ , \tag{4.91}$$

by a pure geometric post-processing. This is based on the geometric relationships (4.7), yielding the result

$$\boldsymbol{P}^{algo} = \boldsymbol{\pi}^{algo} : \mathbb{Q} \quad \text{and} \quad \mathbb{C}^{algo} = \mathbb{Q}^T : \mathfrak{c}^{algo} : \mathbb{Q} + \boldsymbol{\pi}^{algo} : \mathbb{L} \ . \tag{4.92}$$

with the current transformation tensors $\mathbb{Q}$ and $\mathbb{L}$ defined in (4.8). The algorithmic stress expression $\boldsymbol{P}^{algo}$ enters the isothermal deformation predictor (4.82). Finally, we compute for the updated dissipative variables $\boldsymbol{\sigma}^p$ and γ^p the algorithmic expression for the plastic dissipation (4.18), yielding the source

$$\mathcal{D}^{algo}_{loc} = |\operatorname{dev}[\boldsymbol{\sigma}^p]|\,(\gamma^p - \gamma^p_n)/\Delta t \geq 0 \tag{4.93}$$

in the heat conduction corrector (4.84).

4.6.3. Algorithmic Linearization for Global Newton Solver. With regard to the application of Newton-type solvers we consider the linearization of the two sub–algorithms $ALGO_M$ and $ALGO_T$ outlined above.

Mechanical Predictor. In order to obtain the linearization of the isothermal deformation predictor (4.82), we write the linear increment of the first Piola stresses at frozen temperature θ_n in the form $\Delta\boldsymbol{P}^{algo} = \mathbb{C}^{algo} : \nabla_X\Delta\boldsymbol{\varphi}$. Here $\boldsymbol{P}^{algo}$ and $\mathbb{C}^{algo}$ denote the algorithmic expressions for the nominal stresses and moduli obtained from (4.92) at frozen temperature θ_n. Here, $\nabla_X\Delta\boldsymbol{\varphi}$ denotes the material gradient of an incremental displacement field $\Delta\boldsymbol{\varphi}$ defined on the reference configuration. We then obtain the linear increment of the weak form (4.82)

$$\Delta\hat{G}_M(\delta\boldsymbol{\varphi}, \Delta\boldsymbol{\varphi}, \boldsymbol{\varphi}) := \int_{\mathcal{B}} \nabla_X\delta\boldsymbol{\varphi} : \hat{\mathbb{C}}^{algo}(\nabla_X\boldsymbol{\varphi}; \mathfrak{q}_n, \theta_n) : \nabla_X\Delta\boldsymbol{\varphi}\, dV \ , \tag{4.94}$$

in a straightforward manner characterized by the material tangent term. With this expression at hand, the condition on the linearization of the isothermal deformation predictor algorithm (4.82)

$$\hat{G}^{lin}_M(\delta\boldsymbol{\varphi}, \Delta\boldsymbol{\varphi}, \boldsymbol{\varphi}) := \hat{G}_M(\delta\boldsymbol{\varphi}, \boldsymbol{\varphi}) + \Delta\hat{G}_M(\delta\boldsymbol{\varphi}, \Delta\boldsymbol{\varphi}, \boldsymbol{\varphi}) = 0 \tag{4.95}$$

determines at given deformation $\boldsymbol{\varphi}$ its linear increment $\Delta\boldsymbol{\varphi}$ in a typical Newton–type iterative solution step.

Thermal Corrector. The linear increment of the heat-conduction corrector (4.84) reads

$$\Delta\hat{G}_T(\delta\theta, \Delta\theta, \theta) := \int_{\mathcal{B}} \{\, \delta\theta \frac{c}{\Delta t}\, \Delta\theta + \nabla_X \delta\theta \cdot k\boldsymbol{C}^{-1} \nabla_X \Delta\theta \,\} dV \tag{4.96}$$

for constant heat capacity c and conductivity k. Then, the condition on the linearization of the heat conduction corrector algorithm (4.84)

$$\hat{G}_T^{lin}(\delta\theta, \Delta\theta, \theta) := \hat{G}_T(\delta\theta, \theta) + \Delta\hat{G}_T(\delta\theta, \Delta\theta, \theta) = 0 \tag{4.97}$$

determines at given temperature θ its linear increment $\Delta\theta$ in a typical Newton–type iterative solution step. For the model under consideration, the thermal algorithm is *linear*, providing the solution within one step.

4.6.4. Remarks on the Finite Element Discretization. The computational model of finite thermoplasticity is supplemented by the spatial discretization of the equations associated with the two sub–problems $Algo_M$ and $Algo_T$.

Mechanical Predictor. The deformation field is discretized on the domain $\mathcal{B}$ of the reference configuration in a standard manner by the shapes

$$\boldsymbol{\varphi}^h(\boldsymbol{X}) = \boldsymbol{N}_{\boldsymbol{\varphi}}(\boldsymbol{X})\boldsymbol{d}_{\boldsymbol{\varphi}} \qquad \text{and} \qquad \nabla_X \boldsymbol{\varphi}^h(\boldsymbol{X}) = \boldsymbol{B}_{\boldsymbol{\varphi}}(\boldsymbol{X})\boldsymbol{d}_{\boldsymbol{\varphi}}\ , \tag{4.98}$$

where $\boldsymbol{N}_{\boldsymbol{\varphi}}$ and $\boldsymbol{B}_{\boldsymbol{\varphi}}$ are finite element interpolation matrices and $\boldsymbol{d}_{\boldsymbol{\varphi}}$ the current nodal positions of a finite element mesh. Hence, the spatial discretization of the *isothermal deformation predictor* $ALGO_M$ in its linearized form (4.95) gives the global Newton–type cycle

$$\boldsymbol{d}_{\boldsymbol{\varphi}} \Leftarrow \boldsymbol{d}_{\boldsymbol{\varphi}} - [\boldsymbol{k}_{\boldsymbol{\varphi}\boldsymbol{\varphi}}]^{-1} \boldsymbol{r}_{\boldsymbol{\varphi}} \tag{4.99}$$

in terms of the mechanical residual and the tangent matrix

$$\boldsymbol{r}_{\boldsymbol{\varphi}} := \int_{\mathcal{B}} \boldsymbol{B}_{\boldsymbol{\varphi}}^T \boldsymbol{P}^{algo} dV \quad \text{and} \quad \boldsymbol{k}_{\boldsymbol{\varphi}\boldsymbol{\varphi}} := \int_{\mathcal{B}} \boldsymbol{B}_{\boldsymbol{\varphi}}^T \mathbb{C}^{algo} \boldsymbol{B}_{\boldsymbol{\varphi}} dV\ , \tag{4.100}$$

which is solved until convergence is achieved in the sense $|\boldsymbol{r}_{\boldsymbol{\varphi}}| \leq tol_{\boldsymbol{\varphi}}$.

Thermal Corrector. In full analogy to the above setting, we discretize the temperature field on the domain $\mathcal{B}$ of the reference configuration by the shapes

$$\theta^h = \boldsymbol{N}_\theta \boldsymbol{d}_{\boldsymbol{\theta}} \qquad \text{and} \qquad \nabla_X \theta^h = \boldsymbol{B}_{\boldsymbol{\theta}} \boldsymbol{d}_{\boldsymbol{\theta}} \tag{4.101}$$

in terms of interpolation matrices $\boldsymbol{N}_\theta$ and $\boldsymbol{B}_\theta$ and the current nodal temperatures $\boldsymbol{d}_\theta$ of a finite element mesh. The spatial discretization of the *heat conduction corrector* $ALGO_T$ in its linearized form (4.97) gives the iterative cycle

$$\boldsymbol{d}_\theta \Leftarrow \boldsymbol{d}_\theta - [\boldsymbol{k}_{\theta\theta}]^{-1} \boldsymbol{r}_\theta \tag{4.102}$$

in terms of the thermal finite element residual

$$\boldsymbol{r}_\theta := \int_{\mathcal{B}} \{\, \boldsymbol{N}_\theta^T (\frac{c}{\Delta t}(\theta - \theta_n) - \mathcal{D}_{loc}^{algo}) + \boldsymbol{B}_\theta^T \boldsymbol{Q} \,\} dV \tag{4.103}$$

and the tangent matrix

$$\boldsymbol{k}_{\theta\theta} := \int_{\mathcal{B}} \{\, \boldsymbol{N}_\theta^T \frac{c}{\Delta t} \boldsymbol{N}_\theta + \boldsymbol{B}_\theta^T k\boldsymbol{C}^{-1} \boldsymbol{B}_\theta \,\} dV\ , \tag{4.104}$$

which is solved until convergence is achieved $|\boldsymbol{r}_\theta| \leq tol_\theta$. It is convenient to use identical finite element meshes for both the mechanical as well as the thermal fields, which makes the transfer of coupling variables easy. The standard displacement finite element approach fails in the context of isochoric elastoplasticity due to the overconstrained pressure field. To circumvent these difficulties, several mixed finite element formulations have been proposed in the literature. We discretize the mechanical phase of the algorithmically decoupled staggered scheme outlined above with mean pressure–dilatation Q1P0 elements, see for example MIEHE [65] and references therein. The thermal phase can be discretized with standard displacement–type elements.

5. Numerical Examples

An important part of this work consists on the evaluation of the capacity of the previously presented constitutive models to resemble the real mechanical behavior of glassy polymers by comparing the results of the simulations with the isothermal experimental results shown in Chapters 2 and 3. The parameter identification and model validation of the constitutive law of visco-plasticity in the logarithmic strain space is presented here for each form of plastic flow $\dot{\gamma}_p$ introduced in Chapter 4.

5.1. Parameter Identification Methodology

Even though yield drop is observed for all glassy polymers (thermoplastics and thermosets) below their glass transition temperature, the magnitude of it differs substantially from one material to another. In Figures 1.4a and 1.4b a comparison between PC and PMMA is shown via isothermal uniaxial compression experiments, where care was taken in order to perform these tests at true strain rates that allow the dissipation to the surroundings of any heat generated during deformation, enforcing isothermal conditions. It can be seen that the amount of softening after yielding is affected by temperature and that it drastically changes from one material to another, being this not so marked for PC as it is for PMMA.

On the other side, Figures 1.4c and 1.4d present uniaxial experiments at true strain rates considered to be fast enough not to allow the dissipation of the generated heat to the surroundings, increasing the temperature of the polymer sample. The effect of this thermo-mechanical condition can be clearly seen for the case of PMMA (Figure 1.4d) in the form of a more pronounced softening caused by the additional temperature in the specimen. PC, opposite to PMMA, shows less temperature softening when deformed at higher true strain rates.

Due to the complexity presented by the large amount of experimental data from which material parameters are identified, here we propose the following methodology. *i*) Identify the material parameters for the presented constitutive models from isothermal experiments at three different temperatures by means of a constitutive driver (see Scheday [81]) for the loading cases of uniaxial compression and plane strain. *ii*) Identify the thermal parameters of the model by solving a boundary value problem simulating uniaxial compression experiments at higher true strain rates. *iii*) Boundary value problems resembling isothermal and thermomechanical inhomogeneous tension experiments in 3–D will be solved to further study the capabilites of the identified set of material parameters. See Arruda, Boyce & Jayachandran [11] and Dal [31] for the application of a similar method to PMMA.

5.2. Results Using the Double Kink Model

5.2.1. Isothermal Uniaxial Compression and Plane Strain Simulations. Simulations of the homogeneous compression experiments were performed using a so-called *constitutive driver*, which becomes very suitable to identify material parameters of constitutive models based on homogeneous experiments. This method results very effective since it does not require the solution of a boundary value problem, fastly displaying the modifications on the true stress-true strain diagram caused by a trial of new parameters. The use of true strain rates above $\dot{\epsilon} = -1 \cdot 10^{-3}\,\mathrm{s}^{-1}$ can induce a heat increase in the ma-

terial, yielding inhomogeneous temperature and stress distributions along the specimen as shown in Figure 5.11b. In (4.2) and (4.21) these thermal effects are accounted for in the so–called *non–local* or conductive dissipation inequality, which this *local* driver–based simulation is not able to incorporate. Due to this reason, in Chapter 5.3 a boundary value problem and not the mentioned algorithmic constitutive driver will be used to define the thermo–mechanical parameters.

Sensitivity Study. As it is well know for the case of glassy polymers, the parameter identification must be carried out via a trial-and-error procedure. This is due to the fact that the material parameters obtained under compression do not yield satisfactory results when applied to solve a BVP in 3–D under tension due to the inherent pressure dependency of the material. This means that a set of material parameters that accurately predicts the material behavior under tension eventually will have to be modified to obtain *fittings* that yield predictive results under both compression and tension. In this regard, assessing the sensitivity of the true stress–true strain diagram to a variation in every parameter is crucial in order to carry out this trial–and–error method as efficiently as possible. The result of such a sensitivity study is displayed in Figure 5.1. The curves were obtained by always altering one single parameter in a certain interval, where the upper boundary is given next to the bold line and the lower boundary next to the dashed line. Due to the different nature of the parameters, specific values are explicitely given in Figure 5.1 to give gidance on the amount that each parameter has to be varied in the trial-and-error process.

Simulation of Uniaxial Compression Tests. Isothermal simulations were carried out based on the uniaxial experimental data of Chapter 2.2.2 obtained under the rates $\dot{\epsilon} = -1 \cdot 10^{-3}$, $\dot{\epsilon} = -5 \cdot 10^{-4}$ and $\dot{\epsilon} = -1 \cdot 10^{-4}\,\mathrm{s}^{-1}$ at the temperatures $\theta = 23$, $\theta = 50$ and $\theta = 75°\mathrm{C}$. The corresponding simulations are presented in Figure 5.2 and 5.3 and the parameters identified and employed in the simulations are shown in Table 5.1. From Figure 5.2 it is clearly seen that the capability of the model to capture the real material behavior diminishes when the temperature is increased, whereas by a temperature of $\theta = 75°\mathrm{C}$ the only part that can be accurately captured is the yield stress. At this temperature the model assumes the material to soften more than the material does in reality, becoming unable to predict the end of the strain softening. For the lowest true strain rate the model is unable to capture the rate dependency of the material, as seen for all temperatures in Figure 5.3. In Figures 1.4a and 1.4b it can be seen that polycarbonate describes a more complex post–yield mechanical response than PMMA, exhibiting a considerable drop in true strain and a marked hardening afterwards, complicating the fitting of the experimental data.

Table 5.1: Material Parameters Identified Isothermally

κ	[MPa]	2000	$\dot{\gamma}_0$	$[\mathrm{s}^{-1}]$	$6.243 \cdot 10^7$
μ	[MPa]	900	A	$[eV]$	140
μ_p	[MPa]	25.0	N_p	$[-]$	3.3
s_0	$[-]$	102	s_{ss}	$[-]$	68
h	$[-]$	340			

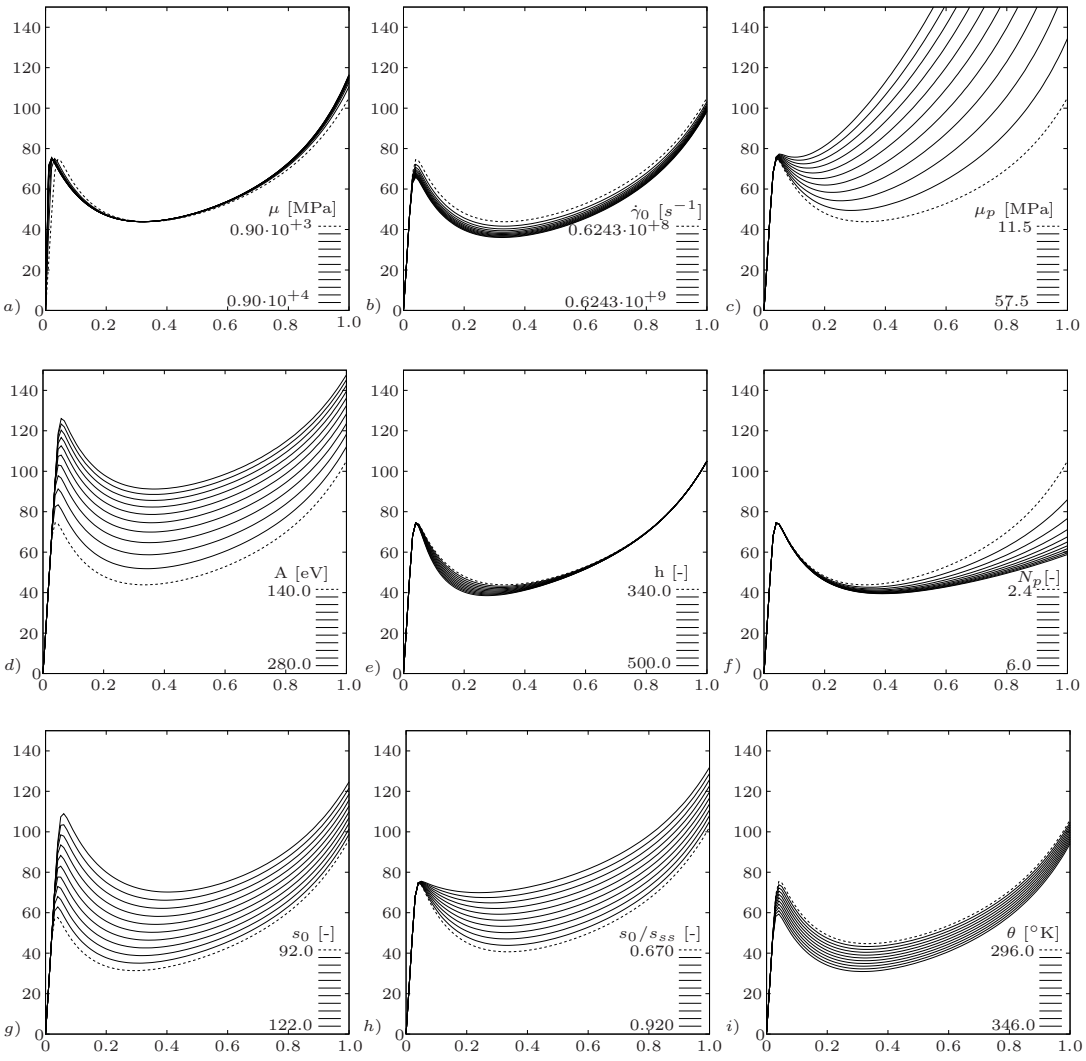

Figure 5.1: Sensitivity study of the material parameters appearing in the double kink theory.

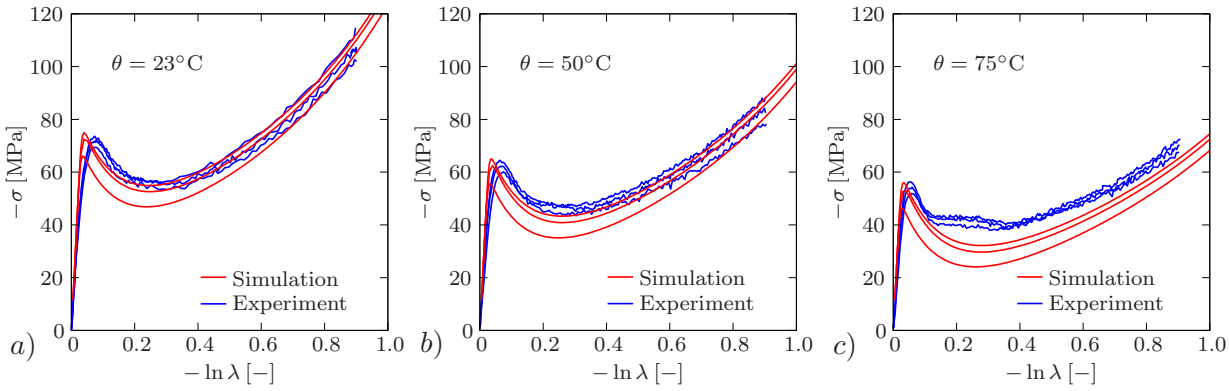

Figure 5.2: Isothermal uniaxial compression simulations compared with their corresponding experiments showing the true strain rate dependency of the model at the temperatures *a*) $\theta = 23°\text{C}$, *b*) $\theta = 50°\text{C}$ and *c*) $\theta = 75°\text{C}$.

Simulation of Plane Strain Tests. The constitutive driver was also applied to the case of the plane strain for which Figure 5.4 shows that the parameters of Table

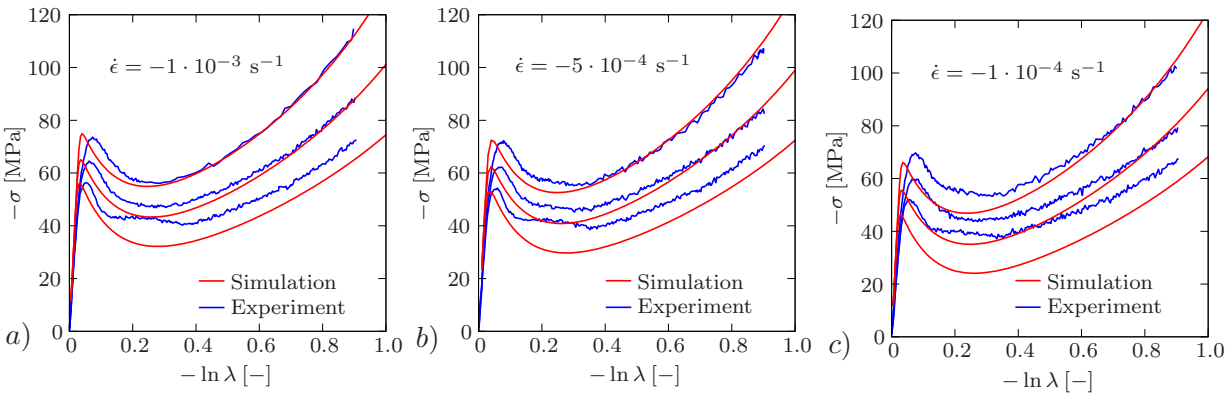

Figure 5.3: Same data as in Figure 5.2 showing the temperature dependency of the model under uniaxial compression at the true strain rates *a)* $\dot{\epsilon} = -1 \cdot 10^{-3}$, *b)* $\dot{\epsilon} = -5 \cdot 10^{-4}$ and *c)* $\dot{\epsilon} = -1 \cdot 10^{-4}$ s^{-1}.

5.1 can be applied to this deformation mode without further modification. The same predictive characteristics as observed for the case of uniaxial compression are observed for plane strain. The yield points are accurately captured despite the fact that plane strain experiments present considerably higher yield stresses than uniaxial compression. Under plane strain the material shows less strain–softening and more strain–hardening in the post–yield region causing that the plateau-like behavior in the post–yield after the end of the strain softening present in the experiments is missing in the simulations. This also induces that in Figure 5.5 the slopes of the hardening part of the experiments are overestimated by the model.

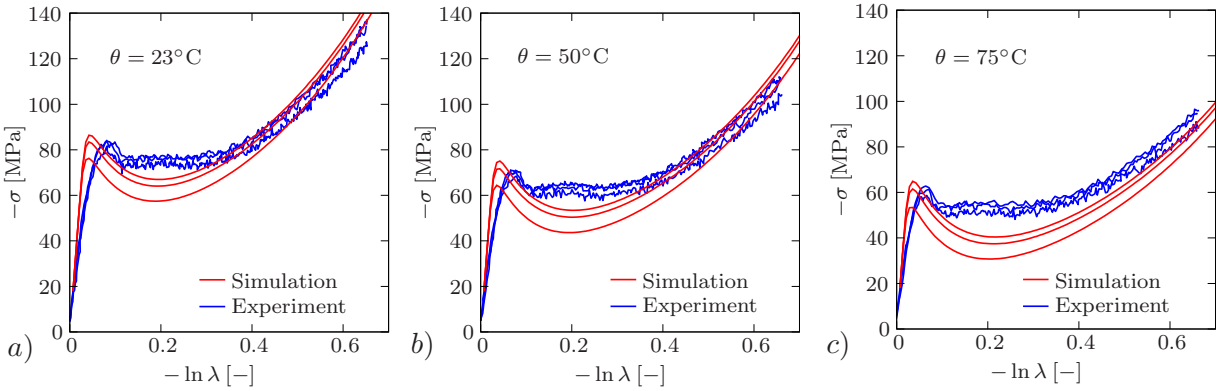

Figure 5.4: Isothermal plane strain compression simulations compared with their corresponding experiments showing the true strain rate dependency of the model at the temperatures *a)* $\theta = 23°$C *b)* $\theta = 50°$C and *c)* $\theta = 75°$C.

5.2.2. Simulation of Thermo–Mechanical Compression Experiments. As described before, the driver routine can not include the deformation-induced nonlocal temperature evolution in the material, thus, the solution of a boundary value problem is needed to simulate the uniaxial compression experiments at higher true strain rates. The discretized cylindrical specimen is presented next.

Employed Boundary Value Problem. Figure 5.6 shows the cylindrical specimen discretized in 250 Q1P0 finite elements as well as the employed boundary conditions $\vartheta(z = 0, t) = \vartheta(z = l, t) = 0$ where $\vartheta = (\theta - \theta_0)$, keeping the upper and lower surfaces

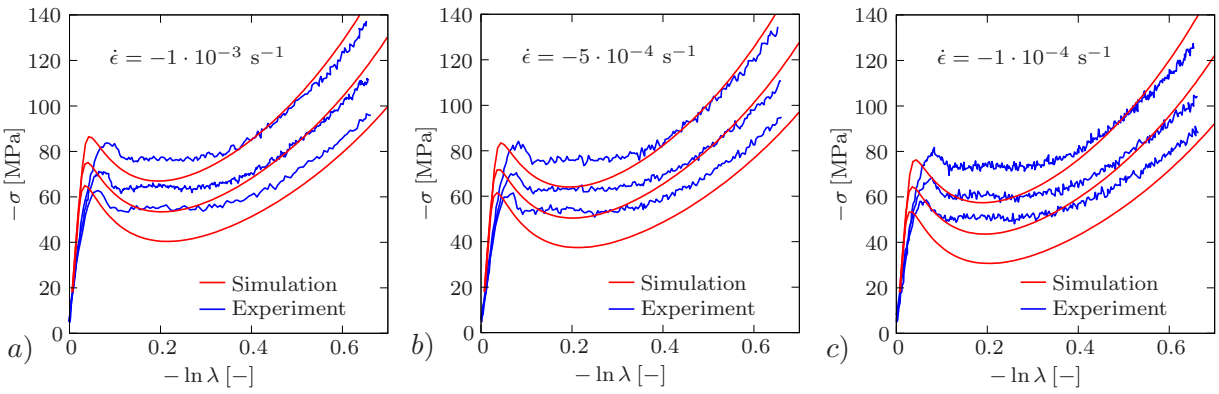

Figure 5.5: Same data as in Figure 5.4 showing the temperature dependency of the model under plane strain at the true strain rates *a)* $\dot{\epsilon} = -1 \cdot 10^{-3}$, *b)* $\dot{\epsilon} = -5 \cdot 10^{-4}$ and *c)* $\dot{\epsilon} = -1 \cdot 10^{-4}$ s^{-1}.

of the cylinder adiabatic. Additionally, the cylindrical surface is thermally insulated, i.e. the outward heat flux is $h = \boldsymbol{q} \cdot \boldsymbol{n} = 0$, which for the true strain rates $\dot{\epsilon} = -1 \cdot 10^{-1}$ and $\dot{\epsilon} = -1 \cdot 10^{-2}$ s^{-1} results appropriate. Similarly to the experiments, one face of the cylinder was displaced by a prescribed exponential loading function $u_z = u(t)$, approximated by 100 linear segments. For the included temperature field, the thermo–mechanical material

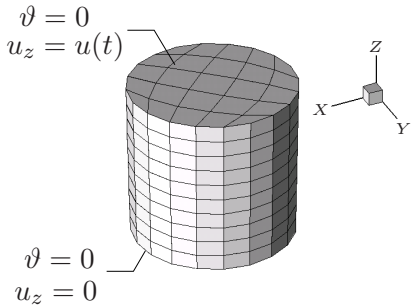

Figure 5.6: Cylindrical specimen discretized in 250–Q1P0 finite elements with mechanical and thermal boundary conditions.

parameters heat capacity c, thermal conductivity k and thermal expansion coefficient α were introduced. The heat capacity c is the ability of a material to absorb heat, i.e. it is a measure of how much heat is needed to raise the temperature of one gram of that material by one degree Celsius. The thermal conductivity k is a measure of the ability of a material to conduct heat. The thermal expansion coefficient α describes the elongation or contraction of a body as a result of a temperature change. See Godovsky [37] for more insight on these thermomechanical material properties.

Sensitivity Study. A sensitivity study for the thermo–mechanical material parameters is not as simple and fast to conduct as it is for the isothermal part of the material response. As mentioned before, the non-local nature of the temperature evolution requires the solution of a boundary value problem which is a more time–demanding task due to the longer time required to solve it. Additionally the influence of each thermo–mechanical parameter at each true strain rate has to be examined since mechanical material parameters like the elastic shear modulus μ or the chain density n_p are adjusted by the temperature evolution caused by deformation, which at the same time depends on the thermo–mechanical parameters.

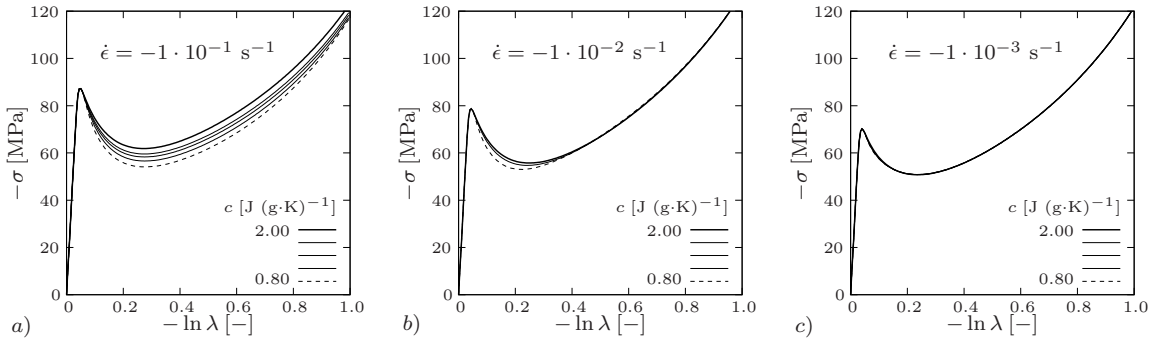

Figure 5.7: Effect of the heat capacity c on the true strain–true stress diagram for the true strain rates *a)* $\dot\epsilon = -1 \cdot 10^{-1}$ s^{-1}, *b)* $\dot\epsilon = -1 \cdot 10^{-2}$ s^{-1} and *c)* $\dot\epsilon = -1 \cdot 10^{-3}$ s^{-1}.

Figure 5.7 shows the influence of the heat capacity c on the simulated material response. Defined in (4.25), c enters the formulation in (4.104) as part of the heat capacity matrix. It can be observed that c influences almost the whole post yield behavior of the true strain-true stress diagram for the highest rate and shows no influence at the lowest. The latter complies with the fact that deformations carried out under isothermal conditions should not be influenced by thermal parameters. In Figure 5.8 the sensitivity study

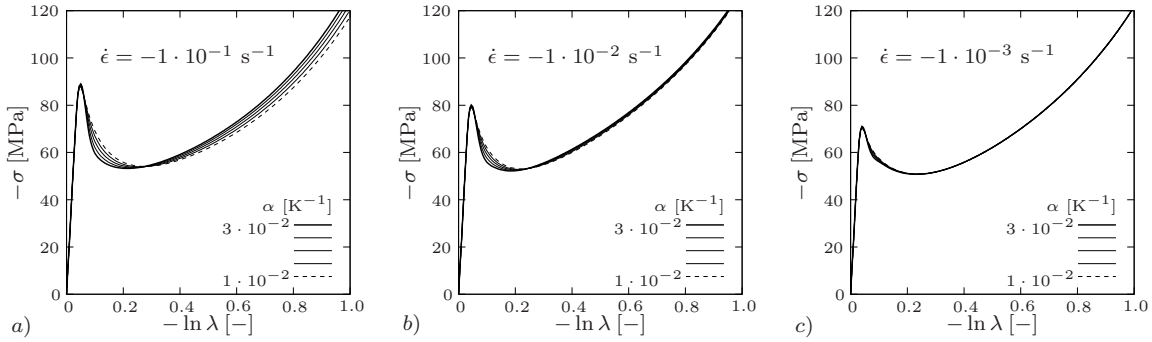

Figure 5.8: Effect of the thermal expansion coefficient α on the true strain–true stress diagram for the true strain rates *a)* $\dot\epsilon = -1{\cdot}10^{-1}$ s^{-1}, *b)* $\dot\epsilon = -1{\cdot}10^{-2}$ s^{-1} and *c)* $\dot\epsilon = -1{\cdot}10^{-3}$ s^{-1}.

for the thermal expansion coefficient α is shown. α acts as a *weight factor* of the temperature increment ϑ inside the thermoelastic coupling term in (4.38), which is a negative contribution to the total stresses. Finally, the sensitivity of the mechanical response to

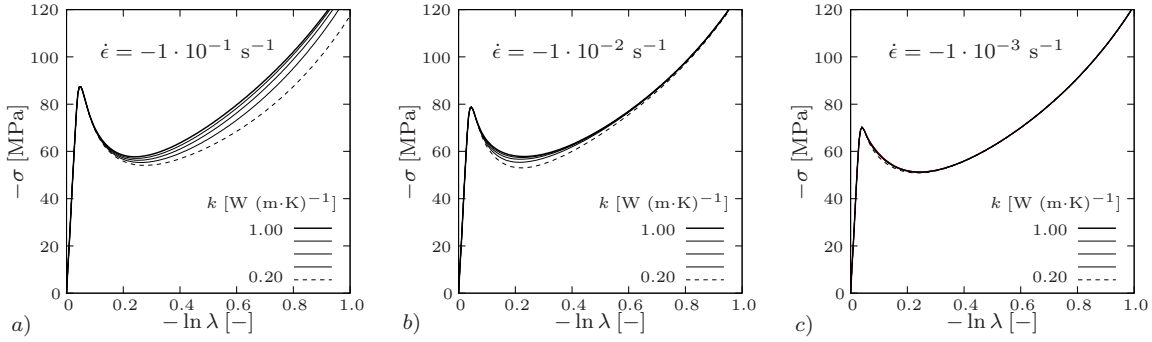

Figure 5.9: Effect of the thermal conductivity k on the true strain–true stress diagram for the true strain rates *a)* $\dot\epsilon = -1 \cdot 10^{-1}$ s^{-1}, *b)* $\dot\epsilon = -1 \cdot 10^{-2}$ s^{-1} and *c)* $\dot\epsilon = -1 \cdot 10^{-3}$ s^{-1}.

the conductivity k, entering the formulation via the heat flux equation (4.20) and later

becoming part of the conductivity matrix in (4.104), is displayed in Figure 5.9. For the highest rate the deformation is applied so abruptly that the conduction starts to take place at higher true strain values, whereas for the intermediate rate the effect is already seen at the end of the softening region. None of the thermo–mechanical parameters influenced the yield point. Based on the insensibility presented by the model to these three material parameters at the true strain rate $\dot{\epsilon} = -1 \cdot 10^{-3}$ s^{-1} (Figures 5.7c, 5.8c and 5.9c), this last rate will be considered as isothermal from this point on.

Parameter Identification and Results. The set of material parameters of Table 5.1 was further expanded by the identification of the thermo–mechanical parameters. This was done via a trial and error process where the sensitivity study was taken as guideline in order to carry out the identification process as efficiently as possible. The non–isothermal true strain rates $\dot{\epsilon} = -1 \cdot 10^{-1}$ and $\dot{\epsilon} = -1 \cdot 10^{-2}$ s^{-1} were applied to perform additional uniaxial compression experiments whose results are shown in Figure 5.10. The highest rate yielded the best overall fittings while with the second obtained a better approximation of the yield point. The complete set with the three additional thermal parameters can be found in Table 5.2.

Table 5.2: Identified Thermo–Mechanical Material Parameters

κ	[MPa]	2000	$\dot{\gamma}_0$	[s^{-1}]	$6.243 \cdot 10^7$
μ	[MPa]	900	A	[eV]	140
μ_p	[MPa]	25.0	N_p	[–]	3.3
s_0	[–]	102	s_{ss}	[–]	68
h	[–]	340	c_v	[J g^{-1}K^{-1}]	1.1
k	[–]	0.300	α_T	[K^{-1}]	$1.0 \cdot 10^{-2}$

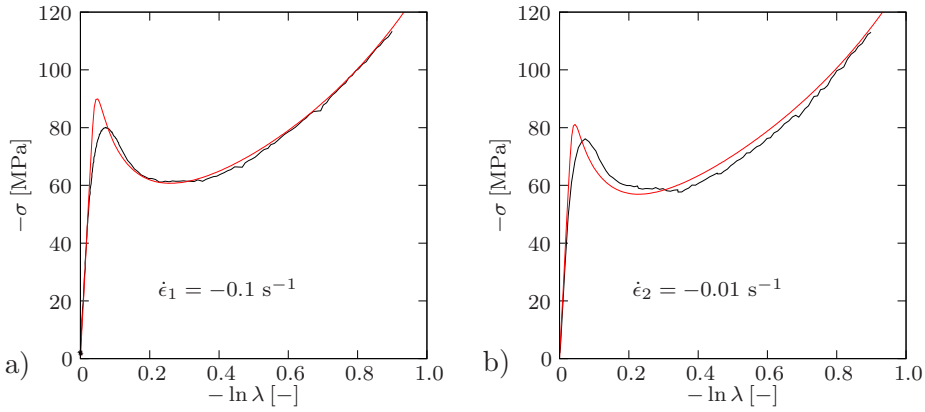

Figure 5.10: Plot of the thermo–mechanical experiments (black) and simulations (red) at room temperature for the true strain rates a) $\dot{\epsilon} = -0.1$ and b) $\dot{\epsilon} = -0.01$ s^{-1}.

In Figure 5.11 the contours of a real and a virtual pair of specimens deformed at the strain rate $\dot{\epsilon} = -1 \cdot 10^{-1}$ s^{-1} are compared, being the barreling of the sides clearly visible in both. The real specimen seems to be less compressed than the simulation due to the

fact that the real specimen was pictured once the experiment had finished and is therefore in an unloaded state, whereas the simulation has not yet released the elastic strains. In the next sub-chapter the origin of that inhomogeneous deformation will be studied in more detail.

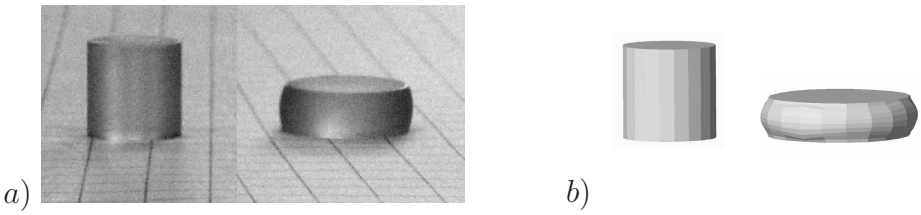

Figure 5.11: *a*) Pictures taken from a specimen in the undeformed and deformed state, the later under $\dot{\epsilon} = 1 \cdot 10^{-1}\text{s}^{-1}$. *b*) Results obtained from the simulations resembling the barreling observed in *b*) due to the inhomogeneous temperature distribution in the specimen.

Temperature Evolution in Compression. As observed in Figure 5.11 for both experiment and simulation, the strain distribution along the polymer cylinder is no longer homogeneous, and as it will be shown here, the deformation process is no longer isothermal. Despite the lack of own infrared experiments that would reveal the temperature increment on the surface of the specimens, we can deduce from the similarity of the final form of the real and simulated specimen that the same phenomenon causing the simulation to barrel can be ascribed also to the experiment. For this purpose the five points labeled *i*) – *v*) in Figure 5.12 were chosen on the true strain–true stress diagram to examine the simulations for the two higher true strain rates. *i*) shows the initial geometry of the specimen, *ii*) marks the yield point and *iii*) is at the lowest force during the strain softening. *iv*) is at the half of the displacement between *iii*) and the final *v*).

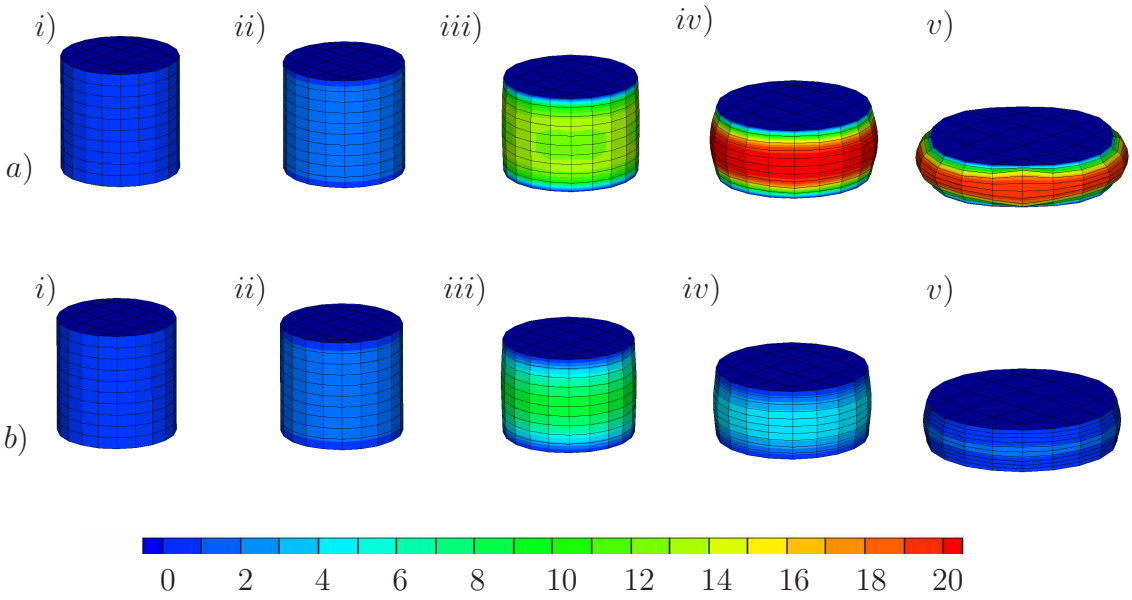

Figure 5.12: *a*) Temperature distribution of the simulation at the strain rate $\dot{\epsilon} = -1 \cdot 10^{-1}$ s^{-1}. *b*) Temperature distribution of the simulation at the strain rate $\dot{\epsilon} = -1 \cdot 10^{-2}$ s^{-1}.

By comparison of Figures 5.12a and 5.12b it can be seen that higher rates produce greater amount of heat specially for steps *iv*) and *v*), whereas the steps *i*)–*iii*) show almost

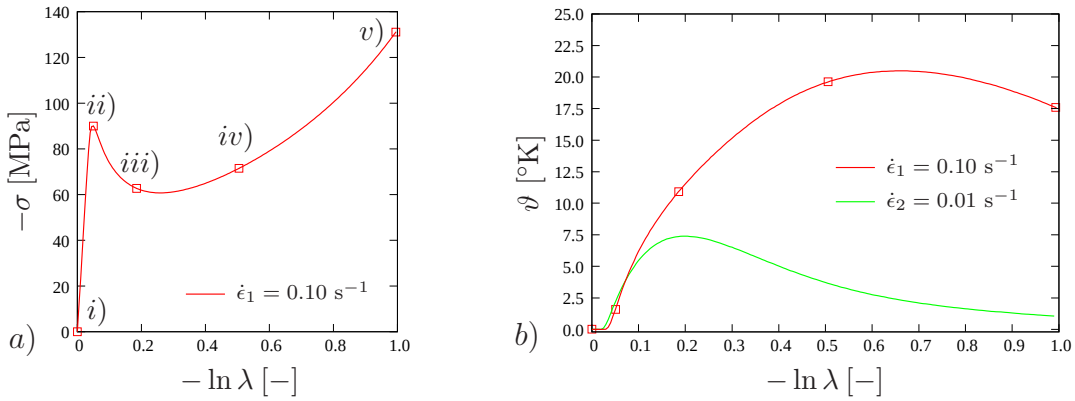

Figure 5.13: *a*) Identification of the points of interest for the temperature distibutions shown in Figure 5.12a. *b*) Temperature evolution over true strain for both rates obtained from a node located in the midpoint of the cylinder.

the same distribution for both rates. For the true strain rate of $\dot{\epsilon} = -1 \cdot 10^{-2}\ \mathrm{s}^{-1}$ the maximum temperature increase of 7.4°K is reached already in point *iii*), followed by cool down. For $\dot{\epsilon} = -1 \cdot 10^{-1}\ \mathrm{s}^{-1}$ the true strain-temperature diagram reaches its maximum at $\vartheta = 21.01$°K after point *iv*). It can be concluded that an inhomogeneous temperature distribution along the specimen causes different parts of it to soften differently, being the mid plane of the cylinder the most prone to flow plastically due to the higher temperature found in its vicinity. This is the origin of the barrel-like form observed in the cylinder after deformation.

5.2.3. Simulation of Inhomogeneous Tension Tests. For further validation of the identified parameter set, boundary value problems representing the inhomogeneous tension tests presented in Chapter 3.3 will be solved. For the simulation the specimen was discretized using 8–noded Q1P0 coupled brick elements. Due to apparent symmetry only one fourth of it was used for the computation. To resemble the fastening of the test piece in the testing machine one end of the boundary value problem was fully constrained while the other was drawn at the mentioned deformation rate, see Figure 5.14.

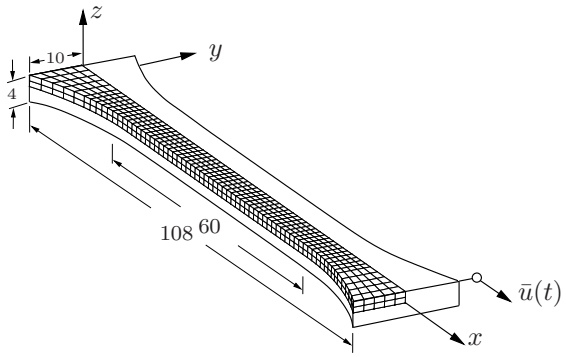

Figure 5.14: Dimensions of the dumbbell–shaped specimen for the tension boundary value problem. A quarter of the specimen is meshed with 660 Elements.

In Figure 5.15 the simulations of the experimental load-displacement diagrams are shown. The adaptivity of the constitutive model to isothermal tension gives a predictive match for the case of room temperature, whereas for the other two temperatures the results are acceptable up to the creep–like behavior, which is modeled too short, i.e. in

the simulations the displacement required for the neck front to reach the end of the gauged section of the flat specimen is shorter than in reality. Differently from the compressive simulations at 75°C, the temperature dependence in the load–displacement diagram under tension gives more satisfactory results along the creep-like plateau (compare to Figure 5.2c).

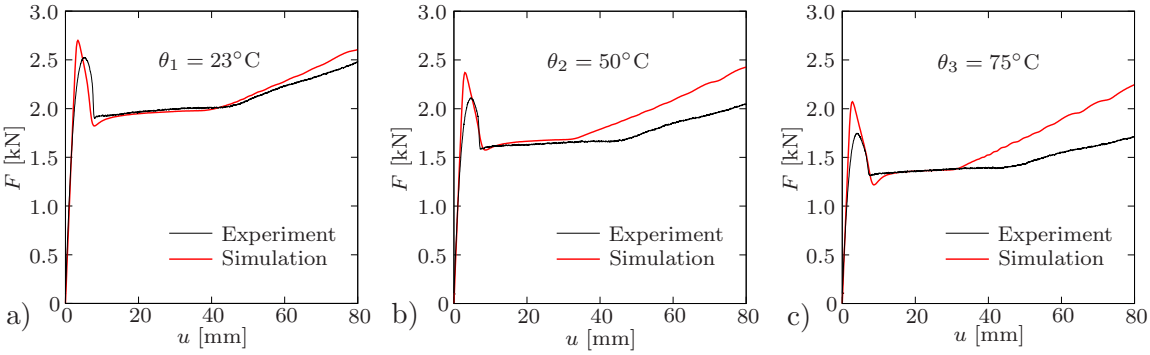

Figure 5.15: Simulation of the isothermal tension test performed with the displacement rate $\dot{u} = 2\text{mm/min}$. a) $\theta = 23°C$, b) $\theta = 50°C$ and c) $\theta = 75°C$.

As it has been mentioned before, the 3–D inhomogeneous experimental results serve as a *model validation* tool since they can be directly compared with the results of simulations. Figures 5.16–5.18 show the comparison of the major strain distributions obtained experimentally (right) with the results of the BVP (left) at the three employed temperatures. The deformation stages displayed correspond to the points marked in the load displacement diagram of Figure 3.6. Similarly of what was observed in Figure 5.15, it can be observed that the simulation is again in good agreement at room temperature reaching the maximum major strain over the whole length of the neck just as described by the experiments (see Figure 5.16f). For the two cases at higher temperatures, the BVP fails to obtain predictive results by only reaching a portion of the maximum major strain exhibited by the experiments along the necked region.

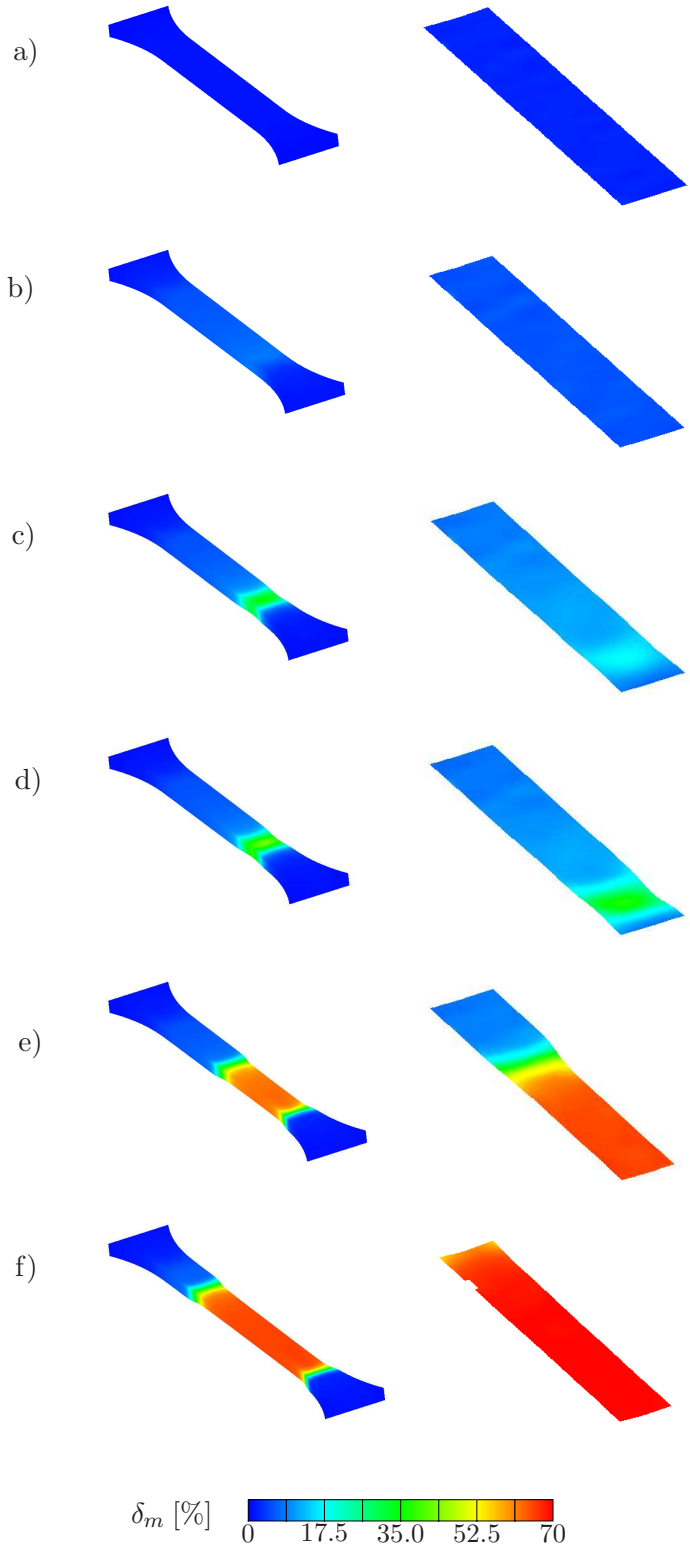

Figure 5.16: Major strain computations (left column) are compared with their corresponding inhomogeneous experimental results (right column) at 23°C. The labels of the rows *a*)–*f*) indicate the deformation stages labeled with the same letters in Figure 3.6. In the FE analysis, the same material parameters as those given in Table 5.1 have been used.

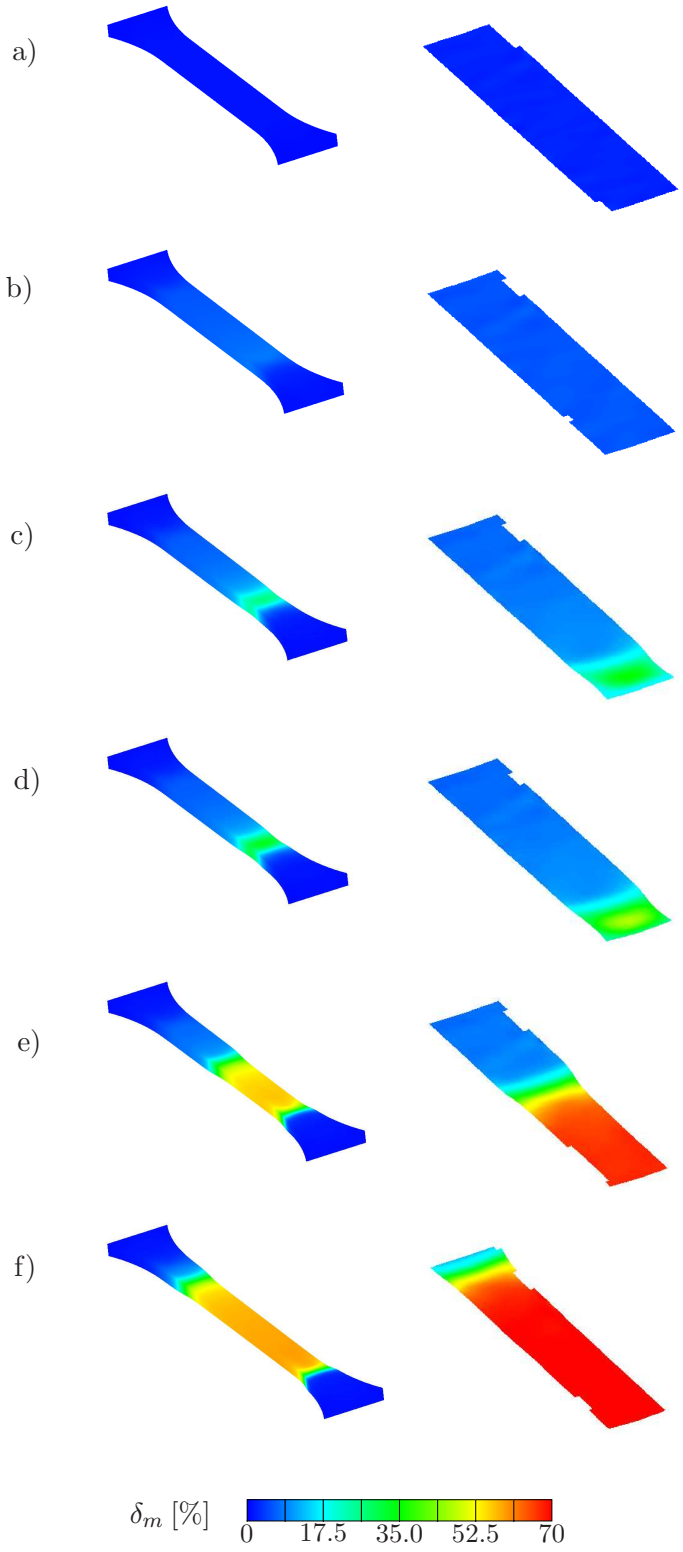

Figure 5.17: Major strain computations (left column) are compared with their corresponding inhomogeneous experimental results (right column) at 50°C. The labels of the rows *a*)–*f*) indicate the deformation stages labeled with the same letters in Figure 3.6. In the FE analysis, the same material parameters as those given in Table 5.1 have been used.

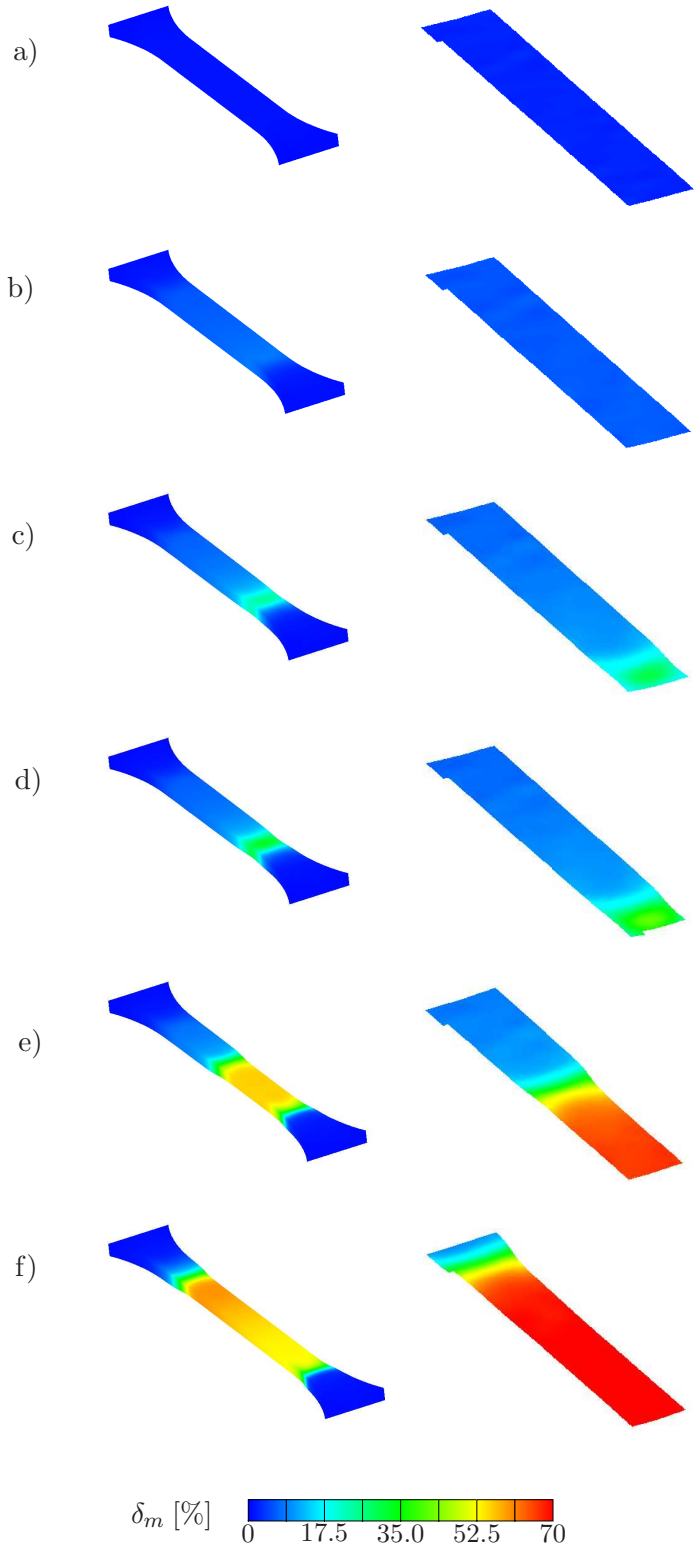

Figure 5.18: Major strain computations (left column) are compared with their corresponding inhomogeneous experimental results (right column) at 75°C. The labels of the rows *a*)–*f*) indicate the deformation stages labeled with the same letters in Figures 3.6. In the FE analysis, the same material parameters as those given in Table 5.1 have been used.

In order to further examine the capabilities of the proposed thermo–mechanical model for the non-isothermal case, an additional experimental load-displacement diagram was obtained at $\theta = 23°\text{C}$ using the deformation rate $\dot{u} = 50\text{mm/min}$, see Figure 5.19b. At this deformation rate the material is expected to undergo heating due to deformation, softening the material response. A simulation of this characteristics presents an additional difficulty in its execution since such a deformation can no longer be considered adiabatic because during the time required by the neck front to fully propagate along the gauged section of the specimen the already *necked* region begins to dissipate the generated heat to the surroundings. For this purpose, an additional material parameter, the *surface film coefficient* $\bar{h}$, had to be prescribed. It enters the formulation via the equation

$$\boldsymbol{q} \cdot \boldsymbol{n} = \bar{h}\ (\theta_{surface} - \theta_{ambient}), \tag{5.1}$$

where $\boldsymbol{q}$ denotes the Kirchhoff heat–flux and $\boldsymbol{n}$ the surface normal. We set this parameter to $\bar{h} = 0.01$. To get an overview of the quality of the simulations under tension with respect to the rate dependency, the tension plots for the two displacement rates at $\theta = 23°\text{C}$ are shown in Figure 5.19. In Figure 5.19b it can be observed that besides the overestimation of the yield point, the load-displacement diagram of the material is quantitatively captured by the model.

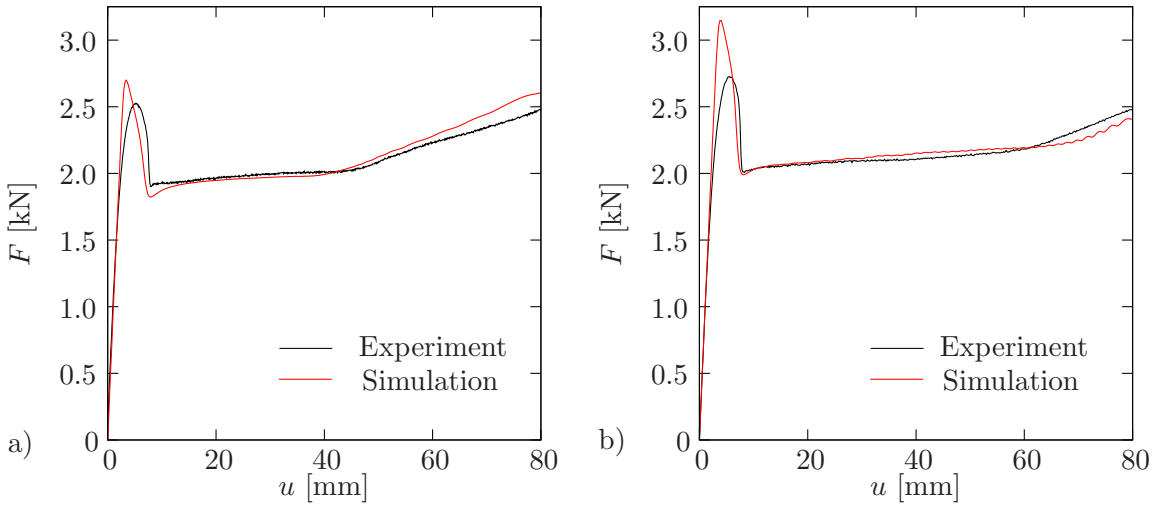

Figure 5.19: Comparison with experimental results of tension simulations using the material parameter set displayed in Table 5.2. at the crosshead speeds a) $\dot{u} = 2\text{mm/min}$ and b) $\dot{u} = 50\text{mm/min}$.

5.3. Results Using the Theory of Distributed Free Volume

So far in this work the predictive capabilities of the *double kink model* have been extensively studied. That constitutive law for the plastic flow showed to be well in accordance with experiments at room temperature but gave poor results when the temperature of the surroundings was increased. Besides, the theory lacks of a *smooth* elastic-to-inelastic transition, causing it to fail to predict in all simulations the strain at which yield occurs. In this subchapter the superior fitting capabilities of the theory of *distributed free volume* will be studied by carrying out similar simulations as those performed in Chapter 5.2, here done for the isothermal experiments only. To proceed with the validation of this model homogeneous uniaxial- and plane strain-compression experiments were employed to obtain the material parameters entering in this formulation. After, inhomogeneous tensile

experiments at the temperatures and *isothermal* deformation rate previously introduced were simulated using the same set of material parameters. This three–dimensional simulations were carried out by solving the boundary value problem of the discretized dumbbell specimen presented in Figure 5.14.

5.3.1. Isothermal Uniaxial Compression and Plane Strain Simulations. The material parameters, determined from the homogeneous uniaxial compression experiments shown in Chapter 2.2.2, are listed in Table 5.3. Once more the identification process was done via a *trial-and-error* procedure taking as a guide the sensitivity study shown in Figure 5.20, being N_p, α_0^{-1}, $\dot{\gamma}_0$, Δ_τ^*, Δ_p^*, and ω_0 the most relevant parameters to approximate the experimental curves.

Table 5.3: Identified Material Parameters

κ	[MPa]	2350	β_1	[−]	1.1×10^{-17}
μ	[MPa]	800	β_2	[−]	8.5
μ_p	[MPa]	17.8	β_3	[−]	30
N_p	[−]	3	$\dot{\gamma}_0$	[s^{-1}]	5×10^{10}
a_0	[eV]	1.47	Δv_τ^*	[mm^3]	3.55×10^{-18}
a_{eq}	[eV]	1	Δv_p^*	[mm^3]	2.3×10^{-19}
α_0^{-1}	[eV^{-1}]	0.032	ω_0	[s^{-1}]	4.2×10^{11}
α_{eq}^{-1}	[eV^{-1}]	0.94	ζ	[−]	90

Figures 5.21a–c show the simulation of the uniaxial compression data for all temperatures and true strain rates. It can be seen that this more elaborated model accurately captures the whole deformation up to the strain hardening. In Figures 5.21d–f a magnification of the true stress-true strain diagram up to the end of the strain softening is included to emphasize the predictive capabilities of the proposed model. Afterwards, the mechanical response is evaluated for plane strain compression in Figure 5.22, where a similar outstanding agreement between experiments and simulations is achieved in both yield and post yield regions.

5.3.2. Simulation of Inhomogeneous Tension Tests. The solution of the boundary value problem illustrated in Figure 5.14 was performed using the same set of material parameters listed in Table 5.3. The resulting load-displacement diagrams at different temperatures are plotted in Figure 5.23 where the in-situ experimental results together with the finite element simulations are presented. Comparison with the results of the optical measurement system, as done in Chapter 5.2.3 for the double kink model, are shown in Figures 5.24 to 5.29 for major strain distribution and thickness change. The latter magnitude was added in this subchapter in order to accentuate the remarkable results obtained in 3–D. The distributed free volume model applied to inhomogeneous deformations provides sound predictions of the neck initiation, stabilization and steady propagation along the gauged section of the specimen at all the employed temperatures.

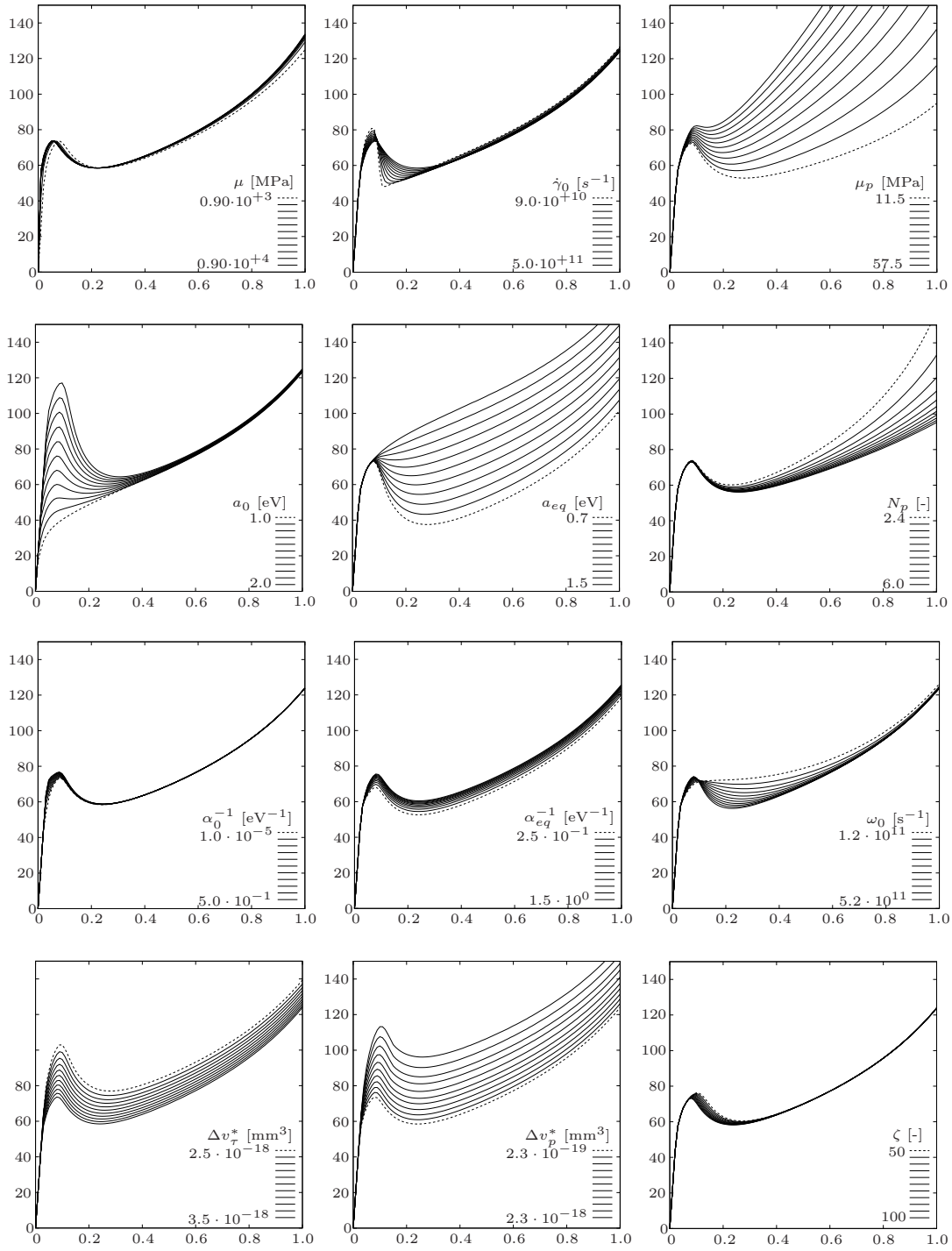

Figure 5.20: Sensitivity study of the most relevant material parameters appearing in the theory of distributed free volume.

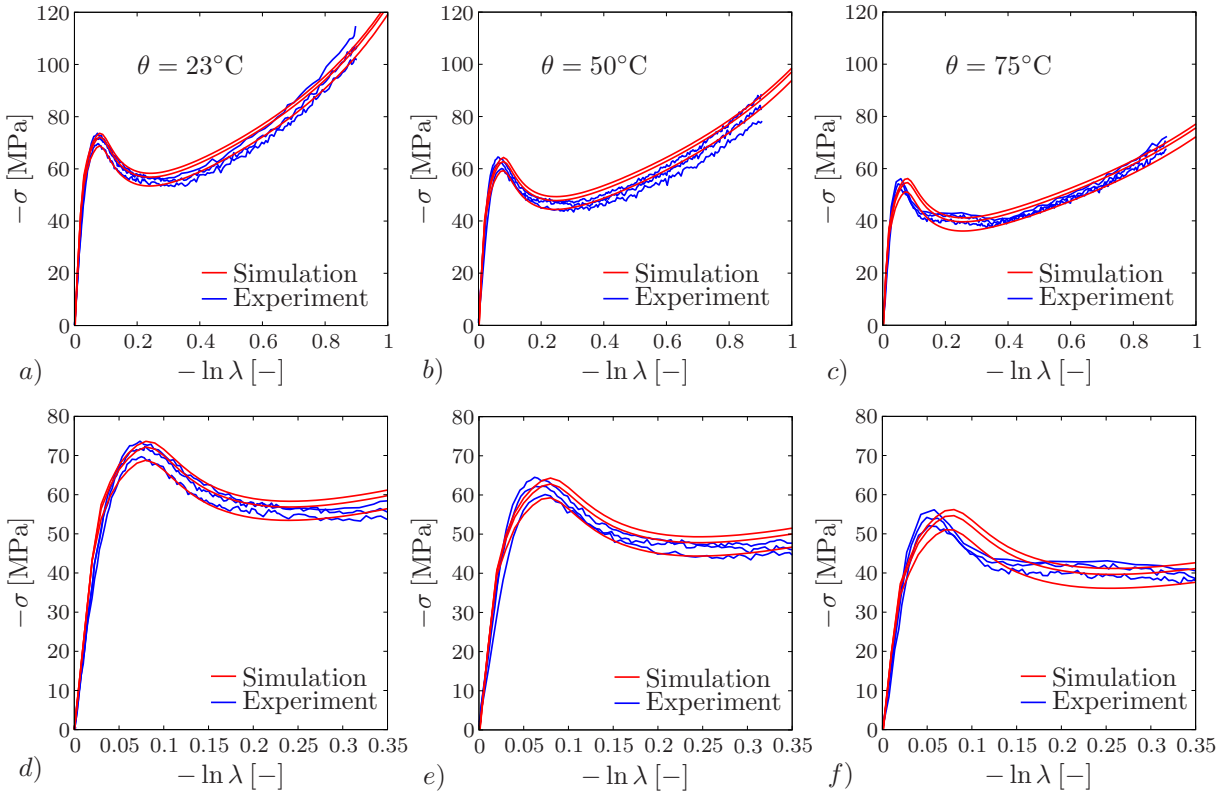

Figure 5.21: Curve fitting between uniaxial compression test data and the numerical simulation based on the constitutive model.

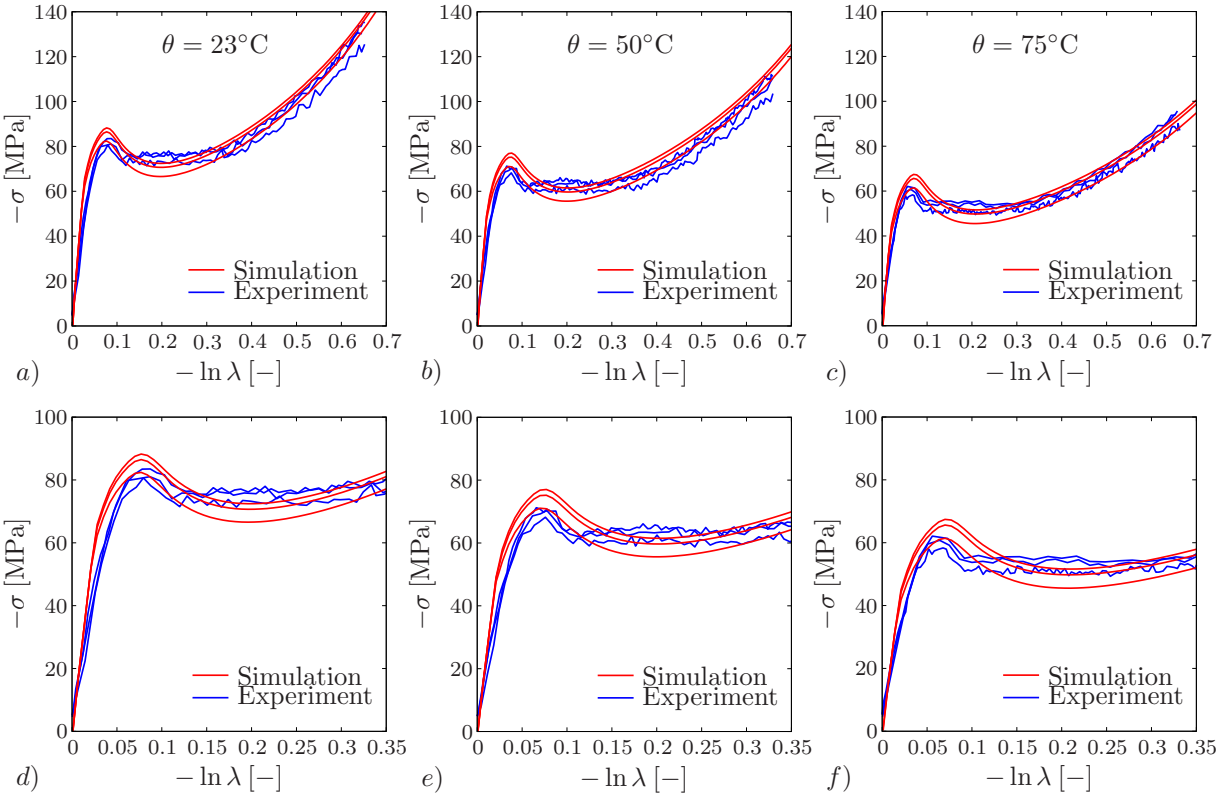

Figure 5.22: Curve fitting between plane strain compression test data and the numerical simulation based on the constitutive model.

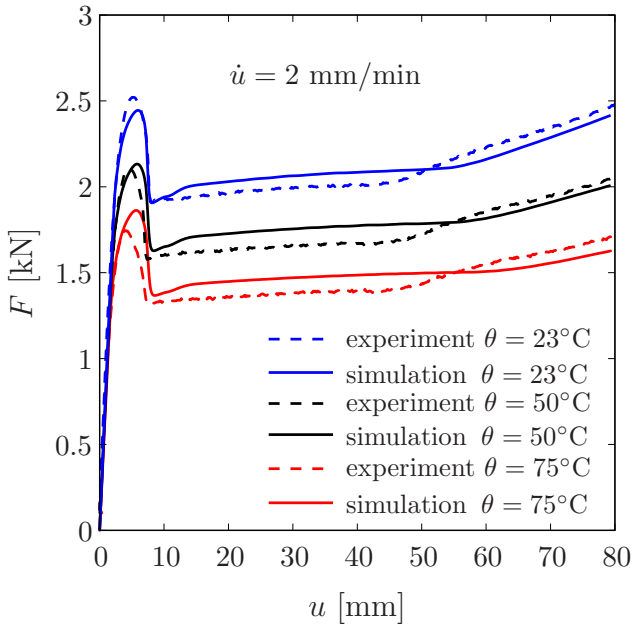

Figure 5.23: Comparison between the simulations and experimental data of cold-drawing at different temperatres.

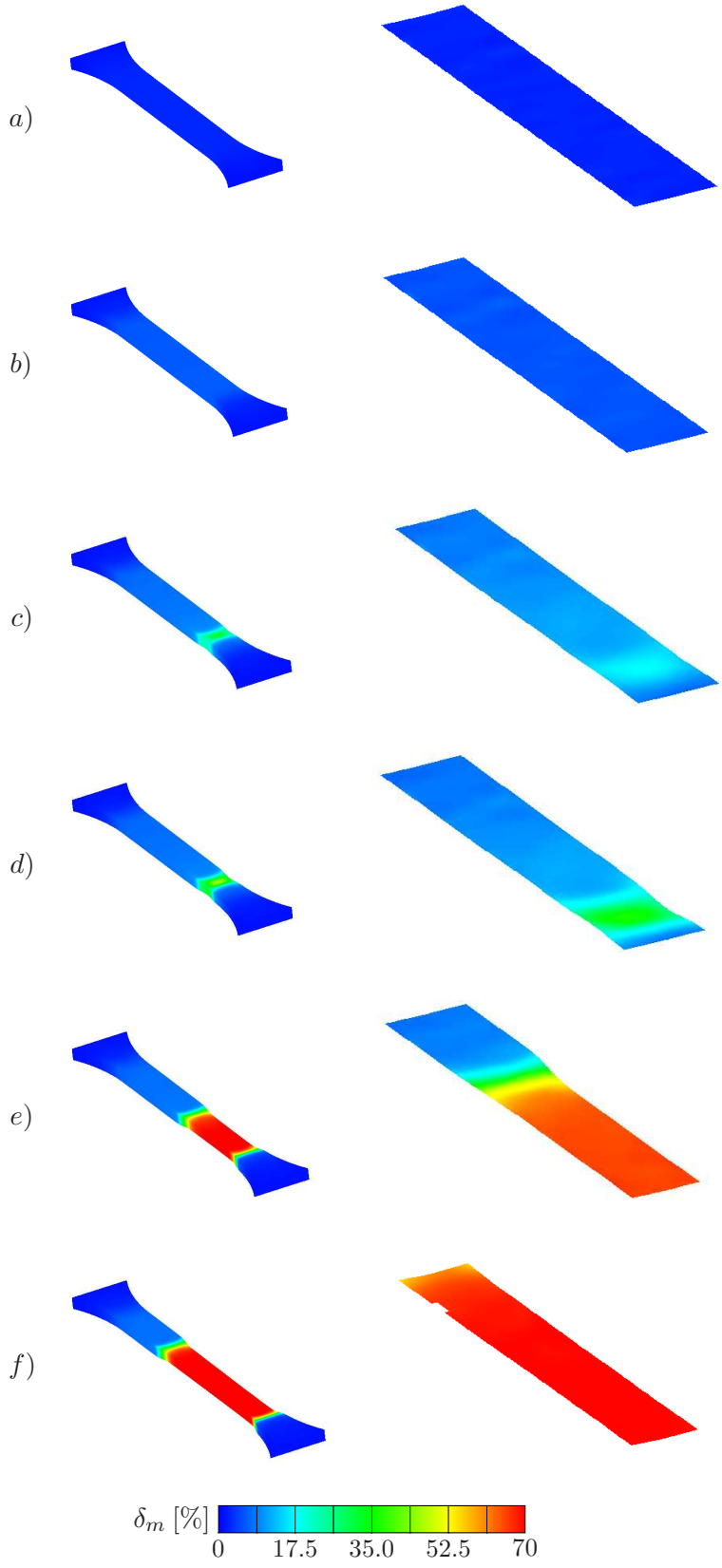

Figure 5.24: Major strain computations obtained by the three-dimensional finite element analysis (left column) are compared with their corresponding inhomogeneous experimental results (right column) at 23°C. The labels of the rows *a*)-*f*) indicate the deformation stages labeled with the same letters in Figure 3.6. In the FE analysis, the same material parameters as those given in Table 5.3 have been used.

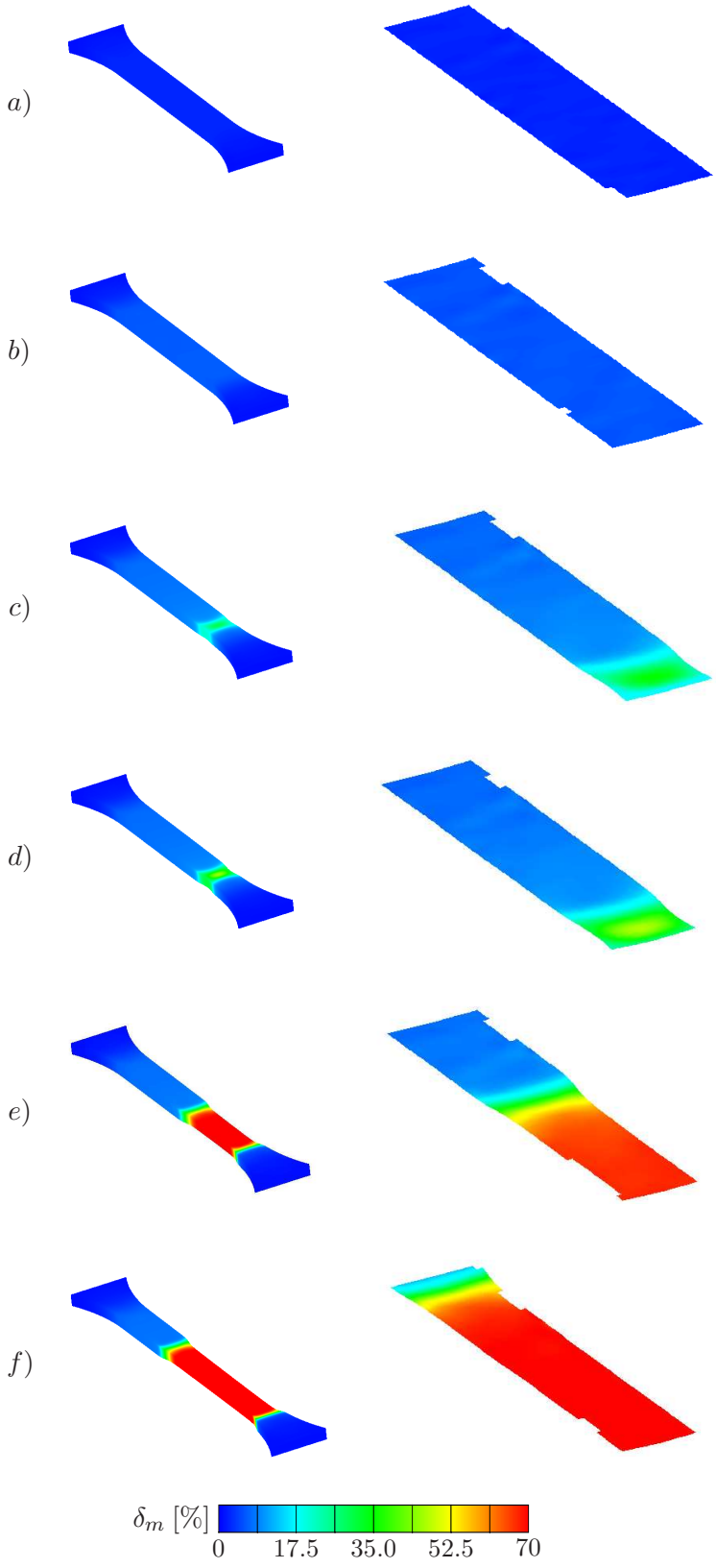

Figure 5.25: Major strain computations obtained by the three-dimensional finite element analysis (left column) are compared with their corresponding inhomogeneous experimental results (right column) at 50°C. The labels of the rows a)-f) indicate the deformation stages labeled with the same letters in Figure 3.6. In the FE analysis, the same material parameters as those given in Table 5.3 have been used.

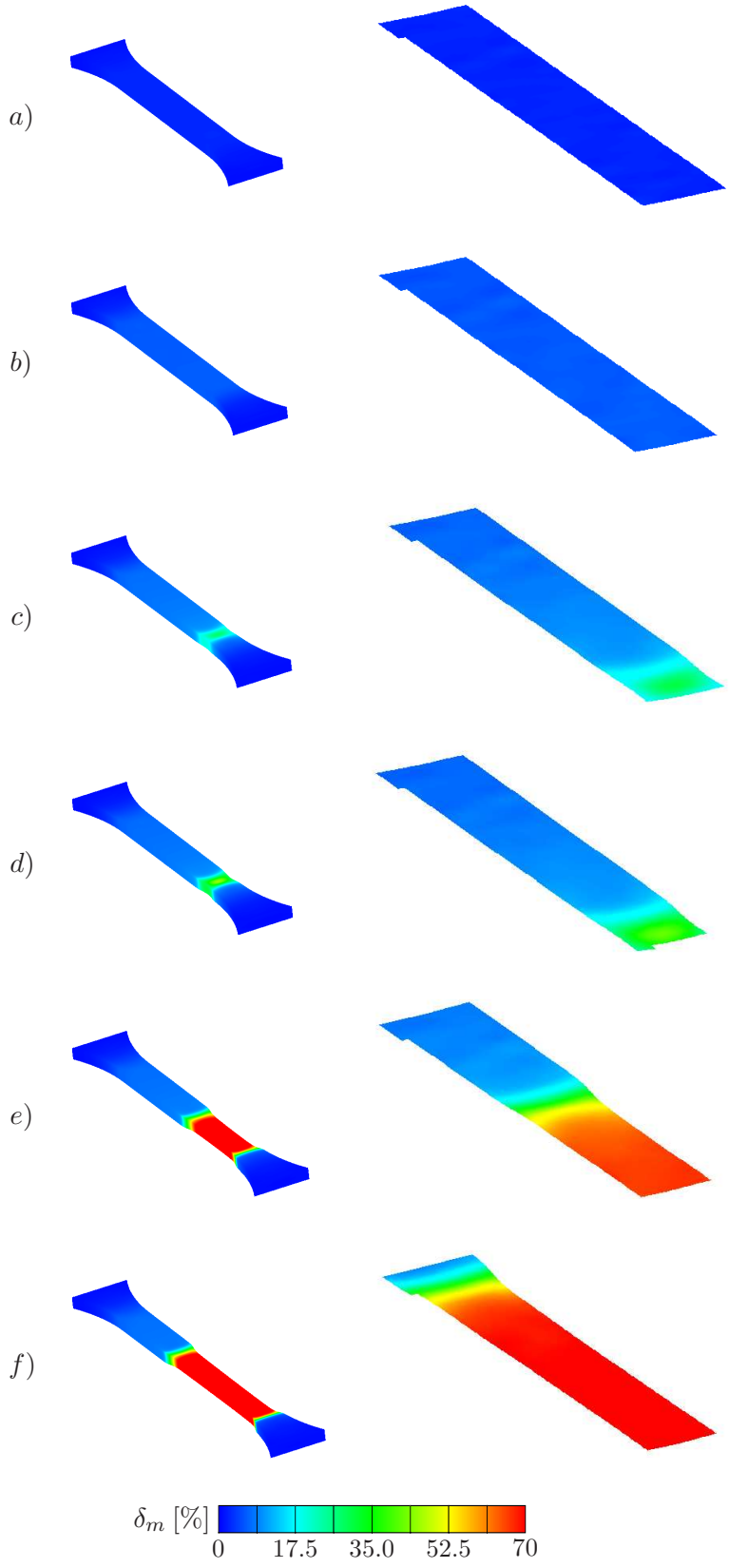

Figure 5.26: Major strain computations obtained by the three-dimensional finite element analysis (left column) are compared with their corresponding inhomogeneous experimental results (right column) at 75°C. The labels of the rows *a*)-*f*) indicate the deformation stages labeled with the same letters in Figure 3.6. In the FE analysis, the same material parameters as those given in Table 5.3 have been used.

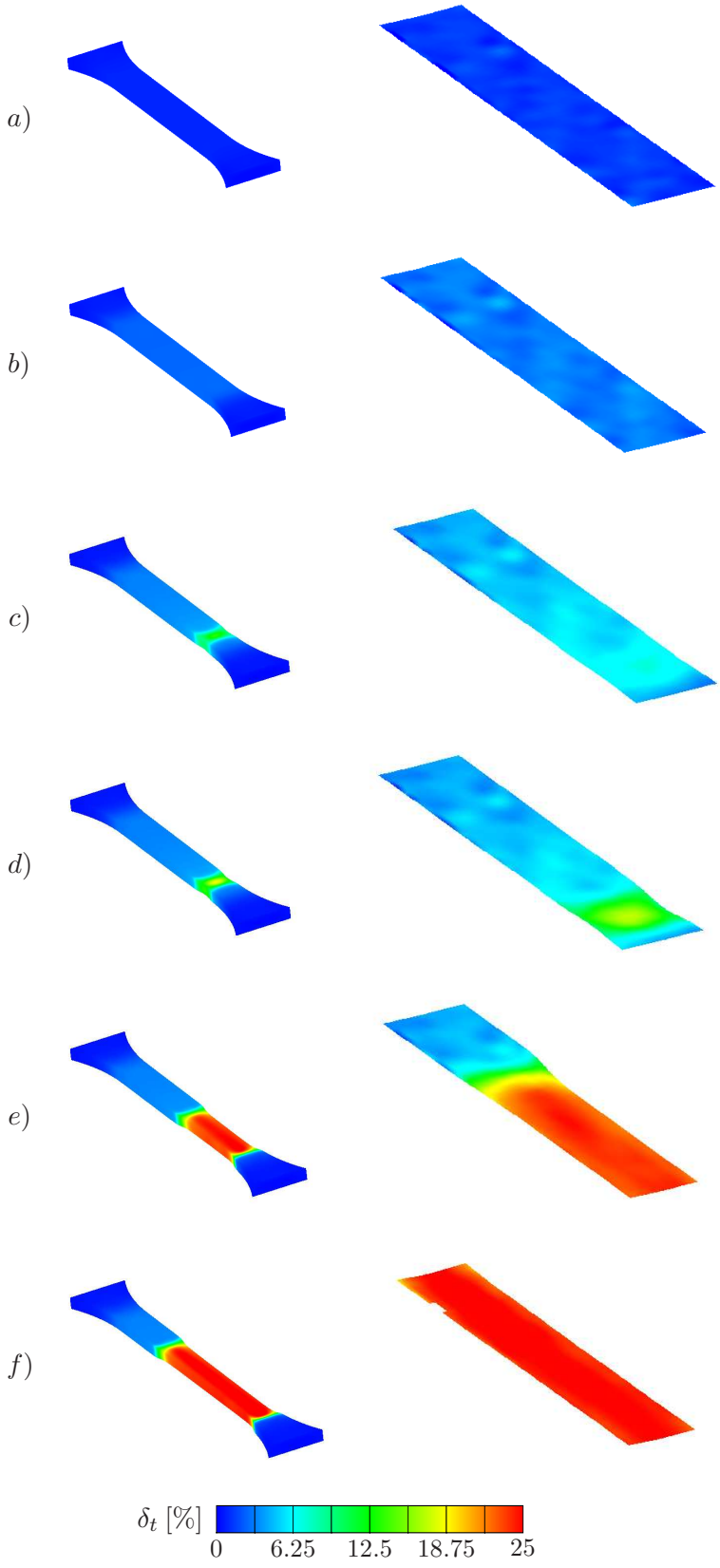

Figure 5.27: Thickness change computations obtained by the three-dimensional finite element analysis (left column) are compared with their corresponding inhomogeneous experimental results (right column) at 23°C. The labels of the rows *a*)-*f*) indicate the deformation stages labeled with the same letters in Figure 3.6. In the FE analysis, the same material parameters as those given in Table 5.3 have been used.

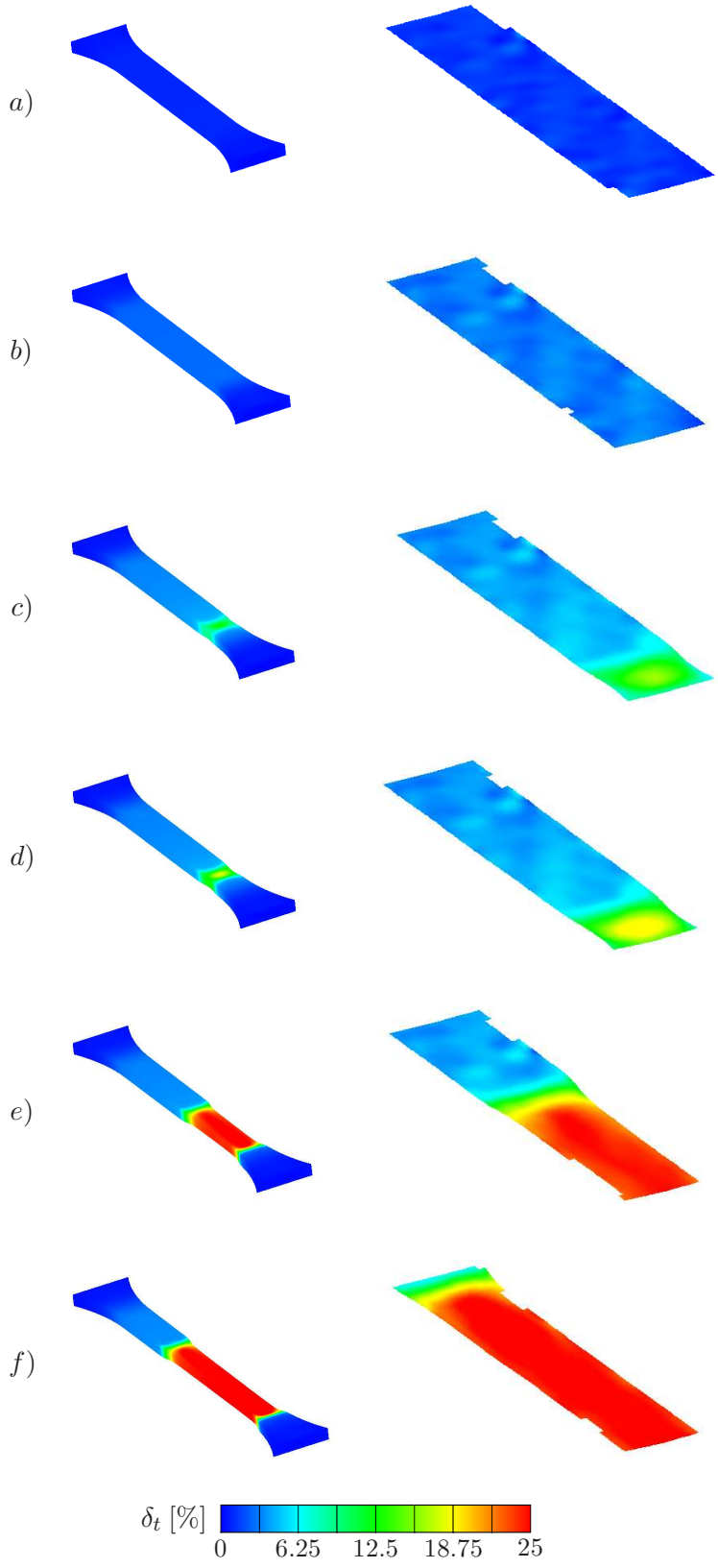

Figure 5.28: Thickness change computations obtained by the three-dimensional finite element analysis (left column) are compared with their corresponding inhomogeneous experimental results (right column) at 50°C. The labels of the rows *a*)-*f*) indicate the deformation stages labeled with the same letters in Figure 3.6. In the FE analysis, the same material parameters as those given in Table 5.3 have been used.

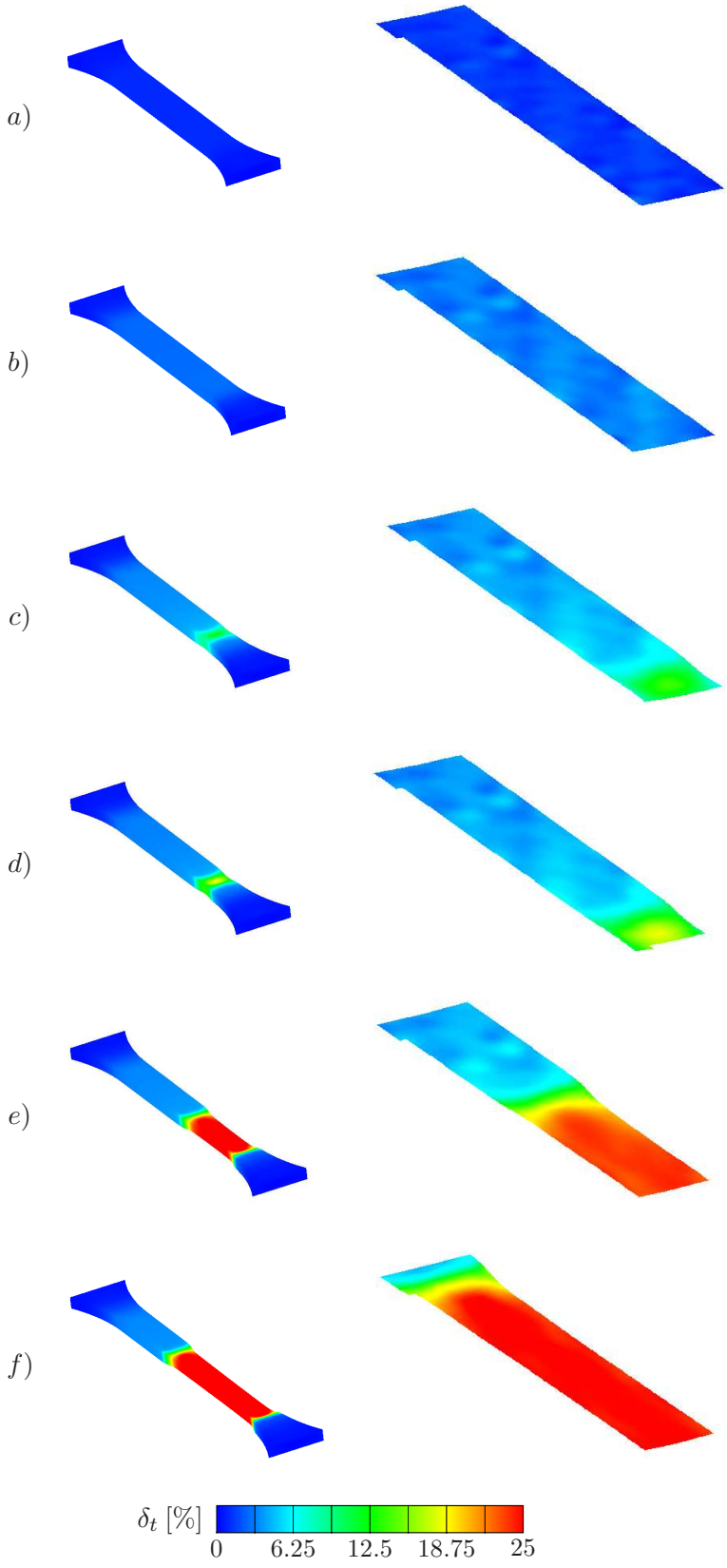

Figure 5.29: Thickness change computations obtained by the three-dimensional finite element analysis (left column) are compared with their corresponding inhomogeneous experimental results (right column) at 75°C. The labels of the rows *a*)-*f*) indicate the deformation stages labeled with the same letters in Figure 3.6. In the FE analysis, the same material parameters as those given in Table 5.3 have been used.

6. Concluding Remarks

This thesis is concerned with the conduction of experiments on glassy polymers that provide both, a reliable reference to identify the material parameters appearing inside different constitutive models and a validation of the capability of those models to simulate real material behavior. For this, a full understanding of the problem at hand together with a profound deliberation of the phenomena to be measured were crucial for the success of the experimental work. These experiments were implemented following strict guidelines since external factors like friction, environmental temperature or die alignment can severely affect the final results. The necessary tools to be equipped to the testing machine were designed and manufactured in the shop of our own material testing laboratory, allowing swift modifications to the testing methodology if required.

All the experiments presented in this work were done using a polycarbonate with the denomination Makrolon 2607 as test material. Initially, homogeneous compression experiments were carried out using true strain rates slow enough to isolate the pure mechanical response by excluding any deformation-generated heat. This was of special importance since most constitutive models are initially developed to acquaint for the purely mechanical response of the material, leaving for further development their thermo-mechanical extension. In order to subject the evaluated constitutive model to a more exhaustive scrutiny two different *homogeneous deformation modes*, namely uniaxial- and plane strain compression were considered. Additionally, these homogeneous tests were carried out at three true strain rates and three temperatures to study the adaptability of the material models. Cylindrical specimens were employed for the uniaxial compression experiments, being friction and misalignment of the upper and lower dies the most common source of inhomogeneity in the deformed specimens. This problem was tackled by the construction of a self-adjusting lower die having a spherical seat that allowed the upper and lower surfaces touching the material to *self-align*, providing two surfaces as parallel as possible to carry out the compression of the cylindrical specimen. With this, the presence of buckling in the experiment was almost eliminated. Friction was avoided up to a satisfactory degree by using a mixture of solid and liquid lubricants. For the case of plane strain homogeneous experiments cube-shaped specimens were used. In this case misalignment was not much of a problem as it was friction, which required additional countermeasures due to the larger contact area of the specimen with the surrounding die. This problem was minimized by a well documented standard procedure developed in this work which consisted on wrapping up the specimen in such a way that successive layers of solid and liquid lubricants were placed around the cubic specimen. We claim to have successfully carried out the mentioned homogeneous isothermal experiments based on the high repeatability observed when different data sets obtained under the same conditions are compared with each other. If the desired temperature failed to be induced to the specimen prior to the initiation of the experiment the repeatability would also be affected since polycarbonate, like most glassy polymers, present a high sensitivity of their mechanical behavior to even slight temperature changes.

Due to the typical inhomogeneity in the form of a neck that they present, when glassy polymers subjected to tension are studied using standard testing equipment, only load–displacement and not true stress-true strain diagrams can be obtained. In this work tensile experiments were carried out together with the 3–D optical measurement system ARAMIS, making possible the acquisition of the strain distribution present on the spec-

imen surface throughout the duration of the deformation. Specially challenging was the obtention of such inhomogeneous strain distributions when the experiments were performed inside an environmental chamber. Once again, a procedure had to be designed and put in place in order to calibrate the optical measurement system, get the appropriate illumination inside the chamber and apply the enamel required for the optical recognition of the surface. Since these experiments were meant to be later compared with simulations, the neck was required to initiate at a specific point along the gauged section of the experiment. The effect of the slight grinding done to nucleate the neck at a specific point and the compulsory spray coating on the dumbbell-shaped specimen were examined. They were observed to have no effect in the overall mechanical response of the material. The synchronization of the standard load-displacement diagram with the 3–D experimental results and the execution of this tests under different temperatures gave new light into the process of neck formation, stabilization and propagation in glassy polymers.

For the computational part of this work a recently developed kinematical setting of thermo-elasto-visco plasticity of glassy polymers in the logarithmic strain space was employed. This allowed us to use the well–established additive decomposition of the elastic strain variable in total and plastic parts similar to the geometrically linear theory. We begin by introducing the basic tensorial objects required in plastic metric thermoplasticity. Afterwards the general thermodynamical framework of coupled thermoviscoplasticity in presented, where the two balance equations governing the IBVP are solved by the construction of a *staggered* solution algorithm consisting of a mechanical predictor and a thermal corrector. Then, specific constitutive equations for the thermoelastic and plastic responses are given in the form of an additively decomposed free energy. The amount of plastic flow, entering the evolution equation for the plastic strains, is a critical point of the constitutive modeling. Two constitutive theories for the plastic flow were implemented and their fitting capabilities evaluated by comparison with the experimental data. As a first approach the micromechanically motivated double kink model was employed to simulate the isothermal and the thermomechanical compression data, from where the material parameters corresponding to this model were identified. The model showed good agreement with experiments at room temperature independently of the rate, but the quality of the approximations worsened as the temperature was increased. In addition, the inhomogeneous tension experiments were simulated by solving a BVP which showed the same tendency as the homogeneous compression experiments in regard to fittings. Alternatively, a more elaborated constitutive model based on the distributed free volume was employed to simulate the material behavior. For this case only the isothermal experimental results were used. The advantages of the distributed nature of this model were immediately recognized in the form of a smooth transition from elastic to inelastic behavior at the yield point. The rate and temperature dependency of the material were predictively captured for the compression as well as for the inhomogeneous cases. The optical measurement system established itself as a convenient tool for the study of the performance of constitutive laws applied to three dimensional simulations by allowing direct comparison between the real and the virtual results.

A. Derivation of the Backstress Tensor

We start from the constitutive equation for the backstresses $\boldsymbol{\pi}^p$ in the logarithmic space given in $(4.35)_3$

$$\boldsymbol{\pi}^p := \frac{\hat{\Psi}^p(\boldsymbol{\varepsilon}^p, \theta)}{\partial \boldsymbol{\varepsilon}^p} \ .$$

Application of the chain rule yields

$$\boldsymbol{\pi}^p := \frac{\partial \tilde{\Psi}^p(\Lambda^p, \theta)}{\partial \Lambda^p} \frac{\partial \hat{\Lambda}^p(\boldsymbol{\varepsilon}^p)}{\partial \boldsymbol{\varepsilon}^p} \ . \tag{A.1}$$

For each part of (A.1) the chain rule is further applied

$$\begin{aligned} \frac{\partial \tilde{\Psi}^p}{\partial \Lambda^p} &= \frac{\partial \tilde{\Psi}^p}{\partial \Lambda^p_r} \frac{\partial \Lambda^p_r}{\partial \Lambda^p} \\ \frac{\partial \hat{\Lambda}^p}{\partial \boldsymbol{\varepsilon}^p} &= \frac{\partial \hat{\Lambda}^p}{\partial \lambda^p_A} \frac{\partial \lambda^p_A}{\partial \boldsymbol{\varepsilon}^p} \end{aligned} \tag{A.2}$$

with the plastic network stretch defined by the *eight chain model*

$$\begin{aligned} \Lambda^{p2} &= \frac{1}{3}[\lambda_1^{p2} + \lambda_2^{p2} + \lambda_3^{p2}] = \sum_{A=1}^{3} \frac{1}{3} \lambda_A^{p2} \quad \text{and} \\ \Lambda^p &= \sqrt{\tfrac{1}{3} \textstyle\sum_{A=1}^{3} \lambda_A^{p2}} \end{aligned} \tag{A.3}$$

The derivatives of the chain rule in $(A.2)_1$ give

$$\begin{aligned} \frac{\partial \tilde{\Psi}^p}{\partial \Lambda^p_r} &= \hat{\mu}_p \hat{N}_p \ \mathcal{L}^{-1}(\Lambda^p) \\ \frac{\partial \Lambda^p_r}{\partial \Lambda^p} &= (\hat{N}_p)^{-1/2} \end{aligned} \tag{A.4}$$

yielding finally for $(A.2)_1$

$$\frac{\partial \tilde{\Psi}^p}{\partial \Lambda^p} = \hat{\mu}_p \Lambda^p \frac{3 - \Lambda_r^{p2}}{1 - \Lambda_r^{p2}} \ . \tag{A.5}$$

The latter was obtained by making use of the already introduced identities $\mathcal{L}^{-1}(\Lambda^p_r) \approx \Lambda^p_r \ (3N_p - \lambda^{p2})/(N_p - \lambda^{p2})$ and $\Lambda^p = \sqrt{N_p} \Lambda^p_r$. It can be observed that $\partial_{\Lambda^p} \tilde{\Psi}^p(\Lambda^p, \theta)$ can be additionally split into two parts due to the dependence of the inverse Langevin function $\mathcal{L}^{-1}$ on Λ^p

$$\frac{\partial \tilde{\Psi}^p}{\partial \Lambda^p} = \frac{\partial \tilde{\Psi}^p}{\partial \Lambda^p} + \frac{\partial \tilde{\Psi}^p}{\partial \mathcal{L}^{-1}} \frac{\mathcal{L}^{-1}}{\Lambda^p}. \tag{A.6}$$

Nevertheless, as it is shown in Appendix B, the derivative $\partial_{\mathcal{L}^{-1}} \tilde{\Psi}^p$ vanishes, making (A.5) to hold. For the second chain rule operation in (A.2) we have

$$\begin{aligned} \frac{\partial \hat{\Lambda}^p}{\partial \lambda^p_A} &= \frac{1}{\sqrt{3}} \frac{\sum_{A=1}^{3} \lambda^p_A}{\sum_{A=1}^{3} \lambda^p_A} = \sum_{A=1}^{3} \frac{\lambda^p_A}{3\Lambda^p} \quad \text{and} \\ \frac{\partial \lambda^p_A}{\partial \boldsymbol{\varepsilon}^p} &= \frac{\partial \exp[\epsilon^p_A]}{\partial \boldsymbol{\varepsilon}^p} = \exp[\epsilon^p_A] \, \boldsymbol{n}^p_A \otimes \boldsymbol{n}^p_A \end{aligned} \tag{A.7}$$

obtained by means of $\lambda_A^p := \exp[\epsilon_A^p]$ and $\partial_{\boldsymbol{\varepsilon}^p}\epsilon_A^p = \boldsymbol{n}_A^p \otimes \boldsymbol{n}_A^p$, yielding finally for $(A.2)_2$

$$\frac{\partial \hat{\Lambda}^p}{\partial \boldsymbol{\varepsilon}^p} = \sum_{A=1}^{3} \frac{\lambda_A^{p2}}{3\Lambda^p} \boldsymbol{n}_A^p \otimes \boldsymbol{n}_A^p \ . \tag{A.8}$$

Direct insertion of (A.5) and (A.8) into (A.1) yields

$$\boldsymbol{\pi}^p := \hat{\mu}_p \Lambda^p \frac{3 - \Lambda_r^{p2}}{1 - \Lambda_r^{p2}} \cdot \sum_{A=1}^{3} \frac{\lambda_A^{p2}}{3\Lambda^p} \boldsymbol{n}_A^p \otimes \boldsymbol{n}_A^p \tag{A.9}$$

Rearranging the terms we get

$$\boldsymbol{\pi}^p := \frac{\hat{\mu}_p}{3} \frac{3 - \Lambda_r^{p2}}{1 - \Lambda_r^{p2}} \cdot \sum_{A=1}^{3} \lambda_A^{p2} \boldsymbol{n}_A^p \otimes \boldsymbol{n}_A^p \tag{A.10}$$

finally giving the closed form of the back–stresses in terms of the plastic metric $(4.44)_1$

$$\boxed{\boldsymbol{\pi}^p := \frac{\hat{\mu}_p}{3} \frac{3 - \Lambda_r^{p2}}{1 - \Lambda_r^{p2}} \boldsymbol{G}^p \quad \text{with} \quad \boldsymbol{G}^p = \sum_{A=1}^{3} \lambda_A^{p2} \boldsymbol{n}_A^p \otimes \boldsymbol{n}_A^p}$$

B. Statistics of the Freely Jointed Chain

In Appendix A the partial derivative of the plastic free energy function $\tilde{\Psi}^p$ with respect to $\mathcal{L}^{-1}$ is set to zero

$$\frac{\partial \tilde{\Psi}^p}{\partial \mathcal{L}^{-1}} = \mu_p \, N_p \left(\Lambda^p + \frac{1}{\mathcal{L}^{-1}(\Lambda^p)} - \coth \mathcal{L}^{-1}(\Lambda^p) \right) = 0 \; . \tag{B.1}$$

To understand this result a short introduction to the field of statistics of freely jointed chains has to be done. To get a deeper view in this topic see for example Appendix C in Göktepe [38] and Flory [33],[34]and [35]. Almost all network models have to find a way to approximate the existing structure into an idealized chain of freely rotation links. This is done by the statistical treatment of a single polymer chain as depicted in Figure B.1.

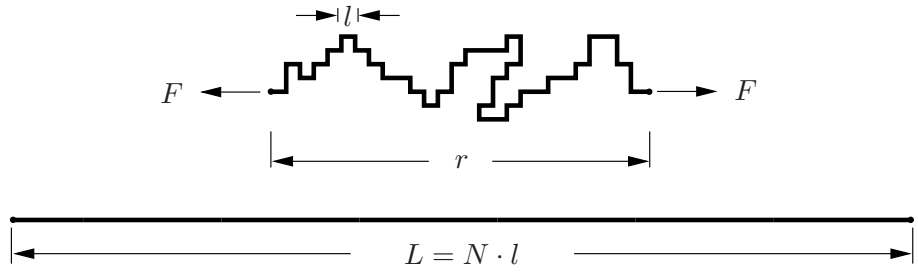

Figure B.1: Idealized linear polymer macromolecule approximated with N segments with the average segment length l. The momentary entangled length is denoted by r and the total straighten out length is $L = N \cdot l$.

The geometric structure is idealized by N segments of equal length l (denoted as the Kuhn segment length). Through determination of the energy and enthalpy state with the non–Gaussian–chain statistics the end–to–end length r of the entangled polymer chain is given by

$$r = N \, l \, \mathcal{L}(\chi) = L \, \mathcal{L}(\chi) \tag{B.2}$$

being $\mathcal{L}(\chi) := \coth(\chi) - 1/(\chi)$ the Langenvin function of $\chi = \frac{1}{k_B \theta} \, F \, l = \mathcal{L}^{-1}(\Lambda^p)$ with the Boltzmann constant k_B, the temperature θ and the force F. Reconsidering the defintion of the relative stretch gives

$$\Lambda^p := \frac{l_0}{l} = \frac{r}{L} = \mathcal{L}(\chi) \tag{B.3}$$

by inserting this in equation (B.1) the partial derivative of $\tilde{\Psi}^p$ with respect to $\mathcal{L}^{-1}$ yields

$$\begin{aligned} \frac{\partial \tilde{\Psi}^p}{\partial \mathcal{L}^{-1}} &= \mu_p \, N_p \left(\mathcal{L}(\chi) + \frac{1}{\mathcal{L}^{-1}(\Lambda^p)} - \coth \mathcal{L}^{-1}(\Lambda^p) \right) \\ &= \mu_p \, N_p \left(\coth \mathcal{L}^{-1}(\Lambda^p) - \frac{1}{\mathcal{L}^{-1}(\Lambda^p)} + \frac{1}{\mathcal{L}^{-1}(\Lambda^p)} - \coth \mathcal{L}^{-1}(\Lambda^p) \right) \\ &= 0 \; . \end{aligned} \tag{B.4}$$

References

[1] `http://www.makrolon.com`.

[2] `http://www.campusplastics.com`.

[3] `http://dki-online.de`.

[4] `http://www.gom.com`.

[5] `http://www.wd40.com/faqs`.

[6] Allison, S. W.; Ward, I. M. [1967]: *The Cold Drawing of Polyethylene Terephthalate*. Journal of Applied Physics, 18: 1151–1164.

[7] Anand, L.; Gurtin, M. E. [2003]: *A Theory of Amorphous Solids Undergoing Large Deformations, with Application to Polymeric Glasses*. International Journal of Solids and Structures, 40: 1465–1487.

[8] Argon, A. S. [1973]: *A Theory for the Low–Temperature Plastic Deformation of Glassy Polymers*. The Philosophical Magazine, 28: 839–865.

[9] Armero, F.; Simo, J. C. [1992]: *A New Unconditionallly Stable Fractional Method for Non-linear Coupled Thermomechanical Problems*. International Journal for Numerical Methods in Engineering, 35: 737–766.

[10] Arruda, E. M.; Boyce, M. C. [1993]: *A Three–Dimensional Constitutive Model for the Large Stretch Behavior of Rubber Elastic Materials*. Journal of the Mechanics and Physics of Solids, 41: 389–412.

[11] Arruda, E. M.; Boyce, M. C.; Jayachandran, R. [1995]: *Effects of Strain Rate, Temperature and Thermomechanical Coupling on the Finite Strain Deformation of Glassy Polymers*. Mechanics of Materials, 19: 193–212.

[12] Ashby, M. F.; Jones, D. R. H. [1986]: *Engineering Materials II*. Pergamon Press, Oxford, 1st Edition.

[13] Ashby, M. F.; Jones, D. R. H. [1998]: *Engineering Materials II*. Pergamon Press, Oxford, 2nd Edition.

[14] Basu, S.; van der Giessen, E. [2002]: *A Thermo–mechanical Study of Mode I, Small–Scale Yielding Crack–Tip Fields in Glassy Polymers*. International Journal of Plasticity, 18: 1395–1423.

[15] Bauwens-Crowet, C.; Bauwens, J. C.; Homes, G. [1969]: *Tensile Yield–Stress Behavior of Glassy Polymers*. Journal of Polymer Science: Part A-2, 7: 735–742.

[16] Bowden, P. B. [1973]: *Introduction*. In Haward, R. N. (Editor): *The Physics of Glassy Polymers*, Chapter 5, pp. 279–339. Applied Science Publishers Ltd, London, 1st Edition.

[17] Boyce, M. C.; Arruda, E. M. [1990]: *An Experimental and Analytical Investigation of the Large Strain Compressive and Tensile Response of Glassy Polymers*. Polymer Engineering and Science, 30: 1288–1298.

[18] Boyce, M. C.; Arruda, E. M.; Jayachandran, R. [1994]: *The Large Strain Compression, Tension, and Simple Shear of Polycarbonate*. Polymer Engineering and Science, 34: 716–725.

[19] Boyce, M. C.; Haward, R. N. [1997]: *The Post–Yield Deformation of Glassy Polymers*. In Haward, R. N.; Young, R. J. (Editors): *The Physics of Glassy Polymers*, Chapter 5, pp. 213–293. Chapman & Hall, London, 2nd Edition.

[20] Boyce, M. C.; Montagut, E. L.; Argon, A. S. [1992]: *The Effects of Thermomechanical Coupling on the Cold Drawing Process of Glassy Polymers*. Polymer Engineering and Science, 32: 1073–1085.

[21] Boyce, M. C.; Parks, D. M.; Argon, A. S. [1988]: *Large Inelastic Deformation of Glassy Polymers. Part I: Rate Dependent Constitutive Model*. Mechanics of Materials, 7: 15–33.

[22] Boyce, M. C.; Weber, G. G.; Parks, D. M. [1989]: *On the Kinematics of Finite Strain Plasticity*. Journal of the Mechanics and Physics of Solids, 37: 647–665.

[23] Brady, T. E.; Yeh, G. S. [1971]: *Yielding Behavior of Glassy Amorphous Polymers*. Journal of Applied Physics, 42: 4622–4630.

[24] Brown, N.; Ward, L. M. [1968]: *Load Drop at the Upper Yield Point of a Polymer*. Journal of Polymer Science Part A-2, 6: 607–620.

[25] Brydson, J. A. [1999]: *Plastics Materials*. Elsevier, 7th Edition.

[26] Bueche, F. [1962]: *Physical Properties of Polymers*. John Wiley & Sons, Inc., New York, London, 1st Edition.

[27] Carraher, C. E. [2000]: *Introduction to Polymer Science and Technology*. In Craver, C.D.; Carraher, C. (Editors): *Applied Polymer Science: 21st Century*, Chapter 1.2, page 21. Elsevier Science Ltd., UK, 1st Edition.

[28] Christiansen, A. W.; Baer, E.; Radcliffe, S. V. [1971]: *The Mechanical Behaviour of Polymers under High Pressure*. Philisophical Magazine, 24: 451–467.

[29] Cohen, A. [1991]: *A Padé Approximant to the Inverse Langevin Function*. Rheological Acta, 30: 270–273.

[30] Crist, B. [1997]: *Yield Processes in Glassy Polymers*. In Haward, R. N.; Young, R. J. (Editors): *The Physics of Glassy Polymers*, Chapter 4, pp. 155–212. Chapman & Hall, London, 2nd Edition.

[31] Dal, H. [2005]: *Approaches to the Modeling of Thermoviscoplastic Behavior of Glassy Polymers*. Master Thesis 05-I-06, Institut für Mechanik (Bauwesen), Lehrstuhl I, Universität Stuttgart.

[32] Dupaix, R. B.; Boyce, M. C. [2005]: *Finite Strain Behavior of Poly(ethylene terephthalate) (PET) and Poly(ethylene terephthalate)-glycol (PETG)*. Polymer, 46: 4827–4838.

[33] Flory, P. J. [1953]: *Principles of Polymer Chemistry*. Cornell University Press, Ithaca.

[34] Flory, P. J. [1976]: *Statistical Thermodynamics of Random Networks*. Proceedings of the Royal Society London A, 351: 351–380.

[35] Flory, P. J. [1989]: *Statistical Mechanics of Chain Molecules*. Clarendon Press, Oxford.

[36] Gilmour, I. W.; Trainor, R. A.; Haward, R. N. [1979]: *Elastic Moduli of Glassy Polymers at Low Strains*. Journal of Applied Polymer Science, 23: 3129–3138.

[37] Godovsky, Y. K. [1992]: *Thermophysical Properties of Polymers*. Springer–Verlag, Berlin, Heidelberg, New York.

[38] Göktepe, S. [2007]: *Micro-Macro Approaches to Rubbery and Glassy Polymers: Predictive Micromechanically-Based Models and Simulations*. Ph.D. Thesis, Universität Stuttgart.

[39] Golden, J. H.; Hammant, B. L.; Hazell, E. A. [1967]: *The Effect of Thermal Pretreatment on the Strength of Polycarbonate*. Journal of Applied Polymer Science, 11: 1571–1579.

[40] GOM mbH. [2001]: *ARAMIS Introduction—Operation Manual*. GOM mbH, Braunschweig, Germany.

[41] G'Sell, C.; Aly-Helal, N. A.; Jonas, J. J. [1983]: *Effect of Stress Triaxiality on Neck Propagation during the Tensile Stretching of Solid Polymers*. Journal of Materials Science, 18: 2493–2502.

[42] G'Sell, C.; Hiver, J. M.; Dahoun, A. [2002]: *Experimental Characterization of Deformation Damage in Solid Polymers under Tension, and its Interrelation with Necking*. International Journal of Solids and Structures, 39: 3857–3872.

[43] G'Sell, C.; Hiver, J. M.; Dahoun, A.; Souahi, A. [1992]: *Video–Controlled Tensile Testing of Polymers and Metals Beyond the Necking Point*. Journal of Materials Science, 27: 5031–5039.

[44] G'Sell, C.; Jonas, J. J. [1979]: *Determination of the Plastic Behaviour of Solid Polymers at Constant True Strain Rate*. Journal of Materials Science, 14: 583–591.

[45] G'Sell, C.; Jonas, J. J. [1981]: *Yield and Transient Effects during the Plastic Deformation of Solid Polymers*. Journal of Materials Science, 16: 1956–1974.

[46] Hasan, O. A. [1994]: *An Experimental and Analytical Investigation of the Thermomechanical Properties of Glassy Polymers*. Ph.D. Thesis, Massachusets Institute of Technology.

[47] Hasan, O. A.; Boyce, M. C. [1995]: *A Constitutive Model for the Nonlinear Viscoelastic Viscoplastic Behavior of Glassy Polymers*. Polymer Engineering and Science, 35: 331–344.

[48] Hasan, O. A.; Boyce, M. C.; Li, X. S.; Berko, S. [1993]: *An Investigation of the Yield and Postyield Behavior and Corresponding Structure of Poly(methyl methacrylate)*. Journal of Polymer Science, 31: 185–197.

[49] Haward, R. N. [1973]: *The Post-Yield Behaviour of Amorphous Plastics*. In Haward, R. N. (Editor): *The Physics of Glassy Polymers*, Chapter 6, page 348. Applied Science Publishers Ltd., England, 1st Edition.

[50] Haward, R. N. [1994]: *Heating Effects in the Deformation of Thermoplastics*. Thermochimica Acta, 247: 87–109.

[51] Hutchinson, J. W.; Neale, K. W. [1983]: *Neck Propagation*. Journal of the Mechanics and Physics of Solids, 31: 405–426.

[52] Iyer, H. [2006]: *Micromechanically Based Thermo-Viscoplasticity of Glassy Polymers: Experiments and Constitutive Modeling*. Master Thesis 06-I-04, Institut für Mechanik (Bauwesen), Lehrstuhl I, Universität Stuttgart.

[53] James, H. M.; Guth, E. [1943]: *Theory of Elastic Properties of Rubber.* The Journal of Chemical Physics, 11: 455–481.

[54] Kocks, U. F.; Argon, A. S.; Ashby, M. F. [1975]: *Thermodynamics and Kinetics of Slip.* Progress in Materials Science, 19: 110–170.

[55] Kröner, E. [1960]: *Allgemeine Kontinuumstheorie der Versetzungen und Eigenspannungen.* Archive for Rational Mechanics and Analysis, 4: 273–334.

[56] Lee, E. H. [1969]: *Elastic–Plastic Deformation at Finite Strain.* ASME Journal of Applied Mechanics, 36: 1–6.

[57] Li, J. C. M.; Gilman, J. J. [1970]: *Disclination Loops in Polymers.* Journal of Applied Physics, 41: 4248–4256.

[58] Lu, J.; Ravi-Chandar, K. [1999]: *Inelastic Deformation and Localization Phenomena in Polycarbonate Under Tension.* International Journal of Solids and Structures, 36: 391–425.

[59] Maher, J. W.; Haward, R. N.; Hay, J. N. [1980]: *Study of the Thermal Effects in the Necking of Polymers with the Use of an Infrared Camera.* Journal of Polymer Science, 18: 2169–2179.

[60] Mandel, J. [1972]: *Plasticitè Classique et Viscoplasticitè.* Springer–Verlag, Berlin.

[61] Marquez-Lucero, A.; G'Sell, C.; Neale, K. W. [1989]: *Experimental Investigation of Neck Propagation in Polymers.* Polymer, 30: 636–642.

[62] Melick, H. G. H.; Govaert, L. E.; Meijer, H. E. H. [2003]: *Localization Phenomena in Glassy Polymers: Influence of Thermal and Mechanical History.* Polymer, 44: 3579–3591.

[63] Melick, H. G. H.; Govaert, L. E.; Meijer, H. E. H. [2003]: *On the Origin of Strain Hardening in Glassy Polymers.* Polymer, 44: 2493–2502.

[64] Méndez, J. [2004]: *Finite Elastic and Inelastic Behavior of Rubbery Polymers: Experiments and Modeling.* Master Thesis 04-I-02, Institut für Mechanik (Bauwesen), Lehrstuhl I, Universität Stuttgart.

[65] Miehe, C. [1994]: *Aspects of the Formulation and Finite Element Implementation of Large Strain Isotropic Elasticity.* International Journal of Numerical Methods in Engineering, 37: 1981–2004.

[66] Miehe, C. [1995]: *Entropic Thermo–Elasticity at Finite Strains: Aspects of the Formulation and Numerical Implementation.* Computer Methods in Applied Mechanics and Engineering, 120: 243–269.

[67] Miehe, C. [1995]: *A Theory of Large-Strain Isotropic Thermoplasticity Based on Metric Transformation Tensors.* Archive of Applied Mechanics, 66: 45–64.

[68] Miehe, C. [1998]: *A Constitutive Frame of Elastoplasticity at Large Strains Based on the Notion of a Plastic Metric.* International Journal of Solids and Structures, 35: 3859–3897.

[69] Miehe, C. [1998]: *A Formulation of Finite Elastoplasticity Based on Dual Co- and Contra-Variant Eigenvector Triads Normalized with Respect to a Plastic Metric.* Computer Methods in Applied Mechanics and Engineering, 159: 223–260.

[70] Miehe, C.; Apel, N. [2004]: *Anisotropic Elastic-Plastic Analysis of Shells at Large Strains. A Comparison of Multiplicative and Additive Approaches to Enhanced Finite Element Design and Constitutive Modelling.* International Journal for Numerical Methods in Engineering, 61: 2067–2113.

[71] Miehe, C.; Apel, N.; Lambrecht, M. [2002]: *Anisotropic Additive Plasticity in the Logarithmic Strain Space: Modular Kinematic Formulation and Implementation Based on Incremental Minimization Principles for Standard Materials.* Computer Methods in Applied Mechanics and Engineering, 191: 5383–5425.

[72] Miehe, C.; Göktepe, S.; Lulei, F. [2004]: *A Micro–Macro Approach to Rubber–Like Materials. Part I: The Non–Affine Micro–Sphere Model of Rubber Elasticity.* Journal of the Mechanics and Physics of Solids, 52: 2617–2660.

[73] Miehe, C.; Göktepe, S.; Méndez, J. [2009]: *Finite Viscoplasticity of Amorphous Glassy Polymers in the Logarithmic Strain Space.* International Journal of Solids and Structures, 46: 181–202.

[74] Miehe, C.; Keck, J. [2000]: *Superimposed Finite Elastic–Viscoelastic–Plastoelastic Stress Response with Damage in Filled Rubbery Polymers. Experiments, Modelling and Algorithmic Implementation.* Journal of the Mechanics and Physics of Solids, 48: 323–365.

[75] Miehe, C.; Lambrecht, M. [2001]: *Algorithms for Computation of Stresses and Elastic Moduli in Terms of Seth–Hill's Family of Generalized Strain Tensors.* Communications in Numerical Methods in Engineering, 17: 337–353.

[76] Parsons, E. M.; Boyce, M. C.; Parks, D. M.; Weinberg, M. [2005]: *Three-Dimensional Large-Strain Tensile Deformation of Neat and Calcium Carbonate-filled High-density Polyethylene.* Polymer, 46: 2257–2265.

[77] Qu, S. [2007]: *Temperature-Dependent Finite Viscoplasticity of Glassy Polymers: Experiments and Simulations.* Master Thesis 07-I-05, Institut für Mechanik (Bauwesen), Lehrstuhl I, Universität Stuttgart.

[78] Raha, S.; Bowden, P. B. [1972]: *Birefringence of Plastically Deformed Poly(methyl methacrylate).* Polymer, 13: 174–183.

[79] Rehage, G.; Borchard, W. [1973]: *The Thermodynamics of the Glassy State.* In Haward, R. N. (Editor): *The Physics of Glassy Polymers*, Chapter 1, page 54. Applied Science Publishers Ltd., England, 1st Edition.

[80] Sahagun, Fray B. de [1831]: *Historia Universal de las Cosas de la Nueva España.* In King, Lord Kingsborough E. (Editor): *Antiquities of Mexico*, Vol. VII.

[81] Scheday, G. [2003]: *Theorie und Numerik der Parameteridentifikation von Materialmodellen der finiten Elastizität und Inelastizität auf der Grundlage optischer Feldmeßmethoden.* Dissertationsschrift 03-I-11, Institut für Mechanik (Bauwesen), Lehrstuhl I, Universität Stuttgart.

[82] Séguéla, R. [2007]: *On the Natural Draw Ratio of Semi-Crystalline Polymers: Review of the Mechanical, Physical and Molecular Aspects.* Macromolecular Materials and Engineering, 292: 235–244.

[83] Simó, J.C.; Miehe, C. [1992]: *Associative Coupled Thermoplasticity at Finite Strains: Formulation, Numerical Analysis and Implementation.* Computer Methods in Applied Mechanics and Engineering, 98: 41–104.

[84] Spitzig, W. A.; Richmond, O. [1979]: *Effect of Hydrostatic Pressure on the Deformation Behavior Polyethylene and Polycarbonate in Tension and in Compression.* Polymer Engineering and Science, 19: 1129–1139.

[85] The Research Association of British Rubber Manufacturers [1947]: *Rubber Among the Mexican Indians.* Journal of Rubber Research, 16: 171–180.

[86] Treloar, L. R. G. [1946]: *The Photoelastic Properties of Short–Chain Molecular Networks.* Transactions of the Faraday Society, 50: 881–896.

[87] Treloar, L. R. G. [1975]: *The Physics of Rubber Elasticity.* Clarendon Press, Oxford, 3rd Edition.

[88] Treloar, L. R. G.; Riding, G. [1979]: *A Non–Gaussian Theory of Rubber in Biaxial Strain. I. Mechanical Properties.* Proceedings of the Royal Society London A, 369: 261–280.

[89] Vincent, P. I. [1960]: *The Necking and Cold–Drawing of Rigid Plastics.* Polymer, 1: 7–19.

[90] Wang, M. C.; Guth, E. [1952]: *Statistical Theory of Networks of Non–Gaussian Flexible Chains.* The Journal of Chemical Physics, 20: 1144–1157.

[91] Ward, I. M. [1983]: *Mechanical Properties of Solid Polymers.* John Wiley & Sons, Ltd., England, 2nd Edition.

[92] Weigert, M. [2009]: *Thermo–Mechanical Behavior of Glassy Polymers: Parameter Identification and Model Validation.* Diplomarbeit 09-I-06, Institut für Mechanik (Bauwesen), Lehrstuhl I, Universität Stuttgart.

[93] Zhou, Z.; Chudnovsky, A. [1995]: *Cold-Drawing (Necking) Behavior of Polycarbonate as a Double Glass Transition.* Polymer Engineering and Science, 35: 304–309.

Curriculum Vitae

Personal Data

Name	Joel Méndez Diez
Date of Birth	July 16, 1975
Place of Birth	Tehuacán, Mexico
Parents	Joel Méndez Ballesteros and Maria Luisa Diez de Méndez
Siblings	Maria Luisa Méndez Diez
Marital Status	Married
Nationality	Mexican

School Education

1981-1987	Unidad Escolar Benavente Primary School, Tehuacán
1987-1990	Colegio Saleciano Benavente Secondary School, Tehuacán
1991-1994	Colegio Saleciano Benavente High School, Tehuacán

University Education

1994-2001	B.Sc. in Mechanical Engineering, Universidad de las Americas – Puebla, Puebla
2002-2004	M.Sc. in Computational Mechanics of Materials and Structures (COMMAS), University of Stuttgart

Professional Occupation

1999-2000	System Administrator, Company Tag-it Pacific, Tehuacan and Tijuana
2004-2009	Research Associate, Institute of Applied Mechanics, Civil Engineering, University of Stuttgart

In dieser Schriftenreihe bisher erschienene Berichte:

I-1(1996) *Theoretische und algorithmische Konzepte zur phänomenologischen Beschreibung anisotropen Materialverhaltens*, J. Schröder, Dissertation, 1996.

I-2(1996) *Zur Theorie und Numerik finiter elastoplastischer Deformationen von Schalentragwerken*, B. Seifert, Dissertation, 1996.

I-3(1996) *Zur Modellierung des künstlichen Infrarot-Dichroismus in Poymerfolien bei großen Verformungen*, J. Buhler, Dissertation, 1996.

I-4(1998) *Verfahren zur Ermittlung der Erdbebenlasten mit Berücksichtigung des stochastischen Charakters des Bebens*, S. Zhang, Dissertation, 1998.

I-5(1998) *Zur Beschreibung finiter Deformationen von Polymeren: Experimente, Modellbildung, Parameteridentikation und Finite-Elemente- Formulierung*, J. Keck, Dissertation, 1998.

I-6(1999) *Berechnungsverfahren instationär erregter Systeme im Frequenzbereich*, A. Jaworek, Dissertation, 1999.

I-7(2000) *Homogenisierungsmethoden der nichtlinearen Kontinuumsmechanik unter Beachtung von Stabilitätsproblemen*, J. Schröder, Habilitation, 2000.

I-8(2002) *Theorie und Numerik von Materialinstäbilitaten elastoplastischer Festkörper auf der Grundlage inkrementeller Variationsformulierungen*, M. Lambrecht, Dissertation, 2002.

I-9(2002) *Mikromechanisch motivierte Modelle zur Beschreibung finiter Deformationen gummiartiger Polymere: physikalische Modellbildung und numerische Simulation*, F. Lulei, Dissertation, 2002.

I-10(2003) *Adaptive Finite-Elemente-Berechnungen der nichtlinearen Festkörpermechanik bei kleinen und großen Verzerrungen*, A. Koch, Dissertation, 2003.

I-11(2003) *Theorie und Numerik der Parameteridentikation von Materialmodellen der finiten Elastizität und Inelastizität auf der Grundlage optischer Feldmeßmethoden*, G. Scheday, Dissertation, 2003.

I-12(2004) *Approaches to the Description of Anisotropic Material Behaviour at Finite Elastic and Plastic Deformations, Theory and Numerics*, N. Apel, Dissertation, 2004.

I-13(2004) *Temperaturabhängige Beschreibung visko-elasto-plastischer Deformationen kurzglasfaserverstärkter Thermoplaste: Modellbildung, Numerik und Experimente*, S. Rieger, Dissertation, 2004.

I-14(2005) *Zur Parameteridentikation komplexer Materialmodelle auf der Basis realer und virtueller Testdaten*, A. Rieger, Dissertation, 2005.

I-15(2005) *Viskoelastisches Verhalten von Elastomeren bei finiten Verzerrungen: Experimente, Modellierung und Simulationen*, H. Zecha, Dissertation, 2005.

I-16(2005) *Mehrskalenmodelle in der Festkörpermechanik und Kopplung von Mehrgittermethoden mit Homogenisierungsverfahren*, C.G. Bayreuther, Dissertation, 2005.

I-17(2005) *Static and Dynamic Homogenization Analyses of Discrete Granular and Atomistic Structures on Different Time and Length Scales*, J. Dettmar, Dissertation, 2005.

I-18(2006) *Incompatibility and Instability Based Size Effects in Crystals and Composites at Finite Elastoplastic Strains*, M. Becker, Dissertation, 2006.

I-19(2007) *Aspects of Energy Minimization in Solid Mechanics: Evolution of Inelastic Microstructures and Crack Propagation*, E. Gürses, Dissertation, 2007.

I-20(2007) *Micro-Macro Approaches to Rubbery and Glassy Polymers: Predictive Micromechanically-Based Models and Simulations*, S. Göktepe, Dissertation, 2007.

I-21(2008) *Material Forces in Finite Inelasticity and Structural Dynamics: Topology Optimization, Mesh Refinement and Fracture*, D. Zimmermann, Dissertation, 2008.

I-22(2010) *Thermoviscoplasticity of Glassy Polymers: Experimental Characterization, Parameter Identification and Model Validation*, J. Méndez Diez, Dissertation, 2010.